Universidade Federal do Rio Grande
Escola de Engenharia
Programa de Pós-Graduação em Engenharia Oceânica

---

# Constructal Design applied to an Oscillating Water Column Wave Energy Converter device subjected to a realistic sea state

Dissertação de:
**Rafael Pereira Maciel**

Orientador:
**Liércio André Isoldi**

Coorientador:
**Mateus das Neves Gomes**

September 2022

**Constructal Design applied to an Oscillating Water Column Wave Energy Converter device subjected to a realistic sea state**

**Rafael Pereira Maciel**
Mestre em Engenharia Oceânica

Dissertação submetida ao Programa de Pós-Graduação em Engenharia Oceânica (PPGEO) da Escola de Engenharia da Universidade Federal do Rio Grande (FURG), como parte dos requisitos para a obtenção do título de Mestre em Engenharia Oceânica.

Prof. Dr. Liércio André Isoldi
Coordenador do PPGEO

Banca examinadora:

Prof. Dr. Liércio André Isoldi
Orientador — PPGEO/FURG

Prof. Dr. Mateus das Neves Gomes
Coorientador — IFPR

Prof. Dr. Elizaldo Domingues dos Santos
Membro Interno — PPGEO/FURG

Prof.ª Dr.ª Bianca Neves Machado
Membro Externo — UFRGS

Rio Grande, September 15th, 2022

M152c Maciel, Rafael Pereira.
Constructal Design applied to an Oscillating Water Column Wave Energy Converter device subjected to a realistic sea state / Rafael Pereira Maciel – 2022.
94 f.

Dissertação (mestrado) – Universidade Federal do Rio Grande – FURG, Programa de Pós-Graduação em Engenharia Oceânica, Rio Grande/RS, 2022.
Orientador: Dr. Liércio André Isoldi.
Coorientador: Dr. Mateus das Neves Gomes.

1. Wave energy 2. Renewable Energy 3. WaveMIMO Methodology 4. Irregular Waves I. Isoldi, Liércio André II. Gomes, Mateus das Neves III. Título.

CDU 62:551.46

Catalogação na Fonte: Bibliotecário José Paulo dos Santos CRB 10/2344

*Look again at that dot. That's here. That's home. That's us. On it everyone you love, everyone you know, everyone you ever heard of, every human being who ever was, lived out their lives. The aggregate of our joy and suffering, thousands of confident religions, ideologies, and economic doctrines, every hunter and forager, every hero and coward, every creator and destroyer of civilization, every king and peasant, every young couple in love, every mother and father, hopeful child, inventor and explorer, every teacher of morals, every corrupt politician, every "superstar," every "supreme leader," every saint and sinner in the history of our species lived there – on a mote of dust suspended in a sunbeam.*

---

Carl Sagan

# Agradecimentos

Agradeço e dedico, primeiramente, este trabalho à minha mãe e ao meu pai, que sempre me apoiaram e estiveram do meu lado.

Ao professor Liércio, que, além de um excelente orientador, sempre foi muito humano comigo. Agradeço também aos professores Bianca e Mateus, ao Phelype, ao acadêmico Milad Zabihi e à Alexandra Elbakyan, a ajuda de vocês foi essencial no desenvolvimento deste trabalho.

Agradeço ao professor Luís Henrique, que sempre orientou que eu me dedicasse à pesquisa acadêmica.

Aos amigos do Ceará, Carol, Fred, Lima, Deyse, Malika, Ju, Mariana, Bruna, Pow, Mara e Nívea, bem como aos familiares Gabriel, Betinha, Rafael, Rafaela e Elinardo, os quais sempre tornaram e ainda tornam maravilhosa a vida nesse lugar incrível.

Aos amigos com quem dividi a experiência de morar em Rio Grande, Nágila, Lua, Raylton, Álvaro, Gabriela, Werner, Jeferson e Marta. Sempre lembrarei do nossa amizade na FURG.

Aos amigos do intercâmbio, Alex, Rodrigo, Beto e Danilo, mesmo depois de tantos anos vocês ainda são muito importantes na minha vida.

Ao apoio do Conselho Nacional de Desenvolvimento Científico e Tecnológico (CNPq) pela bolsa de mestrado (Chamada CNPq/EQUINOR Energia Ltda. 2018, processo 440020/2019-0) e da Universidade Federal do Rio Grande (FURG).

# Abstract

**Rafael Pereira Maciel**

Constructal Design applied to an Oscillating Water Column Wave Energy Converter device subjected to a realistic sea state

This work presents a numerical analysis of an Oscillating Water Column (OWC) converter device, an ocean Wave Energy Converter (WEC) into electrical energy, using realistic sea state data. The main goal of this work is to perform a geometric evaluation of this device in order to define an optimal geometry to maximize its available hydrodynamic power. To do so, the WaveMIMO methodology was employed, which converts sea data from spectral wave model Tomawac into time series of free surface elevation, which is, then, appropriately treated and transformed into orbital velocity components of water particles. Tomawac obtained realistic sea state data from the coastal region of the city of Rio Grande, in the state of Rio Grande do Sul, Brazil, for the year 2014, which was used for the study case. In the numerical simulations, it was also employed a methodology which uses transient velocity data as a means to impose velocity boundary condition for the generation of numerical waves. This methodology was validated reproducing a laboratory experiment with regular waves, which consisted of laboratory-scale OWC device inserted in a wave channel. To perform the geometrical evaluation of the device, the Constructal Design method is employed. The objective function is to maximize the available hydropneumatic power. The hydropneumatic chamber volume ($V_{HC}$) and the total volume of the OWC device ($V_T$) are adopted as geometric constraints of the problem and were kept constant. Three degrees of freedom (DOF) are chosen for this study: $H_1/L$ (ratio between height and length of the hydropneumatic chamber), whose values are varied, $H_2/l$ (ratio between height and length of the turbine duct) and $H_3$ (submergence depth of hydropneumatic chamber), whose values were kept constant. Finally, the best device performance happened with geometry of $H_1/L$ value of 0.1985 and presented a hydropneumatic power $P_{hyd}$ of 29.63 W. That is 4.34 times higher than the power obtained with the worst geometry performance, which was 6.83 W, obtained with the degree of freedom $H_1/L$ value of 2.2789; and 2.49 times higher than the power obtained by the device with the same dimensions as those from the one in Pico island, which was 11.89 W. The contribution of this study is to perform a geometric evaluation, with the Constructal Design method, of an OWC device subjected to realistic irregular waves from the wave climate of the coastal region of the city of Rio Grande, in the state of Rio Grande do Sul, Brazil, which is unprecedented in the literature.

**Keywords**: Wave energy. Renewable Energy. WaveMIMO Methodology. Irregular Waves.

# Resumo

**Rafael Pereira Maciel**

Design Construtal aplicado a um dispositivo conversor do tipo Coluna de Água Oscilante submetido a um estado de mar realístico

O presente trabalho apresenta uma análise numérica de um dispositivo conversor de energia de ondas do mar em energia elétrica do tipo Coluna de Água Oscilante (do inglês, OWC), empregando dados realísticos de estado do mar. O objetivo deste trabalho é realizar uma avaliação geométrica deste dispositivo, a fim de se definir uma geometria ótima para maximizar a potência hidrodinâmica disponível. Para tanto, foi empregada a metodologia WaveMIMO, que converte dados de mar do modelo de ondas espectral Tomawac em séries temporais de elevação da superfície livre, que são, por sua vez, devidamente tratadas e transformadas em componentes de velocidade orbital de partículas de água. Por meio do Tomawac foram obtidos dados realísticos de estado de mar da região costeira da cidade de Rio Grande, Rio Grande do Sul, para o ano de 2014, os quais foram usados para o estudo de caso. Assim, nas simulações numéricas, foi empregada uma metodologia que utiliza dados de velocidade transiente como condições de contorno de velocidade para a geração de ondas numéricas. Esta metodologia foi validada reproduzindo um experimento de laboratório com ondas regulares, que consistia em um dispositivo OWC em escala laboratorial inserido em um canal de ondas. Para realizar a avaliação geométrica do dispositivo, é empregado o método Design Construtal. A função objetivo é maximizar a potência hidropneumática disponível. O volume da câmara hidropneumática ($V_{HC}$) e o volume total do dispositivo OWC ($V_T$) são adotados como restrições geométricas do problema e foram mantidos constantes. Três graus de liberdade (do inglês, DOF) são escolhidos para este estudo: $H_1/L$ (relação entre altura e comprimento da câmara hidropneumática), cujos valores são variados, $H_2/l$ (relação entre altura e comprimento do duto da turbina ) e $H_3$ (profundidade de submersão da câmara hidropneumática), cujos valores foram mantidos constantes. O melhor desempenho do dispositivo aconteceu com a geometria de valor $H_1/L$ igual a 0,1985 e apresentou uma potência hidropneumática $P_{hyd}$ de 29,63 W. Isso é 4,34 vezes maior que a potência obtida com o pior desempenho geométrico, que foi de 6,83 W, obtido com o grau de liberdade $H_1/L$ igual a 2,2789 e 2,49 vezes superior à potência obtida pelo dispositivo com as mesmas dimensões do dispositivo da ilha do Pico, que foi de 11,89 W. A contribuição deste estudo é realizar uma avaliação geométrica, com o método Design Construtal, de um dispositivo OWC submetido a ondas realísticas região costeira da cidade de Rio Grande, Rio Grande do Sul, o que é algo inédito na literatura.

**Palavras-chave**: Energia das Ondas do Mar. Energias Renováveis. Metodologia WaveMIMO. Ondas Irregulares.

# Contents


| | | Page |
|---|---|---|
| | • **List of Figures** | **X** |
| | • **List of Tables** | **XIII** |
| | • **List of Symbols** | **XIV** |
| | • **List of Acronyms** | **XVII** |
| **1** | • **Introduction** | **1** |
| 1.1 | • Objectives | 2 |
| 1.1.1 | • Specific Objectives | 3 |
| 1.2 | • Text structure | 3 |
| **2** | • **Theoretical Foundation** | **4** |
| 2.1 | • Wave Theory | 4 |
| 2.1.1 | • Airy wave theory | 6 |
| 2.1.2 | • Stokes Wave Theory | 11 |
| 2.2 | • Wave Energy | 13 |
| 2.3 | • Oscillating Water Column Wave Energy Converter | 14 |
| 2.4 | • Finite Volume Method | 27 |
| 2.5 | • Constructal Design | 31 |
| 2.5.1 | • Constructal Design Method Applied to OWC Devices | 32 |
| **3** | • **Materials and Methods** | **35** |
| 3.1 | • WaveMIMO Methodology | 35 |
| 3.1.1 | • Spectral Data Conversion and Temporal Location of the Study Area | 37 |
| 3.2 | • Multiphase Hydrodynamic Model | 40 |
| 3.2.1 | • Statistical Measures | 42 |
| 3.3 | • Verification and Validation of the Hydrodynamic Model | 43 |
| 3.4 | • Numerical Simulation with Realistic Sea Data | 49 |
| 3.4.1 | • Simulation Discretization and Parameters | 50 |
| 3.4.2 | • Inserting the OWC device in the wave channel | 52 |
| 3.5 | • Application of Constructal Design Method | 55 |
| **4** | • **Results** | **59** |
| 4.1 | • Verification and Validation | 59 |
| 4.2 | • OWC subjected to realistic sea state | 67 |
| 4.3 | • Application of the Constructal Design Method | 71 |

**5 • Conclusions** **80**
5.1 • Suggestion for future studies . . . . . 82

• **References** **83**

# List of Figures


**Page**

**1 • Introduction**

1.1 • Annual mean wave power along the Brazilian coast (Espindola and Araújo, 2017). . . . . 2

**2 • Theoretical Foundation**

2.1 • Classification of ocean waves according to their respective periods and frequencies (Holthuijsen, 2010). . . . . 5
2.2 • Wave characteristics (Dean and Dalrymple, 1991). . . . . 6
2.3 • Wave channel where two-dimensional waves are represented as a boundary value problem (Dean and Dalrymple, 1991). . . . . 7
2.4 • Wave profile shape of different progressive gravity waves (U.S. Army Corps of Engineers, 2002). . . . . 12
2.5 • Wave theory applicability chart. Adapted from U.S. Army Corps of Engineers (2002). . . . . 12
2.6 • Wave energy converter devices mentioned in table 2.1 (Falcão, 2014). 15
2.7 • Illustration of the operational principle of an Oscillating Water Column device (Maciel *et al.*, 2021). . . . . 15
2.8 • Kaimei barge (Falcão and Henriques, 2016). . . . . 16
2.9 • OWC device in Toftestallen, near Bergen, Norway (Falcão and Henriques, 2016). . . . . 16
2.10 • Devices installed in India and Japan, in 1990 (Falcão and Henriques, 2016). . . . . 17
2.11 • Prototype of an OWC device, on the Isle of Islay, Scotland (Falcão and Henriques, 2016). . . . . 17
2.12 • OWC Device on Dawashan Island in Zhuhai, Guangdong Province, China (Zhang, Li, and Lin, 2009). . . . . 18
2.13 • OWC device on Pico island, Azores, Portugal before and after the partial collapse that took place on April 17, 2018. . . . . 19
2.14 • LIMPET OWC device from the Isle of Islay, Scotland, United Kingdom (Heath, Whittaker, and Boake, 2000). . . . . 19
2.15 • Multi-chamber OWC power plant integrated into a breakwater in the port of Mutriku, Spain (Torre-Enciso *et al.*, 2009). . . . . 19
2.16 • Oceanlix Mk1 OWC device, in Wollongong, Australia (Falcão and Henriques, 2016). . . . . 20
2.17 • BBDB device in Galway Bay, Ireland (Falcão, 2014). . . . . 20
2.18 • Mk3 floating platform with multiple OWC chambers at Port Kembla, in Wollongong, Australia (Falcão, 2014). . . . . 21

2.19 • REWEC3 U-OWC device being built, in Civitavecchia port, Rome, Italy (Falcão and Henriques, 2016). . . . . 21
2.20 • GreenWAVE device, at Port Adelaide, Australia (Falcão and Henriques, 2016). . . . . 22
2.21 • OWC device in Yongsoo, Jeju island, South Korea (Falcão and Henriques, 2016). . . . . 22
2.22 • Discretization of an element or volume through numerical method (Maliska, 2004). . . . . 28
2.23 • Generic control volume. Adapted from (Maliska, 2004). . . . . 29

**3 • Materials and Methods**
3.1 • Summary flowchart of the WaveMIMO methodology. Shapes in lilac represent a step of the methodology and in yellow represent the action performed. . . . . 36
3.2 • Location of the point in the Cassino beach chosen for analysis, which will provide realistic sea state data for the simulations. . . . . 37
3.3 • Time series of significant wave height ($H_s$) and mean wave period ($T_m$) at the coast of Rio Grande, for the year 2014. . . . . 38
3.4 • Bivariate histogram of the time series of significant wave height and mean wave period for the year 2014 (Oleinik, 2020). . . . . 39
3.5 • Variance spectrum of the sea state on August 23$^{rd}$, 2014, at 00:00 (Tavares *et al.*, 2020). . . . . 39
3.6 • Computational domain used in this study for the hydrodynamic model verification. . . . . 44
3.7 • Sketch of boundary condition fractioning region used in the wave generation with the adopted methodology. . . . . 45
3.8 • Number of line segments at the region of wave generation and values of coefficient $C_1$ used in the verification study. . . . . 46
3.9 • Two-dimensional mesh used for wave generation verification. . . 46
3.10 • Dimensions of the physical model used in the experiments of Zabihi, Mazaheri, and Namin (2019) and of its cross-section (in m). . . . 47
3.11 • Computational domain used for validation of hydrodynamic model. 48
3.12 • Discretization of the computational domain employed in the methodology validation. . . . . 48
3.13 • Location of wave gauges and pressure sensors based on the experiments of Zabihi, Mazaheri, and Namin (2019) (in m). . . . . 49
3.14 • Computational domain used in this study for the numerical simulations with realistic sea data. . . . . 50
3.15 • Location alongside each line segment from where horizontal and vertical components of orbital wave velocity are calculated. . . . . 51
3.16 • Representation of the cross-section of the OWC device located in Pico island. Adapted from Joule III (1998). . . . . 52
3.17 • Dimensions of the OWC device used in this study. . . . . 53
3.18 • Computational domain with the OWC device inserted. . . . . 53
3.19 • Numerical probes in the computational domain. . . . . 54

3.20 • Summary flowchart of the Constructal Design method. . . . . 56
3.21 • Representation of the computational domain and the physical dimensions used in the geometrical analysis. . . . . 56

**4 • Results**
4.1 • Comparison of the discretization at the wave generation region for the validation procedure. . . . . 59
4.2 • Comparison of free surface elevation at the end of the channel, according to the values adopted for numerical beach coefficient $C_1$. . . . . 60
4.3 • Comparison of mesh discretizations tested for the validation procedure. 62
4.4 • Comparison of time step values tested in this study. . . . . 63
4.5 • Free surface elevation of wave gauges located outside the hydropneumatic chamber. . . . . 64
4.6 • Free surface elevation of wave gauges located inside the hydropneumatic chamber. . . . . 65
4.7 • Instantaneous free surface flow along a wave period, from 35.75 s to 37.95 s (Maciel *et al.*, 2021). . . . . 66
4.8 • Air pressure inside the hydropneumatic chamber, experimental versus numerical results. . . . . 67
4.9 • Free surface elevation at $x = 0$ m for different velocity inlet discretizations at the wave generation region. . . . . 68
4.10 • Free surface elevation at $x = 0$ m for different velocity inlet discretizations at the wave generation region. . . . . 68
4.11 • Free surface elevation at $x = 0$ m for different locations from where, alongside each line segment, wave velocity data is calculated. . . . 70
4.12 • Free surface elevation at $x = 0$ m for different locations from where, alongside each line segment, wave velocity data is calculated. . . . 70
4.13 • Free surface elevation at $x = 0$ m for different values of $H_1/L$. . . . 72
4.14 • Free surface elevation at $x = 0$ m for different values of $H_1/L$ (detail). 72
4.15 • Free surface elevation at $x = 0$ m and $x = 67.57$ m (center of the OWC device) for $H_1/L = 1.1167$. . . . . 74
4.16 • Spectra of free surface elevation at $x = 0$ m, $x = 50$ m, and $x = 67.57$ m (center of the OWC device) for $H_1/L = 1.1167$. . . . . 74
4.17 • Static pressure at the turbine duct for different values of $H_1/L$. . . . 75
4.18 • Static pressure at the turbine duct for different values of $H_1/L$ (detail). 75
4.19 • Mass flow rate at the turbine duct for different values of $H_1/L$. . . . 76
4.20 • Mass flow rate at the turbine duct for different values of $H_1/L$ (detail). 76
4.21 • Instantaneous hydropneumatic power of the OWC device for different values of $H_1/L$. . . . . 77
4.22 • RMS averaged hydropneumatic power of the OWC device for different values of $H_1/L$. . . . . 77
4.23 • Instantaneous wave flow during 5 s of simulation, from 295 s to 300 s, for geometry with $H_1/L = 1.1167$. . . . . 79
4.24 • Instantaneous wave velocity field during 5 s of simulation, from 295 s to 300 s, for geometry with $H_1/L = 1.1167$. . . . . 79

# List of Tables


**Page**

**2 • Theoretical Foundation**

2.1 • Classification of wave energy conversion technologies (Falcão, 2008). . 14

2.2 • Summary of the presented OWC devices. . . . . 23

**3 • Materials and Methods**

3.1 • Mesh element sizes used in the mesh independence study. . . . . 46

3.2 • Configurations of geometry adopted for the simulations in this study. 58

**4 • Results**

4.1 • NRMSE values for velocity inlet discretization at the wave generation region. . . . . 60

4.2 • Wave height ratio for each value of linear damping coefficient analyzed. 61

4.3 • NRMSE values for mesh discretization in the validation procedure. . 61

4.4 • NRMSE value for each time step analyzed. . . . . 62

4.5 • NRMSE value for numerical wave gauges and pressure sensor in the validation simulation. . . . . 66

4.6 • RMSE values for velocity inlet discretization at the wave generation region. . . . . 69

4.7 • RMSE values for velocity inlet discretization at the wave generation region. 71

4.8 • RMSE values for different values of degree of freedom $H_1/L$. . . . . 73

4.9 • Available hydropneumatic power according to each OWC device geometry simulated. . . . . 78

# List of Symbols

### *Roman Symbols*

| | |
|---|---|
| $A_i$ | Area of mesh volume [−]. |
| $a$ | Amplitude [m]. |
| $a$ | Hydropneumatic chamber dimension [m]. |
| $A_{duct}$ | Two-dimensional area of turbine duct of OWC device [$m^2$]. |
| $b$ | Hydropneumatic chamber dimension [m]. |
| $C_1$ | Linear damping coefficient [1/s]. |
| $C_2$ | Quadratic damping coefficient [1/m]. |
| $CO_2$ | Carbon Dioxide [kg]. |
| $D$ | Turbine duct diameter [m]. |
| $D_p$ | Main direction at peak period [rad]. |
| e | East face of generic control volume. |
| $F(x, y, z, t)$ | Function that represents a surface in space and time [−]. |
| $g$ | Gravitational acceleration [$m/s^2$]. |
| $H$ | Wave height [m]. |
| $h$ | Water depth [m]. |
| $H_1/L$ | Ratio between height and length of the hydropneumatic chamber [−]. |
| $H_2/l$ | Ratio between height and length of the turbine duct [−]. |
| $H_3$ | Submergence depth of the hydropneumatic chamber [−]. |
| $H_s$ | Significant wave height [m]. |
| $k$ | Wave number [1/m]. |
| $k_x$ | Wavenumber vector component in $x$ direction [1/m]. |
| $k_y$ | Wavenumber vector component in $y$ direction [1/m]. |
| $L$ | Wavelength [m]. |
| $L_1$ | Transversal dimension of wave channel [m]. |
| $\dot{m}$ | Mass flow rate [kg/s]. |
| $n$ | Number of observation values available for analysis, for RMSE calculation. |
| $N(f, \theta)$ | Wave action density directional spectrum [$m^2$ s/rad]. |
| n | North face of generic control volume. |
| $O_i$ | Observation results (or analytical, experimental), for RMSE calculation. |
| $O_{max}$ | Maximum observation value, for NRMSE calculation. |
| $O_{min}$ | Minimum observation value, for NRMSE calculation. |

| | |
|---|---|
| $p_\eta$ | Dynamic surface pressure [Pa]. |
| $p_{air}$ | Air static pressure at turbine duct of OWC device [Pa]. |
| $P_{hyd}$ | Hydropneumatic available power of OWC device [W]. |
| $h$ | Totality of source and sink terms [−]. |
| $r_{OWC_{Study}}$ | Ratio of turbine duct area and chamber area of the OWC device in this study [−]. |
| $r_{Pico}$ | Ratio of turbine duct area and chamber area of the OWC device in Pico island [−]. |
| $S$ | Source term in momentum equation [−]. |
| $S_i$ | Values obtained from simulation, for RMSE calculation. |
| s | South face of generic control volume. |
| $t$ | Time [s]. |
| $T_m$ | Mean wave period [s]. |
| $T_p$ | Peak wave period [s]. |
| $T_s$ | Significant wave period [s]. |
| $u$ | Component in the $x$ direction of a velocity vector [m/s]. |
| $u(z_i, t)$ | Wave component in horizontal direction, variable in time and along depth [m/s]. |
| $\vec{v}$ | Velocity vector ($\vec{v} = (u,\ v\, w)$) [m/s]. |
| $v$ | Component in the $y$ direction of a velocity vector [m/s]. |
| $v_{air}$ | Outflow air velocity at turbine duct of OWC device [m/s]. |
| $\vec{v} = (u,\ w)$ | Wave orbital velocity vector [m/s]. |
| $V_{HC}$ | Hydropneumatic chamber volume [$m^3$]. |
| $V_T$ | OWC device total volume [$m^3$]. |
| $w$ | Component in the $z$ direction of a velocity vector [m/s]. |
| w | West face of generic control volume. |
| $w(z_i, t)$ | Wave component in vertical direction, variable in time and along depth [m/s]. |
| $x$ | Longitudinal component of a Cartesian coordinate system [m]. |
| $x_e$ | End point of numerical beach in horizontal direction [m]. |
| $x_i(t)$ | Flow characteristic varying with time. |
| $X_{RMS}$ | Root mean square of flow characteristic $X$. |
| $x_s$ | Start point of numerical beach in horizontal direction [m]. |
| $y$ | Transversal component of a Cartesian coordinate system [m]. |
| $z$ | Vertical component of a Cartesian coordinate system [m]. |
| $z_b$ | Bottom coordinate along vertical direction [m]. |
| $z_{fs}$ | Free surface coordinate along vertical direction [m]. |
| $z_i$) | Variable depth of vertical profile [m]. |

### *Greek Symbols*

| | |
|---|---|
| $\alpha$ | Volume fraction of fluid [−]. |
| $\Delta t$ | Time step [s]. |
| $\Delta X$ | Horizontal dimension of generic control volume. |
| $\Delta Y$ | Vertical dimension of generic control volume. |
| $\epsilon$ | Perturbation expansion parameter [−]. |
| $\eta$ | Free surface elevation [m]. |
| $\mu$ | Absolute viscosity coefficient [kg/m s]. |
| $\mu_{air}$ | Air absolute viscosity coefficient [kg/m s]. |
| $\mu_{water}$ | Water absolute viscosity coefficient [kg/m s]. |
| $\phi$ | Velocity potential [−]. |
| $\phi_i$ | Variable field [−]. |
| $\pi$ | $\approx$ 3.141 592 653 589 793 238 462 643 383 279 502 884 197 169 399 375 105 820 974 944 592 |
| $\rho$ | Density [kg/m$^3$]. |
| $\rho_{air}$ | Air density [kg/m$^3$]. |
| $\rho_{water}$ | Water density [kg/m$^3$]. |
| $\sigma$ | Wave angular frequency [rad/s]. |

### *Other Symbols*

| | |
|---|---|
| $\nabla F$ | Gradient of function that represents a surface. |
| $\nabla p$ | Divergence of the vector field $p$. |
| $\nabla \cdot \rho\vec{v}$ | Divergence of the vector field $\rho\vec{v}$ [−]. |

# List of Acronyms

| | |
|---|---|
| TOMAWAC | TELEMAC-based Operational Model Addressing Wave Action Computation. |
| BBDB | Backward Bent Duct Buoy. |
| CFD | Computational fluid dynamics. |
| CNPq | *Conselho Nacional de Desenvolvimento Científico e Tecnológico*. |
| FURG | *Universidade Federal do Rio Grande*. |
| FVM | Finite volume method. |
| GEBCO | General Bathymetric Chart of the Oceans. |
| JONSWAP | Joint North Sea Wave Observation Project. |
| LIMPET | Land Installed Marine Pneumatic Energy Transformer. |
| NOAA | National Oceanic and Atmospheric Administration. |
| NP | Numerical probe. |
| NRMSE | Normalized root mean square error. |
| NWC | Numerical wave channel. |
| OSPREY | Ocean Swell Powered Renewable EnergY. |
| OWC | Oscillating Water Column. |
| PISO | Pressure-implicit with splitting of operators. |
| PS | Pressure sensor. |
| REWEC3 | Resonan Wave Energy Converter 3. |
| RMSE | Root mean square error. |
| RMS | Root mean square. |
| SST | Shear stress transport. |
| SWL | Surface water line. |
| VOF | Volume of fluid. |
| WEC | Wave Energy Converter. |
| WG | Wave gauge. |

# I Introduction

As world population grows, so does its demand for electricity. According to the United Nations World Water Development Report (World Water Assessment Programme, 2009), worldwide energy consumption is already six times higher than it was in 1950 and is projected to grow by around 55% by 2030. This demand implies a greater exploitation of natural resources to meet global supply needs. It is a well known fact that the heavily usage of the non-renewable fossil fuels (like coal, oil, natural gas) is the predominant contributor for global warming and climate change by releasing carbon dioxide (Vural, 2020).

In this scenario, renewable energies stand out, since they come from regenerative resources, do not deplete over time, and have a low environmental impact, in addition to reducing carbon emissions (Hil Baky, Rahman, and Islam, 2017). Renewable energy is considered the most effective way to minimize $CO_2$ emissions, therefore, renewable energy sources need to be developed as means to replace carbon-intensive energy sources (Zeng *et al.*, 2017).

In 2014 in Germany, about 27.3% of the electricity generated was derived from renewable sources, resulting in significant reductions in pollutant gas emissions since 1990, and in the growth of 1.4% in the country's economy. This is one of the many reasons which validated the importance of research and investment in technological developments seeking to build strategies that benefit the population and reduce the damage caused to the environment (Zeng *et al.*, 2017).

Although approximately 80% of global primary energy comes from fossil fuels, Brazil stands out in terms of usage of renewable sources, where these represent 80.4% of domestic electricity supply (International Energy Agency, 2017 and Empresa de Pesquisa Energética, 2018).

Given the Brazilian biodiversity that offers broad scenarios for the production and harvest of clean energy, this potential needs to be explored satisfactorily. In this perspective, the harvest of energy contained in ocean waves, in parallel with increasing technological development, become an alternative in search of a source of renewable energy of high performance, since oceans cover more than 70% of the Earth's surface (Ressurreição *et al.*, 2011).

Although progress in the commercialization of ocean energy is still relatively slow, the energy potential of the oceans is promising; part of this is due to the fact that the technology needed to harvest and produce this type of energy is still under development (Melikoglu, 2018). Around 1980, studies and models began to map the energy potential of the oceans around the planet. In a relatively recent study, Espindola and Araújo (2017) mapped the capacity, in kW/m, along the Brazilian coast, as shown in figure 1.1, where it was concluded that the mean wave power varies around 8 to 21

kW/m. Overall, tidal energy has high energy density, low environmental impact and high predictability (El Tawil, Charpentier, and Benbouzid, 2017).

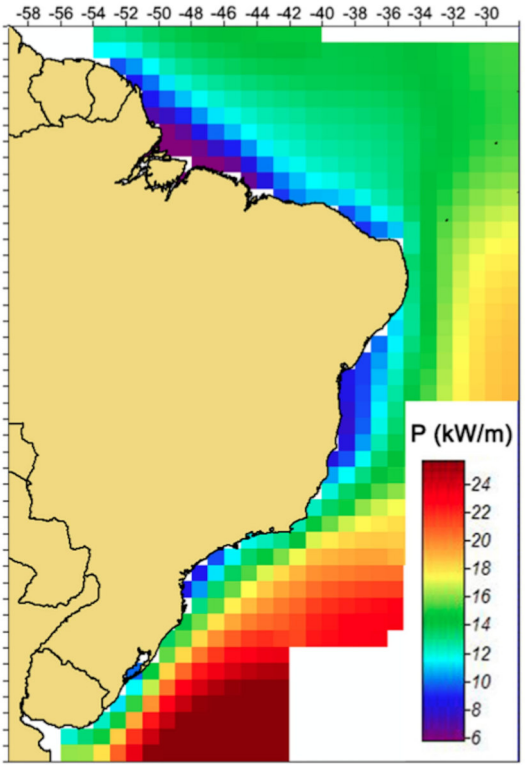


**Figure 1.1:** Annual mean wave power along the Brazilian coast (Espindola and Araújo, 2017).

In this context, the present study is justified by the need to produce clean energy, with low environmental cost and a good economic return for society. Several devices that convert ocean energy into electrical energy have been developed and improved, but because of its simple working principle, the Oscillating Water Column (OWC) type converter has gained prominence. Thus, it is proposed to investigate the performance of an OWC type converter. For this, realistic sea state data will be used, obtained through the Tomawac model, and inserted into the Fluent software, by means of the WaveMIMO methodology (Machado *et al.*, 2021), to numerically analyze fluid-dynamic behavior of the converter device.

## 1.1 Objectives

The main objective of this study is to numerically analyze an Oscillating Water Column (OWC) device submitted to a realistic sea state, performing a geometric evaluation of this device through the Constructal Design method, and analyzing the hydropneumatic power of this device when subjected to the wave climate of the coastal region of the city of Rio Grande, in the state of Rio Grande do Sul, Brazil.

### 1.1.1 Specific Objectives

The following specific objectives were defined in order to achieve the general objective:

I to apply the WaveMIMO methodology to obtain wave velocity data from the coastal region of the city of Rio Grande, in the state of Rio Grande do Sul, Brazil;

II to define a hydrodynamic numerical model of an OWC device, to verify wave generation in the computational domain, and to validate the adopted numerical model;

III to simulate the hydrodynamic behavior of an OWC device when subjected to the action of realistic waves;

IV to apply the Construtal Design method, to perform a geometric analysis on the OWC device, and to investigate the effect of varying degrees of freedom over the hydropneumatic available power of the device.

## 1.2 Text structure

This work was divided into 5 chapters. In chapter 2, the basic concepts and technologies used in this study are discussed. In chapter 3, the tools used are described, their applications in the accomplishment of this study, and the numerical simulations performed are explained, as well as their respective mesh independence study. In chapter 4, the results obtained at each step of this study are presented. Lastly, in chapter 5, the main conclusions drawn from the observed results are presented, as well as closing arguments.

# 2 Theoretical Foundation

As a way of ensuring that the reader can understand the terminology used in this study, as well as the main ideas and technologies involved, this chapter addresses, in a basic manner, the concepts of ocean wave theory, wave energy, wave energy conversion devices, the finite volume method, and Constructal Theory design. In addition, an extensive literature review of the most recent studies involving the Oscillating Water Column device, which converts wave energy into electrical energy, was carried out.

## 2.1 Wave Theory

Before any study on ocean waves energy, it is necessary to comprehend what characterizes a wave. Waves can be described as a disturbance or vibrational motion that travels through space and time, accompanied by a transportation of energy (Lerner and Trigg, 2005 and Ohanian and Markert, 2007). Halliday, Resnick, and Walker (2018) classify waves into three types: mechanical waves, electromagnetic waves, and material waves.

Mechanical waves have two main characteristics, they are governed by Newton's laws and can only exist in a material medium, such as water (water waves), air (sound waves), and rock (seismic waves). Electromagnetic waves do not need a material medium to exist and can therefore travel throughout vacuum; common examples are light waves, radio, television, radar, microwaves, among others. Material waves, in turn, are associated with electrons, protons, and other fundamental particles, such as atoms or molecules (Halliday, Resnick, and Walker, 2018).

Dean and Dalrymple (1991) classify waves found in bodies of water open to the atmosphere as a manifestation of forces acting on a fluid, tending to deform it against the actions of gravity and surface tension, which act together to maintain a free surface level. Among the forces that generate waves are wind, the impact of solid bodies on water, and the gravitational attraction of the moon, sun and other astronomical bodies (Dean and Dalrymple, 1991). Different origins and nature of surface oscillations affect wave characteristics, in terms of wave height and period (as well as wavelength), resulting in a wide variety of waves (Toffoli and Bitner-Gregersen, 2017). Holthuijsen (2010) classifies this variety of waves according to their period and frequency, which can be seen in figure 2.1.

Ocean waves have a random behavior; therefore, in order to be studied, they need the application of statistical analysis techniques. These waves can occur in the wave generation zones, where they are caused by the wind and have a more irregular character. They can also occur away from these generation zones, where they are called swell, have more elongated crests and more regular characteristics (Holthuijsen,

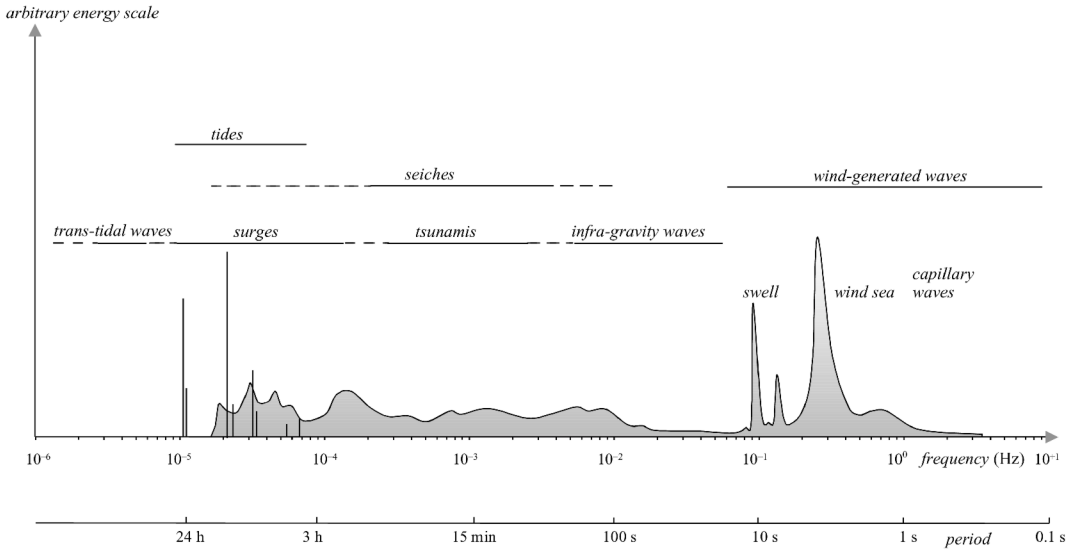


**Figure 2.1:** Classification of ocean waves according to their respective periods and frequencies (Holthuijsen, 2010).

2010).

To facilitate the understanding of the mathematical description of ocean waves, it is necessary to know the characteristics associated with these waves. The representation of such features can be seen in figure 2.2, where, according to Dean and Dalrymple (1991):

- **crest:** represents the point of highest elevation reached by water free surface;
- **trough:** represents the point of lowest elevation reached by water free surface;
- **wavelength ($L$):** represents the distance between two consecutive crests (or troughs);
- **wave height ($H$):** represents the difference in elevation between an adjacent crest and trough;
- **amplitude ($a$):** represents the difference in elevation between mean water level and a crest (or trough);
- **depth ($h$):** represents the vertical distance between mean water level and bottom surface;
- **free surface elevation ($\eta(x, t)$):** represents the instantaneous distance, in a given space and time, between water surface and mean water level.

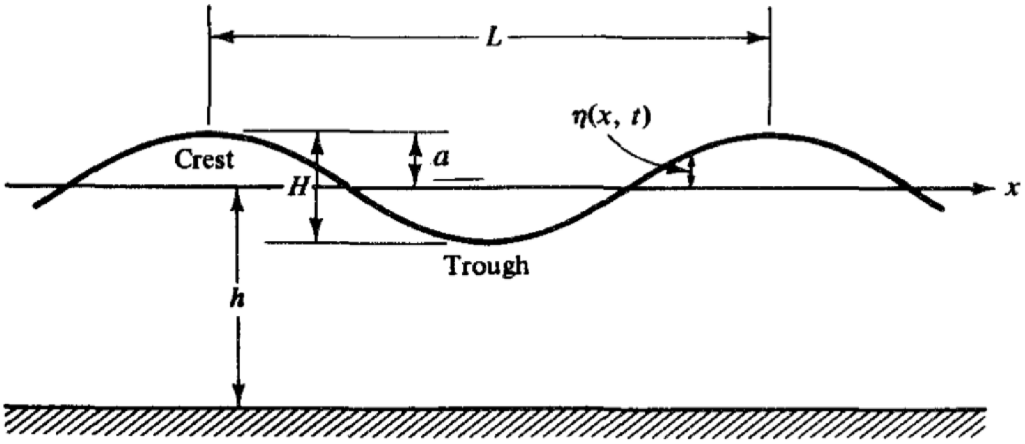


**Figure 2.2:** Wave characteristics (Dean and Dalrymple, 1991).

In addition to the aforementioned characteristics, the following dimensionless parameters should be noted:

- **wave steepness:** represents the relationship between wave height ($H$) and wavelength ($L$);
- **relative depth:** represents the relationship between depth ($h$) and wavelength ($L$);
- **relative wave height:** represents the relationship between wave height ($H$) and depth ($h$);
- **Ursell number:** parameter that indicates the degree of non-linearity of a wave. It is represented by the relation $L^2H/h^3$.

There are several theories developed in an attempt to describe ocean waves, where several factors are taken into account, such as depth, slope of the seabed, wave amplitude, wavelength, among other factors. It is worth mentioning, however, that these theories are not applicable to every type of situation, since some assumptions and physical simplifications are made. Therefore, it is necessary to understand these theories for their proper applications.

### 2.1.1 Airy wave theory

Dean and Dalrymple (1991) state that several classical physical problems and most analytical engineering problems can be posed as a boundary value problem, whose formulation is the expression in mathematical terms of physical situation, so that a unique solution exists.

The solution of hydrodynamic equations that describe the motion of waves is considerably complex and involves non-linear terms. Fortunately, a linear approximation of these equations is a good model for ocean waves in many situations (Holthuijsen, 2010). This is linear wave theory, also known as small amplitude wave theory, formulated by Airy (1845). It is applicable when the flow analyzed is composed of

monochromatic waves, in a horizontal, stationary and impermeable bottom channel, whose amplitude is relatively small and can be considered negligible, compared to the depth and wavelength.

Since the fluid analyzed in this physical problem is water, it can be said that this fluid is inviscid and incompressible (or non-divergent), and the flow is irrotational. This implies that there exists a velocity potential ($\phi$) that satisfies the continuity equation (Dean and Dalrymple, 1991):

$$\nabla^2\phi = 0 \tag{2.1}$$

Thus, the governing differential equation of a flow in a two-dimensional channel is the continuity equation expressed by the Laplace equation (Dean and Dalrymple, 1991):

$$\frac{\partial^2\phi}{\partial x^2} + \frac{\partial^2\phi}{\partial z^2} = 0 \tag{2.2}$$

where $\phi$ represents the velocity potential, $x$ represents a horizontal direction, and $z$ represents a vertical direction.

There are usually a multitude of solutions to said differential equation, whereas there must be a selection of one or more solutions that are relevant to the physical problem under investigation. This selection is achieved through boundary conditions, where solutions that are not compatible with these conditions are rejected (Dean and Dalrymple, 1991). The physical problem can be analyzed in a segment of a two-dimensional channel, as represented in figure 2.3. Boundary conditions are then imposed on the domain boundaries, which are water free surface, lateral boundaries, and the bottom.

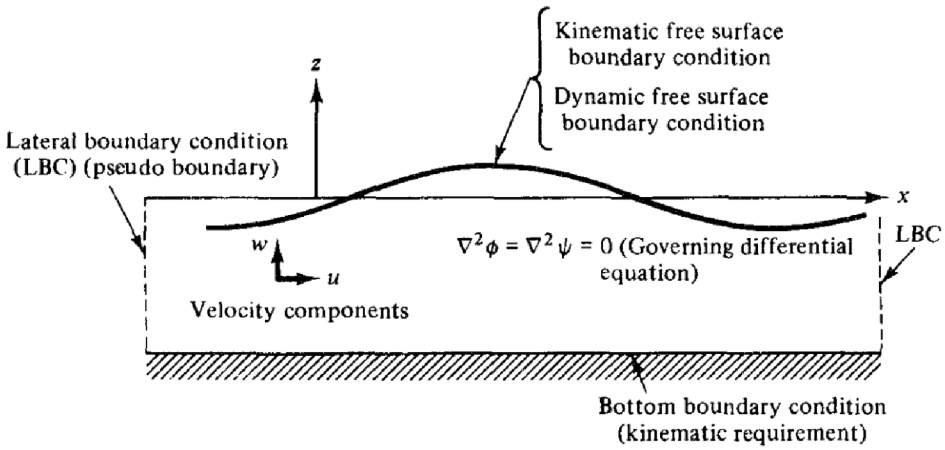


**Figure 2.3:** Wave channel where two-dimensional waves are represented as a boundary value problem (Dean and Dalrymple, 1991).

### *Kinematic bottom boundary condition*

Kinematic boundary conditions are based on the fact that there is no flow through the surface. To describe a surface, the function $F$ that represents this surface is (Dean and Dalrymple, 1991):

$$F(x,\ y,\ z,\ t) = 0 \tag{2.3}$$

whose total derivative, considering an Eulerian reference system, is:

$$\frac{DF(x,\ y,\ z,\ t)}{Dt} = \left(\frac{\partial F}{\partial t} + u\frac{\partial F}{\partial x} + v\frac{\partial F}{\partial y} + w\frac{\partial F}{\partial z}\right)\Bigg|_{F(x,\,y,\,z,\,t)=0} = 0 \tag{2.4}$$

where $x$, $y$ and $z$ represent directions in a Cartesian plane, $t$ represents time, and $u$, $v$ and $w$ represent components of the velocity potential function $\phi$. Equation (2.4) can also be represented by:

$$-\frac{\partial F}{\partial t} = \vec{v} \cdot \nabla F \tag{2.5}$$

where $\vec{v}$ represents the vector velocity, encompassing $u$, $v$ and $w$ velocity components.

Since the channel is two-dimensional and the bottom can be considered stationary, the equation representing the bottom surface can be given by:

$$F(x,\ z) = z + h(x) = 0 \tag{2.6}$$

The gradient term in equation (2.6) then becomes:

$$\nabla F = \frac{\partial F}{\partial x}i + \frac{\partial F}{\partial z}k \tag{2.7}$$

$$\nabla F = \frac{dh}{dx}i + 1k \tag{2.8}$$

Replacing it in equation (2.5), we have:

$$0 = \vec{v} \cdot \nabla F \tag{2.9}$$

$$0 = u\frac{dh}{dx} + w \tag{2.10}$$

$$w = -u\frac{dh}{dx}\Bigg|_{z=-h(x)} \tag{2.11}$$

Therefore, for a horizontal bottom, at $z = -h$, the kinematic bottom boundary condition is:

$$w = 0 \tag{2.12}$$

### *Kinematic Free Surface Boundary Condition*

A kinematic boundary condition is also applied to the free surface of the fluid. For this, the function that represents this surface is (Dean and Dalrymple, 1991):

$$F(x,\ z,\ t) = z - \eta(x,\ t) = 0 \tag{2.13}$$

Therefore, we have the total derivative of this function, considering an Eulerian reference system:

$$\frac{DF(x,\ z,\ t)}{Dt} = \frac{\partial F}{\partial t} + u\frac{\partial F}{\partial x} + w\frac{\partial F}{\partial z} = 0 \tag{2.14}$$

$$-\frac{\partial \eta}{\partial t} - u\frac{\partial \eta}{\partial x} + w = 0 \tag{2.15}$$

Thus, for $z = \eta(x, t)$, we have the kinematic free surface boundary condition:

$$w = \frac{\partial \eta}{\partial t} + u\frac{\partial \eta}{\partial x}\bigg|_{z=\eta(x,t)} \tag{2.16}$$

### *Dynamic Free Surface Boundary Condition*

Free surfaces, such as the water-air interface, are not able to withstand variations in pressure along this interface and therefore must react to maintain uniform pressure. Therefore, free surfaces require a second boundary condition to assign pressure distributions on this boundary (Dean and Dalrymple, 1991).

There are several levels of interaction between water, air and atmospheric pressure on the free surface: the wind can act on the surface through viscous tensions and pressure; the wave can propagate, without suffering any action from the wind, thus not affecting the distribution of applied surface pressure; and the pressure can be considered uniform, where free waves can exist. For the linear wave theory, the most simplified hypothesis is adopted. In this way, the Bernoulli equation is used on the free surface, considering a constant pressure (Dean and Dalrymple, 1991):

$$-\frac{\partial \phi}{\partial t} + \frac{1}{2}\left[\left(\frac{\partial \phi}{\partial x}\right)^2 + \left(\frac{\partial \phi}{\partial z}\right)^2\right] + \frac{p_\eta}{\rho} + gz = C(t) \tag{2.17}$$

where $p_\eta$ represents the surface pressure, $\rho$ is density, and $g$ is the gravitational acceleration.

It is important to mention that the solution involves considering that the wave amplitude is very small, which implies that second and higher order terms can be neglected. Therefore, with $p_\eta = 0$, in $z = \eta$, we have the dynamic free surface boundary

condition:

$$-\frac{\partial \phi}{\partial t} + g\eta = 0 \tag{2.18}$$

$$\eta = \frac{1}{g}\left(\frac{\partial \phi}{\partial t}\right)\Bigg|_{z=0} \tag{2.19}$$

### *Lateral Boundary Condition*

As indicated in figure 2.3, this condition is imposed at the sides of the domain. For simplification purposes, the linear theory of waves considers that waves are periodic in time and space, and propagate only in the positive direction of the Cartesian axis $x$. This condition states that the velocity potential function ($\phi$) is repeated in the wavelength ($L$), in the period of the wave ($T$), and is represented as follows (Dean and Dalrymple, 1991):

$$\phi(x,\ t) = \phi(x + L,\ t) \tag{2.20}$$

$$\phi(x,\ t) = \phi(x,\ t + T) \tag{2.21}$$

### *Solution for a progressive wave*

Finally, applying the boundary conditions at the boundaries of the domain, we have a non-linear problem, which is linearized assuming that the waves are of small amplitude and with constant depth. This way, it is possible to arrive at the formulations of the velocity potential ($\phi$), velocity components ($u$ and $w$) and free surface elevation($\eta$) (Dean and Dalrymple, 1991):

$$\phi(x,\ z,\ t) = -\frac{H}{2}\frac{g}{\sigma}\frac{cosh[k(h+z)]}{cosh(kh)}sin(kx - \sigma t) \tag{2.22}$$

$$u = \frac{\partial \phi}{\partial x} = \sigma\frac{H}{2}\frac{cosh[k(h+z)]}{sinh(kh)}cos(kx - \sigma t) \tag{2.23}$$

$$w = \frac{\partial \phi}{\partial z} = \sigma\frac{H}{2}\frac{sinh[k(h+z)]}{sinh(kh)}sen(kx - \sigma t) \tag{2.24}$$

$$\eta(x,\ t) = \frac{H}{2}cos(kx - \sigma t) \tag{2.25}$$

In equations (2.22–2.25), $k$ and $\sigma$ represent, respectively, the wave number and the angular frequency of the wave, given by:

$$k = \frac{2\pi}{L} \tag{2.26}$$

$$\sigma = \frac{2\pi}{T} \tag{2.27}$$

### 2.1.2 Stokes Wave Theory

Nonlinear wave theories represent waves in a less idealized and a more realistic way, providing the study of larger waves at smaller depths. Linear theory, applied to small amplitude waves, is limited to wave slopes ($H/L$) less than 0.05 and to a relative depth ($h/L$) greater than 0.01 (U.S. Army Corps of Engineers, 2002). Thus, other theories are necessary for more complex situations.

Stokes wave theory is applicable for waves in intermediate or deep waters, with higher wave heights. This theory uses the perturbation method in the governing equations of the flow, where non-linear terms are added to the linear theory solution, so that the perturbation expansion for the velocity potential ($\phi$) and for the free surface elevation ($\eta$) are represented as follows (Dean and Dalrymple, 1991):

$$\phi = \epsilon\phi_1 + \epsilon^2\phi_2 + \epsilon^3\phi_3 + ... \tag{2.28}$$

$$\eta = \epsilon\eta_1 + \epsilon^2\eta_2 + \epsilon^3\eta_3 + ... \tag{2.29}$$

where $\epsilon$ represents the perturbation expansion parameter, in which:

$$\epsilon = ka \tag{2.30}$$

It is important to note that the solution in which only the first order term ($\phi_1$) is present (where non-linear terms are disregarded) corresponds to the linear wave theory. The expansion of this series to the second-order term ($\phi_2$) is called second-order Stokes theory, if it is up to the third-order term ($\phi_3$), it becomes third-order Stokes theory, and so on (U.S. Army Corps of Engineers, 2002).

From the second-order theory onwards, superharmonic components appear, that is, higher frequency components 2, 3, etc. times the fundamental frequency, which leads to higher crests and flatter troughs (Carneiro, 2007).

As depth decreases and waves enter shallow water, the degree of non-linearity of these waves increases and other theories are needed to describe their behavior. The most representative wave theories for greater relative depths or about to break are cnoidal waves and solitary waves. U.S. Army Corps of Engineers (2002) shows the waveform according to the theories that describe them (figure 2.4), as well as a graph of applicability of theories (figure 2.5). More information on Stokes wave theory can be found in Stokes (1847) and Fenton (1985).

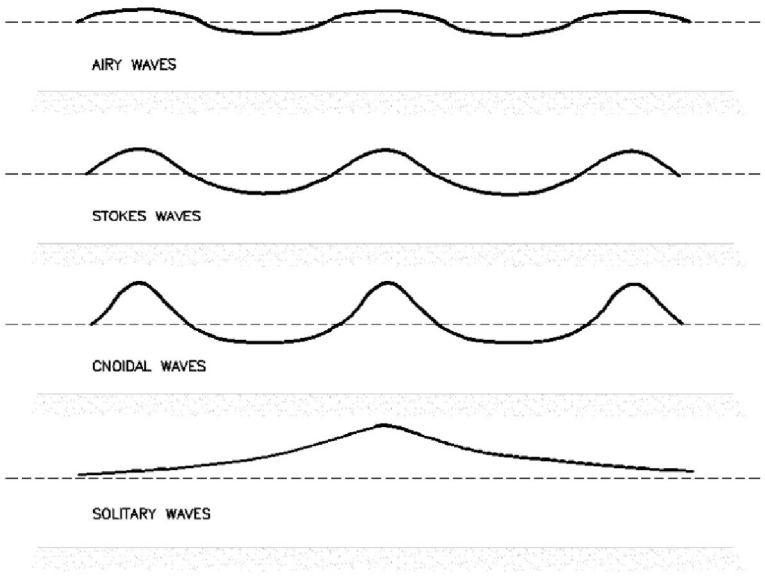


**Figure 2.4:** Wave profile shape of different progressive gravity waves (U.S. Army Corps of Engineers, 2002).

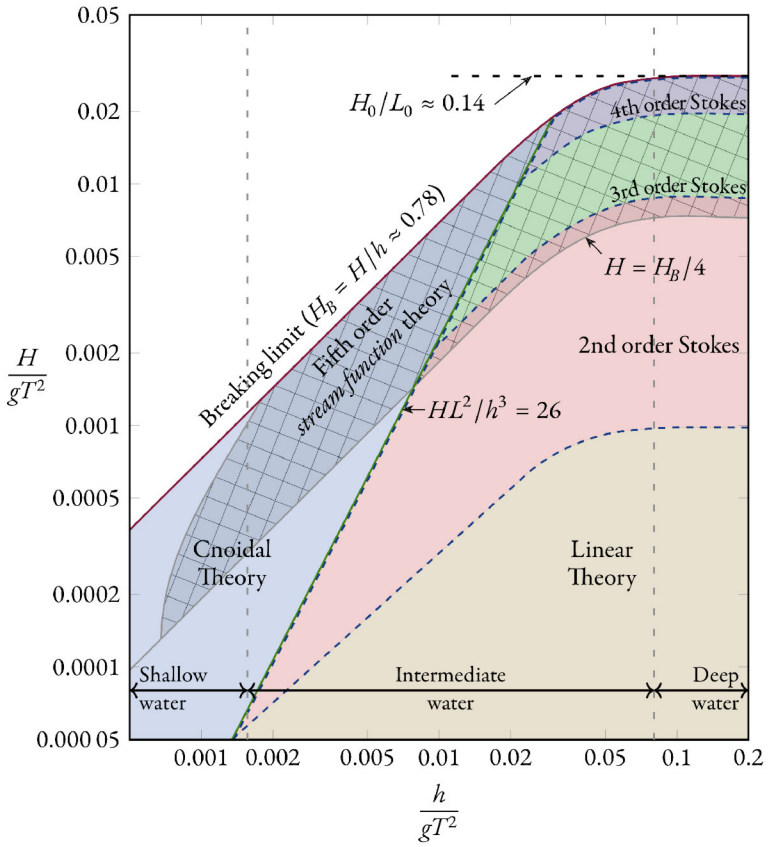


**Figure 2.5:** Wave theory applicability chart. Adapted from U.S. Army Corps of Engineers (2002).

## 2.2 Wave Energy

Energy is a fundamental element in the everyday life of modern society. Numerous activities, such as internet access, household chores, lighting, air conditioning, leisure, transport, among others, make use of this element. These activities therefore need some form of energy to be performed.

Until the Industrial Revolution, energy production came from the use of firewood, animal traction and wind for navigation. In the second half of the $18^{th}$ century and the beginning of the $19^{th}$ century, however, the use of steam engines, electric energy and fossil fuels gained space, which led to a great industrial and technological revolution (Rodrigue, 2020).

The rapid and constant creation of new equipment, technologies and devices increasingly demanded an intense production of electrical energy. Allied to this, the intensive use of non-renewable fossil fuels (such as coal, oil and natural gas) was the predominant contributor to global warming and climate change, releasing carbon dioxide ($CO_2$) (Vural, 2020). In this vein, the 1973 oil crisis induced a major change in the renewable energy scenario and increased interest in large-scale production of energy from the oceans (Falcão, 2012).

There are several ways to classify energy from waves, as well as the devices that extract it. Ocean or marine energy can be divided according to its origin or characteristics: tides, waves, currents, thermal gradients and salinity gradient (Ben Elghali, Benbouzid, and Charpentier, 2007 and Uihlein and Magagna, 2016). Falnes (2007) further states that wave energy conversion, due to its different proposals and principles, can be classified in three ways:

- device location in relation to the bathymetry and distance from the coast;
- device position in relation to the sea level;
- device size and orientation.

According to the first classification, devices can be onshore, whose energy distribution is relatively easy, but with lower energy potential; near shore devices, whose energy potential is greater than onshore devices, but its energy distribution capacity is more expensive; and offshore devices, whose energy potential is high, however, present difficulties of access for installation and maintenance, in addition to longer distances to transport the generated energy, causing greater losses through energy transmission cabling (Kirinus, 2017).

In the second classification, Falnes (2007) classifies the devices as floating, submerged, or bottom-standing, according to their position in relation to sea level. This author also classifies the devices according to their size and orientation; if its extension is very small compared to the wavelength, this device is called point absorber; if, on the other hand, this device is comparable to or greater than one wavelength, it is called line absorber, which is, in turn, subdivided into attenuator or terminator.

Falcão (2008), in turn, classifies devices according to their working principles.

This classification can be observed in table 2.1 and the mentioned devices can be seen in figure 2.6.

**Table 2.1:** Classification of wave energy conversion technologies (Falcão, 2008).

| Physical principle | Position | Characteristic |
|---|---|---|
| **Oscillating Bodies** | Submerged | Essentially translation. Ex: AWS |
| | | Rotation through bottom-hinged plates. Ex: WaveRoller, Oyster |
| | Floating | Essentially translation. Ex: AquaBuoy e WaveBob |
| | | Essentially rotation. Ex: Pelamis |
| **Oscillating Water Column** | Fixed Structure | Isolated. Ex: Limpet |
| | | In breakwater. Ex: Mutriku |
| | Floating structure | Ex: Mighty Whale |
| **Overtopping** | Fixed structure | Shoreline. Ex: Tapchan |
| | | In breakwater. Ex: SSG |
| | Floating structure | Ex: Wave Dragon |

## 2.3 Oscillating Water Column Wave Energy Converter

Among the various types of wave energy converter (WEC) devices, which convert sea wave energy into electrical energy (see table 2.1 and figure 2.6), whether in design phase, in test phase, or in pre-commercial phase, the Oscillating Water Column (OWC) type device is possibly the more extensively studied (Falcão and Henriques, 2016), due to its simplicity and conversion potential.

An OWC device is basically composed of four parts, namely the hydropneumatic chamber, turbine duct, turbine and generator. The hydropneumatic chamber, which can be fixed or floating, is a structure whose bottom is open, below water surface, which retains the trapped air inside the chamber and above the free surface; the movement of the waves then causes the air to be continuously compressed and decompressed, which causes it to flow through a turbine coupled to a generator (Falcão and Henriques, 2016). A representative diagram of the operation of this device can be seen in figure 2.7

The first OWC device was developed by Yoshio Masuda (1925-2009) in 1965, a Japanese naval officer considered the father of modern wave technology. This device

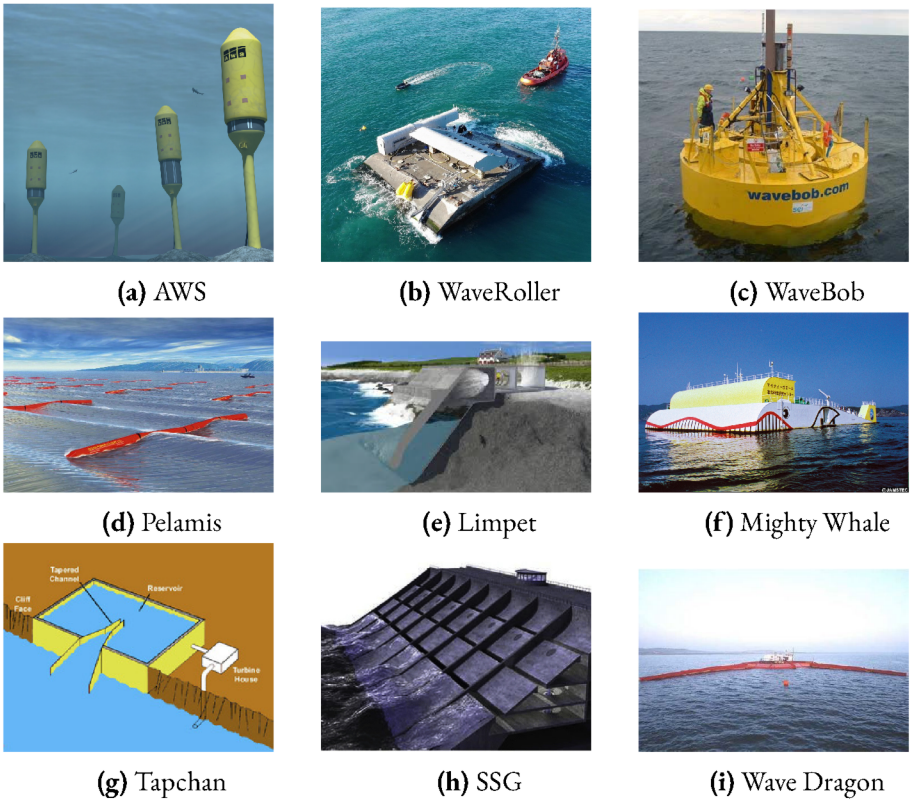


**(a)** AWS **(b)** WaveRoller **(c)** WaveBob

**(d)** Pelamis **(e)** Limpet **(f)** Mighty Whale

**(g)** Tapchan **(h)** SSG **(i)** Wave Dragon

**Figure 2.6:** Wave energy converter devices mentioned in table 2.1 (Falcão, 2014).

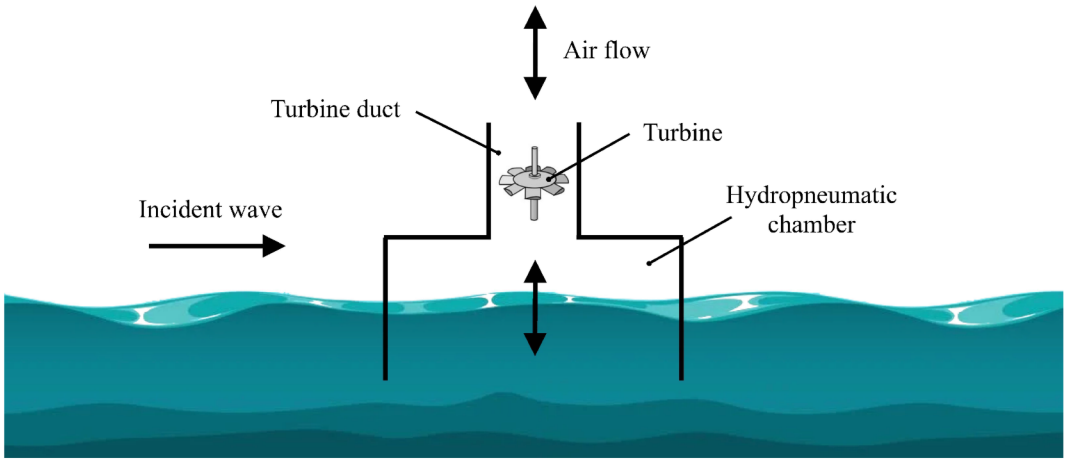


**Figure 2.7:** Illustration of the operational principle of an Oscillating Water Column device (Maciel *et al.*, 2021).

was a navigation buoy powered by wave energy, equipped with a unidirectional air turbine, which was actually what was later named an OWC (floating) (Falcão and Henriques, 2016). In 1978, Masuda created the Kaimei (figure 2.8 for the Japan Marine Science and Technology Center, the first large-scale wave energy conversion device. This was a large barge that featured thirteen OWC devices built into the hull.


**Figure 2.8:** Kaimei barge (Falcão and Henriques, 2016).

In 1983, following Masuda's pioneering devices, a prototype of a fixed onshore OWC device equipped with a 40 kW Wells turbine was installed on Sanze Beach in Tsuruoka City, Japan, where it operated for six months before being taken out of service in 1984 (Bhattacharyya and McCormick, 2003 and Falcão and Henriques, 2016).

In 1985, a Norwegian government program installed a full-size OWC device attached to a cliff at Toftestallen, near the city of Bergen (figure 2.9). This device had a vertical axis Wells turbine and had an estimated capacity of 500 kW. Unfortunately, the device was destroyed in 1988 during a storm, due to a failure in the bolted connection of the steel structure to the concrete foundation (Falcão and Henriques, 2016).

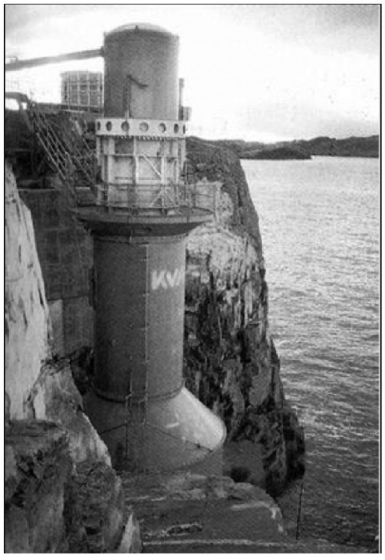

**Figure 2.9:** OWC device in Toftestallen, near Bergen, Norway (Falcão and Henriques, 2016).

In 1988, a scheme consisting of 10 OWC devices was installed in front of an

existing breakwater in the city of Kujukuri, Chiba, Japan. In this plant, the air expelled by each device was distributed in a pressurized reservoir and used to drive a 30 kW turbine, used as a supplementary energy source for a flounder farm (Graw, 1996; Thorpe, 1999 and Bhattacharyya and McCormick, 2003).

In 1990, two more prototypes were installed in Asian countries. A device with an estimated capacity of 60 kW, integrated into a breakwater in the port of Sakata, Japan (figure 2.10a); and another, with a fixed bottom and estimated capacity of 125 kW, was installed in Trivandrum, India (figure 2.10b).


**(a)** OWC device in Sakata port, Japan.

**(b)** OWC device in Trivandrum, India.

**Figure 2.10:** Devices installed in India and Japan, in 1990 (Falcão and Henriques, 2016).

In 1991, a prototype of an OWC device, with academic purposes and capacity of 75 kW (figure 2.11), was commissioned to be installed on the Isle of Islay, Scotland (Whittaker *et al.*, 1997).

**Figure 2.11:** Prototype of an OWC device, on the Isle of Islay, Scotland (Falcão and Henriques, 2016).

China began testing the OWC device in 1990 on Dawashan Island in Zhuhai, Guangdong Province, with a 3 kW prototype, which provided electricity to the island's local community. Five years later, a 20 kW turbine was added and, finally, in 2001 a device with a capacity of 100 kW was installed at the station, the installation of which can be seen in figure 2.12 (Zhang, Li, and Lin, 2009).

**Figure 2.12:** OWC Device on Dawashan Island in Zhuhai, Guangdong Province, China (Zhang, Li, and Lin, 2009).

In 1995, a prototype of a nearshore, fixed-bottom OWC device, named OSPREY (Ocean Swell Powered Renewable EnergY), was launched, towed and installed near Dounreay, Scotland, United Kingdom. However, the device, with an estimated capacity of 1 MW, suffered a structural failure before it could be safely installed (Thorpe, 1999).

In 1996, a 130 kW prototype was deployed in Haramachi, Japan. This prototype used rectifier valves to control the flow of air from and to the turbine to produce constant power (Thorpe, 1999 and Bhattacharyya and McCormick, 2003).

With the inclusion of wave energy in its research and development program, the European Commission initiated in 1991 studies that led to the construction of two fixed OWC devices. The first, located on the island of Pico, in Azores, Portugal (figure 2.13a), was completed in 1999 and had an estimated capacity of 400 kW (Falcão, 2000). The second, named LIMPET (Land Installed Marine Pneumatic Energy Transformer), gave rise to the prototype installed on the Isle of Islay (figure 2.14), and was completed in 2000, with an estimated capacity of 500 kW (Heath, Whittaker, and Boake, 2000 and Falcão and Henriques, 2016). Unfortunately, after a storm on April 17, 2018, the Pico plant suffered significant structural damage (figure 2.13b) and, due to lack of financial support, it was dismantled in 2018 (Doyle and Aggidis, 2019 and Falcão *et al.*, 2020).

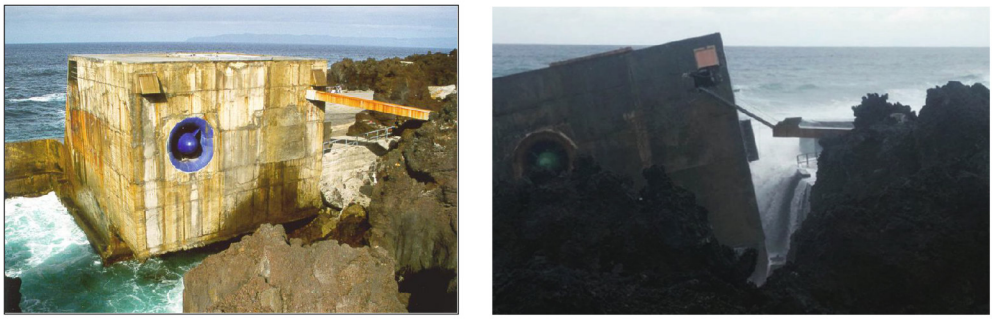

**(a)** Device rear view (Falcão, 2000).

**(b)** Device after collapse (Falcão *et al.*, 2020).

**Figure 2.13:** OWC device on Pico island, Azores, Portugal before and after the partial collapse that took place on April 17, 2018.

**Figure 2.14:** LIMPET OWC device from the Isle of Islay, Scotland, United Kingdom (Heath, Whittaker, and Boake, 2000).

After analyzing various design options, the Spanish government approved, in 2004, the project that began the construction of a multi-chamber OWC structure integrated into the breakwater of the port of Mutriku. The structure began operating in 2011 and has 16 device chambers, as well as 16 Wells turbines with 18.5 kW each, totaling 300 kW (Torre-Enciso *et al.*, 2009).

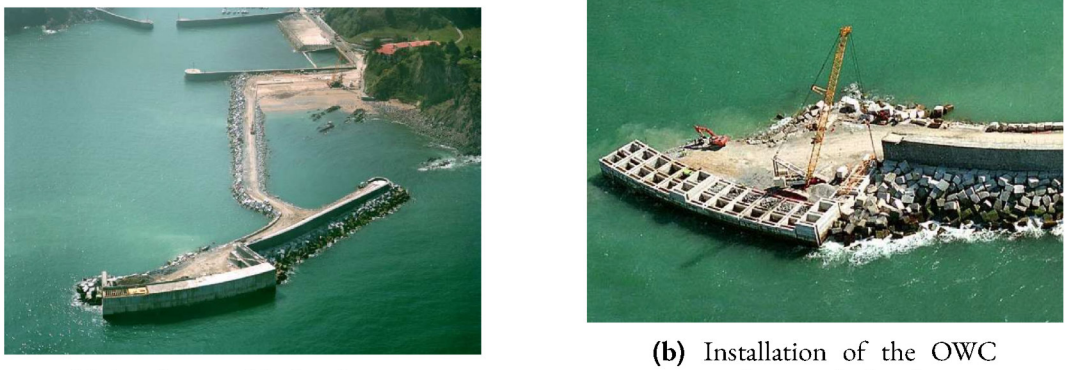

**(a)** Aerial view of the breakwater.

**(b)** Installation of the OWC power plant on the breakwater.

**Figure 2.15:** Multi-chamber OWC power plant integrated into a breakwater in the port of Mutriku, Spain (Torre-Enciso *et al.*, 2009).

Count and Evans (1984) claim that the process of absorbing wave energy can be improved by extending the chamber structure, projecting walls (natural or artificial) in the direction of the waves, forming a port or a collector. In 2005, the Australian company Energetech developed a technology using a large parabolic shaped collector for this purpose; a nearshore prototype with an estimated capacity of 500 kW, Oceanlinx Mk1 (figure 2.16), was tested at Port Kembla, in Wollongong, Australia (Falcão and Henriques, 2016).

**Figure 2.16:** Oceanlix Mk1 OWC device, in Wollongong, Australia (Falcão and Henriques, 2016).

Since 2006, a 12-meter long prototype (figure 2.17), at 1:4 scale, and equipped with a horizontal axis Wells turbine (and later an impulse turbine) has been tested in protected maritime waters of Galway Bay, Western Ireland (Portillo *et al.*, 2019). This prototype is, in fact, a modified version of an OWC device, named BBDB (Backward Bent Duct Buoy), in which the OWC duct is bent backwards from the incident wave direction (it was found to be more advantageous compared to the forward facing duct version). This way, the length of the water column can be large enough for resonance to be achieved, keeping the draught of the floating structure within acceptable limits (Falcão, 2014 and Portillo *et al.*, 2019).

**Figure 2.17:** BBDB device in Galway Bay, Ireland (Falcão, 2014).

In 2010, the Australian company Oceanlinx, formerly known as Energetech, deployed in Port Kembla, Australia, a one-third scale prototype of its latest OWC device, the Mk3 (figure 2.18). This device is connected to the power distribution network and it is a floating platform with several OWC chambers (in this case, eight chambers), each with an air turbine (Falcão, 2014).

**Figure 2.18:** Mk3 floating platform with multiple OWC chambers at Port Kembla, in Wollongong, Australia (Falcão, 2014).

In 2012, the U-OWC REWEC3 (Resonant Wave Energy Converter 3) device was designed to be installed in Civitavecchia port, Rome, Italy (figure 2.19), whose construction was completed in 2015. Compared to a traditional OWC, a U-OWC device includes an additional vertical duct, which allows to adjust the fundamental frequency of the device to the peak period of pressures of waves acting on the breakwater converter. This way, resonance conditions can be achieved without phase control devices and wave pressures on the air in the chamber are increased in amplitude, amplifying the performance of the device (Arena *et al.*, 2013).

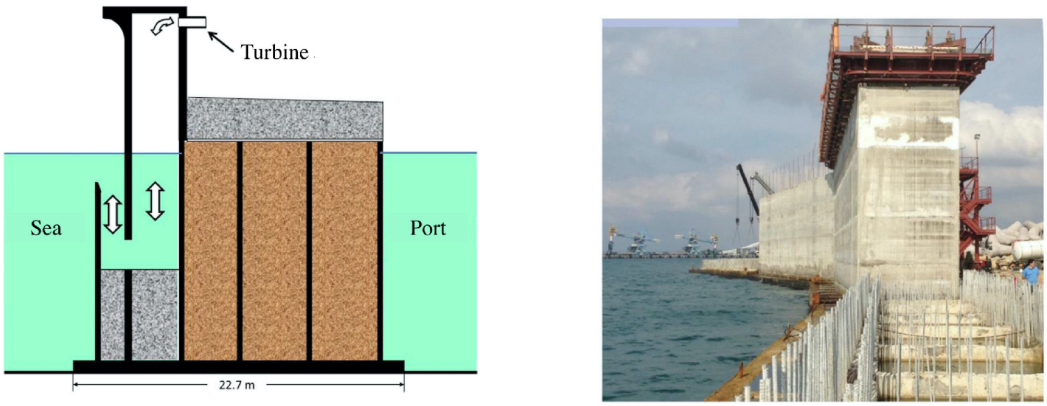


**Figure 2.19:** REWEC3 U-OWC device being built, in Civitavecchia port, Rome, Italy (Falcão and Henriques, 2016).

In 2014, Oceanlinx launched a 1 MW prototype of the greenWAVE device in Port Adelaide, Australia (figure 2.20). However, in March 2014, an accident occurred

in the airbags supporting the 3000-ton structure as the plant was being towed from Port Adelaide to Port MacDonnell in Western Australia, forcing the prototype to be stranded and preventing its deployment. In November 2014, Oceanlinx's wave energy conversion technology and all of its intellectual property were sold to a new wave energy technology developer in Hong Kong. Part of the sunken device remains in the Australian sea and will be used as an artificial coral (Falcão and Henriques, 2016; Sutton, 2017 and Offshore Energy, 2018).


**Figure 2.20:** GreenWAVE device, at Port Adelaide, Australia (Falcão and Henriques, 2016).

In 2015, a fixed-bottom OWC device was completed in South Korea (figure 2.21). Rated at 500 kW, this device was installed in Yongsoo, about 1 km off the coast of Jeju Island.

**(a)** **(b)**

**Figure 2.21:** OWC device in Yongsoo, Jeju island, South Korea (Falcão and Henriques, 2016).

A summary of the OWC devices presented can be seen in table 2.2. The lines highlighted in gray represent devices that are no longer working.

**Table 2.2:** Summary of the presented OWC devices.

| Device | Power | Country | Year | Classification | Turbine |
|---|---|---|---|---|---|
| **Masuda's navigation buoy** | - | Japan | 1965 | Floating | Unidirectional turbine |
| **Kaimei** | Below expected | Japan | 1978 | Floating | Unidirectional turbines |
| **Sanze OWC prototype** | 40 kW | Tsuruoka, Japan | 1983 | Fixed onshore | Wells turbine |
| **Toftestallen OWC device** | 500 kW | Toftestallen, Norway | 1985 | Fixed onshore | Vertical axis Wells turbine |
| **Kujukuri OWC devices** | 30 kW | Kujukuri, Japan | 1988 | Onshore fixed in breakwater | Unidirectional turbine |
| **Port of Sakata OWC device** | 60 kW | Sakata, Japan | 1990 | Onshore fixed in breakwater | Wells turbine |
| **Trivandrum OWC device** | 125 kW | Trivandrum, India | 1990 | Bottom-fixed | Wells turbine |
| **Isle of Islay OWC prototype** | 75 kW | Islay, Scotland | 1991 | Fixed onshore | Wells turbine |
| **OSPREY** | 1 MW | Dounreay, Scotland | 1995 | Fixed nearshore | Wells turbine |
| **Haramachi OWC prototype** | 130 kW | Haramachi, Japan | 1996 | Fixed onshore | Unidirectional turbine with rectifying valves |
| **Pico island OWC device** | 400 kW | Azores, Portugal | 1999 | Fixed nearshore | Wells turbine |
| **LIMPET** | 500 kW | Islay, Scotland | 2000 | Fixed nearshore | Wells turbine |
| **Dawashan island OWC device** | 100 kW | Zhuhai, China | 2001 | Fixed onshore | Unidirectional turbine |
| **Oceanlinx Mk1 prototype** | 500 kW | Port Kembla, Australia | 2005 | Bottom-fixed nearshore | - |

Continued on next page

**Table 2.2 – continued from previous page**

| Device | Power | Country | Year | Classification | Turbine |
|---|---|---|---|---|---|
| **Backward Bent Duct Buoy** | - | Galway Bay, Ireland | 2006 | Floating nearshore | Horizontal axis Well turbine |
| **Oceanlinx Mk3 device** | - | Port Kembla, Australia | 2010 | Multi-chamber floating platform | Turbines of various types |
| **Port of Mutriku OWC device** | 300 kW | Mutriku, Spain | 2011 | Multi-chamber fixed in breakwater | 16 Wells turbines |
| **Oceanlinx GreenWAVE device** | 1 MW | Port Adelaide, Australia | 2014 | Bottom-fixed | - |
| **Yongsoo OWC device** | 500 kW | Yongsoo, South Korea | 2015 | Bottom-fixed | - |
| **REWEC3 U-OWC device** | - | Rome, Italy | 2015 | U-shaped multi-chamber fixed in breakwater | 17 Wells turbines |

In addition to tests on prototypes, numerous studies related to the OWC device have been performed, which address analytical, numerical, and experimental evaluations of the device's geometric characteristics, conversion capacity, turbines used, hydrodynamic performance, device location, and energy availability. In this context, the random character of ocean waves, in which there is no characteristic period or height, makes the use of realistic sea states in numerical studies a challenge. Therefore, the use of representative regular waves for the purpose of representing sea states has been widely used. However, analysis done with regular waves can lead to results, such as available power, pressure and velocity, that do not correspond to reality (Tavares, 2019).

Thus, Ferguson *et al.* (2015) emphasize the importance of performing experiments in sea states more realistic than simple regular waves to ensure an accurate representation of the device's performance and operation. For this, the authors performed experiments with test models in an OWC device using polychromatic waves as an alternative to irregular waves. This type of waves is characterized by the superposition of regular discrete waves with a definite period, which allows the application of phase-averaging techniques and, consequently, a more realistic sea state.

Sabedra *et al.* (2017) numerically simulated the working principle of an OWC device using simulated sea state data to represent the air flow inside the device. For this, the authors used data of significant wave height in a region close to the coast of Rio

Grande, Brazil, to determine the vertical velocity variation of free surface elevation of the sea. The results presented by the authors showed the ability of this methodology to numerically simulate the fluid dynamic behavior of air flow in the converter, as well as the coherence between the velocity imposed as a boundary condition and the velocity obtained as a response of the model at the converter outlet.

Lisboa *et al.* (2018) numerically analyzed the available power of a nearshore OWC device fixed on a breakwater, with a Wells turbine, installed on the southern coast of Brazil. An analysis of the occurrence of waves in this region was performed in order to determine the significant parameters used in the numerical analysis. Considering the wave characteristics of the region, the authors found an optimal diameter of 2.25 m for the turbine and an average annual power of 36.48 kW, for a device 10 m long, 10 m wide and 16 m high (of which 10 m were submerged).

Mendonça *et al.* (2018) presented the development of an integrated tool for the numerical analysis of OWC devices installed on vertical breakwaters. This tool has as main purpose the numerical modeling of wave propagation from offshore to nearshore, of wave-structure interaction, and of complex non-linear hydrodynamic and aerodynamic phenomena that occur in OWC devices. The authors considered the potential of this tool useful in supporting ocean and coastal engineering projects, due to its ability to effectively reproduce the main phenomena involved in these types of studies.

Dai *et al.* (2019) present a study about the effect of different scales on prototypes of fixed OWC devices. For this, tank tests at two different scales were performed at the University of Strathclyde, including the scaling effect of test tanks to minimize the bias introduced by different wave blocking effects. The authors then performed numerical simulations for the two devices at different scales to investigate whether the numerical simulation would be able to reproduce the scale effect. The results found by the authors suggested that the hydrodynamic scale effect was introduced mainly by the effect of Reynolds number in the cases investigated in the study.

Zabihi, Mazaheri, and Namin (2019) employed a fully nonlinear two phase flow model using Ansys Fluent to investigate the hydrodynamics of an OWC, which was validated against a relatively large scale physical model (1:15). For that, they compared results of both free surface elevation and air pressure in the OWC chamber. The authors reached an admissible accordance between numerical and experimental model, although some discrepancies were detected in the free surface elevation inside the hydropneumatic chamber, especially for short wave periods.

Wang *et al.* (2019) investigated the performance of a small-scale OWC system consisting of two units, a fixed onshore unit and a floating vertical motion offshore unit. For this, they analyzed the effects of widths of the two chambers, the vertical restraint force, the submersion depth in the rear wall of the floating device, the space between the two devices and the wave energy conversion efficiencies. The authors came to the conclusion that the floating device with a stronger vertical holding force is more satisfactory for better system performance; in addition, a relatively small space

between devices is best recommended in the design and construction phase.

Gaspar, Teixeira, and Didier (2020) performed a numerical analysis of the performance of two fixed onshore OWC devices, with different slopes of the front and rear walls. In one of the devices, front and rear walls are vertical and in the other, these walls have a slope of 40° in relation to the horizontal plane. In this study, the authors performed analyses of hydrodynamic behavior, of fluid-structure interaction outside and inside the chamber, and of energy distribution. The results presented showed that the device with sloping walls had the best efficiency, however, the device with vertical walls showed less variation in efficiency in the wave period interval than the previous one, which may be interesting in sea states where wave energy changes from short to long periods.

Kim *et al.* (2020) analyzed the hydrodynamic characteristics of an inclined OWC device. For this, these authors developed a numerical method of temporal domain based on a three-dimensional velocity potential, which was used to analyze the hydrodynamic characteristics of an inclined OWC chamber, such as the movement of the water column and the three-dimensional flow distribution around the chamber.

Fox, Gomes, and Gato (2021) studied the design of an OWC device if it were integrated into a caisson used for breakwaters. For this, they developed a numerical model based on linear potential flow theory, and analyzed the device performance under the action of irregular waves. They also analyzed the influence of the submerged duct, air chamber, and turbine with three different duct configurations: conventional, U-shape, and L-shape. The authors found that the U-shaped converter outperforms the other configurations, with a maximum theoretical annual pneumatic power of 46.8 kW/m, against power values of 39.4 kW/m and 38.0 kW/m for the L-shape and conventional device, respectively.

Maciel *et al.* (2021) performed a numerical study, reproducing a case from the laboratory experiment performed by Zabihi, Mazaheri, and Namin (2019), which contained a laboratory-scale OWC device in a numerical channel. The numerical simulations performed aimed to validate the methodology proposed by Machado *et al.* (2017), which uses transient velocity data as a means to impose velocity boundary condition for the generation of numerical waves. The authors were able to validate the mentioned methodology.

Machado *et al.* (2021) developed the WaveMIMO methodology, which allows the numerical simulation of irregular waves with realistic characteristics. This methodology converts wave spectra data into time series of free surface elevations treated and processed as wave propagation velocities in horizontal and vertical directions. The authors then simulated the incidence of irregular realistic waves over an OWC device, using processed discrete transient data of wave propagation velocity as boundary conditions on a wave channel in Fluent.

Cong *et al.* (2021) approaches a new combined concept, consisting of an OWC device, where chamber is divided into four fan-shaped sub-chambers; and an offshore wind turbine for the multi-purpose utilization of offshore renewable energy resources.

The authors found that a significant energy extraction efficiency was attained when remarkable piston-like fluid motion was induced within each sub-chamber, and the wave power absorption by the OWC was not restricted by wave direction. They also found that air compressibility makes a negative effect on the wave power absorption especially when the wave frequency is less than the resonance frequency of the piston-mode motion of the fluid in the chamber.

Santos *et al.* (2022) performed a numerical study of an OWC device considering three different configurations of a Savonius turbine in the turbine duct region, subjected to turbulent flows. Initially, a free turbine inserted in a long and large channel was analyzed for verification and validation of the model. Next, an enclosure domain that mimics an OWC device with a constant velocity at its inlet was simulated and, then, the same domain as in the previous scenario but with sinusoidal velocity imposed at the inlet. The model developed by the authors led to promising results, predicting similar time–spatial-averaged power coefficients as those obtained in the literature for different magnitudes of the tip speed ratio ($0.75 \leq \lambda \leq 2.00$). The imposition of sinusoidal velocity led to a similar performance as that obtained for constant velocity.

Zhou *et al.* (2022) numerically investigated the hydrodynamic response of a land-based OWC wave energy converter under various irregular wave conditions. The influence of irregular waves was carried out by comparison with regular waves, wherein a number of significant wave heights and peak wave periods were considered. The authors observed that the hydrodynamic efficiency of the OWC device in irregular wave conditions was lower than that in regular waves for most wave frequencies, especially near the resonant frequency.

## 2.4 Finite Volume Method

As mentioned in section 2.1.1, most analytical engineering problems can be posed as a boundary value problem, whose formulation is the expression of physical phenomena in mathematical terms, such that a unique solution exists (Dean and Dalrymple, 1991). In general, the methods that make it possible to solve this type of problem can be classified into analytical or numerical (discrete) methods (Kolditz, 2002).

The analytical solution of any physical problem would make it possible to calculate values of the variables involved at an infinitesimal level, that is, for an infinite number of points. However, when you have a numerical solution, there is actually a solution for a discrete number of points, where the greater the number of points, the closer to the exact solution it will be, which results in an increase of computational effort involved (Maliska, 2004).

Analytical solutions can be obtained for problems involving linear equations and domains with simple geometry; however, for nonlinear equations, or problems with complex geometry or boundary conditions, exact solutions generally do not exist, and approximate solutions must be found (Kolditz, 2002).

The growing development of increasingly powerful and efficient machines has become a great ally of scientists and researchers, since computers can perform large-scale calculations and simulations, which were once insoluble. The wide acceptance of numerical models by the community interested in solving these problems is explained by the great versatility and relative simplicity of application of these techniques (Maliska, 2004).

In this context, computational fluid dynamics (CFD) is presented, whose function is the analysis of systems involving fluid flow, heat transfer, and associated phenomena, such as chemical reactions, through computer simulations (Versteeg and Malalasekera, 2007).

Numerical simulations employ numerical methods in its resolution, whose task, in turn, is to solve one or more differential equations, replacing the existing derivatives in the equation by algebraic expressions involving the unknown function; the way to obtain these algebraic equations is to characterize the type of numerical method (Maliska, 2004). Figure 2.22 shows how an element is discretized, that is, how the differential equation defined for domain D is transformed into a system of algebraic equations.

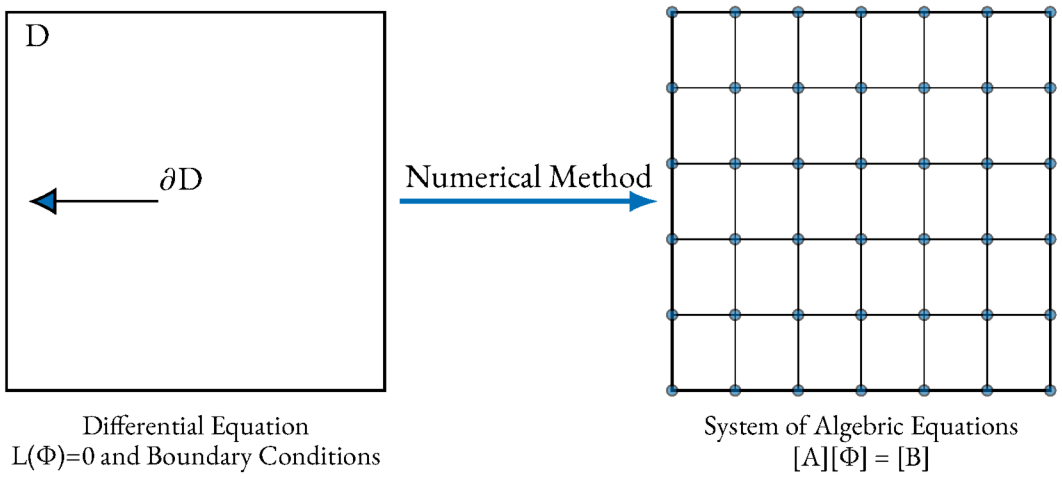


**Figure 2.22:** Discretization of an element or volume through numerical method (Maliska, 2004).

There are different numerical solution methods, such as: finite difference method, finite element method, method of moments, analytic element method, finite layer method, spectral method, and finite volume method. In this work, only the finite volume method (FVM) will be addressed, whose performance is an essential part in well-established CFD codes such as Phoenics[1], Star-CD[2], Ansys CFX[3], and the software used in this study, Fluent[4] (Versteeg and Malalasekera, 2007).

[1] http://www.cham.co.uk/phoenics.php
[2] http://www.cd-adapco.com/products/star_cd/
[3] https://www.ansys.com/products/fluids/ansys-cfx
[4] https://www.ansys.com/products/fluids/ansys-fluent

When employing a method, there are two ways to obtain approximate equations. The first deals with the balance of the property analyzed by the method inside elementary (or finite) volumes, and the second is the integration of the differential equation in conservative form over the elementary volume, in space and time (Maliska, 2004).

The differential equation describing conservation of mass is given by (Maliska, 2004):

$$\frac{\partial \rho}{\partial t} + \frac{\partial \rho u}{\partial x} + \frac{\partial \rho v}{\partial y} + \frac{\partial \rho w}{\partial z} = 0 \tag{2.31}$$

Or simply:

$$\frac{\partial \rho}{\partial t} + \nabla.(\rho \vec{v}) = 0 \tag{2.32}$$

For a two-dimensional elementary volume (figure 2.23), in steady state, we have:

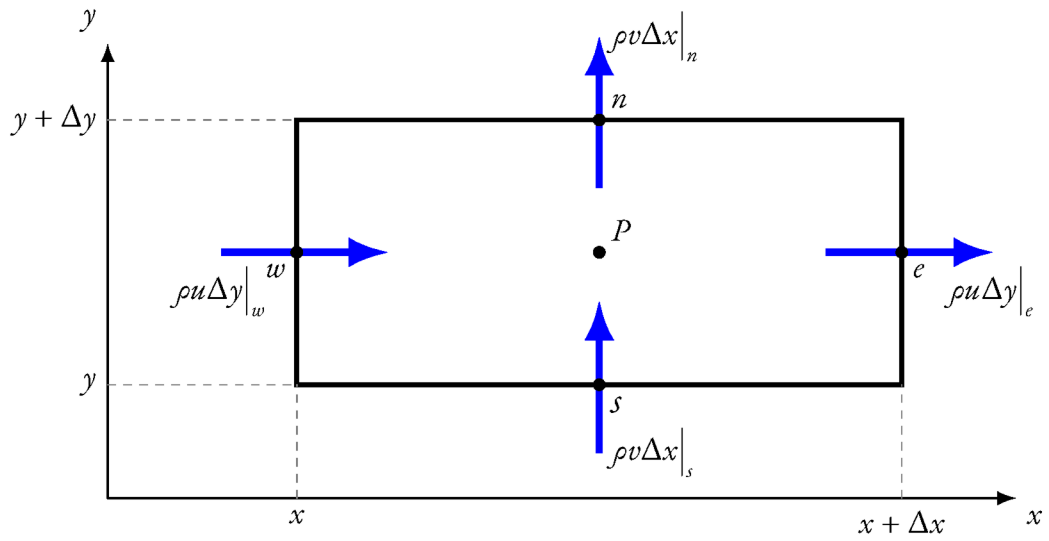


**Figure 2.23:** Generic control volume. Adapted from (Maliska, 2004).

$$\frac{\partial \rho u}{\partial x} + \frac{\partial \rho v}{\partial y} = 0 \tag{2.33}$$

$$\rho u \Delta y\Big|_e - \rho u \Delta y\Big|_w + \rho v \Delta x\Big|_n - \rho v \Delta x\Big|_s = 0 \tag{2.34}$$

$$\dot{m}_e - \dot{m}_w + \dot{m}_n - \dot{m}_s = 0 \tag{2.35}$$

where $\rho$ is density, in kg/m$^3$, $u$ and $v$ are the horizontal and vertical components of velocity, in m/s, $\Delta x$ and $\Delta y$ are, respectively, the horizontal and vertical dimensions of the volume, $e$, $w$, $n$, $s$ represent east, west, north, and south faces, respectively, of the control volume and $\dot{m}$ represents the mass flow rate of each face, in kg/s.

With the continuity equation in hand, the conservative differential form of

the equation will be obtained, and then its integration over the control volume will be carried out, according to the application of the finite volume method. For this, equation (2.35) will be divided by the volume area $\Delta x \Delta y$, obtaining:

$$\frac{\rho u\Big|_e - \rho u\Big|_w}{\Delta x} + \frac{\rho v\Big|_n - \rho v\Big|_s}{\Delta y} = 0 \tag{2.36}$$

According to the application of the limit in equation (2.36), the conservative differential form of the continuity equation is obtained:

$$\frac{\partial}{\partial x}(\rho u) + \frac{\partial}{\partial y}(\rho v) = 0 \tag{2.37}$$

This way, the integration of equation (2.37) on the control volume is performed and, then, equation (2.39) is applied to each control volume in a given time interval $\Delta t$:

$$\int_w^e \int_s^n \left[\frac{\partial}{\partial x}(\rho u) + \frac{\partial}{\partial y}(\rho v)\right] dxdy = 0 \tag{2.38}$$

$$\int_w^e \left(\rho u\Big|_e - \rho u\Big|_w\right) dy + \int_s^n \left(\rho v\Big|_n - \rho v\Big|_s\right) dx = 0 \tag{2.39}$$

It is important to emphasize that it does not help, from an engineering point of view, to have an excellent numerical model if the mathematical model (that is, the differential equations chosen) does not represent the phenomena to be simulated (Maliska, 2004).

In order to facilitate access to its high simulation capabilities, commercial CFD packages include sophisticated interfaces that allow the user to define parameters and analyze results. In this way, all codes contain three main elements: pre-processing, solution (or processing), and post-processing (Versteeg and Malalasekera, 2007).

Pre-processing consists of imposing the fluid flow problem on the CFD software. It is at this stage that: the region of interest, called computational domain, is defined; there is the generation of a mesh of elements (of cells or control volumes), where the subdivision of the domain takes place in a number of smaller subdomains that do not overlap; the physical and chemical phenomena to be modeled are selected; fluid properties are defined; and the proper boundary conditions are assigned to cells at the edges of the domain (Tucker, 2016).

In the processing step, the numerical method is applied to the computational domain. Therefore, the flow governing equations are integrated for all control volumes of the domain, the resulting equations are converted into a system of algebraic equations (discretization), which in turn are solved by an iterative method (Versteeg and Malalasekera, 2007).

Finally, in post-processing the results obtained can be visualized and analyzed.

For this, data visualization tools are widely implemented in CFD codes. Thus, you have means to visualize the domain geometry, control volume mesh, vector graphics, area graphics, 2D and 3D surface graphics, particle tracking, as well as animation of dynamic results (Tucker, 2016).

## 2.5 Constructal Design

Every flow system is subjected to configuration and shape, so it can be said that it has a design. The advantages of thinking of design as a science are extremely beneficial. Since natural flow systems have a configuration, the arrangement of these flows must be treated as a physical phenomenon, based on a scientific principle (Bejan and Lorente, 2008).

In this context, constructal theory is the mental viewing that the generation of flow structures that we often see in nature (river basins, lungs, atmospheric circulation, vascularized tissues, etc.) flow in time. This principle is the Construtal Law, proposed by Adrian Bejan in 1996 (Bejan, 1996, 1997, 2016):

> *for a finite-size flow system to persist in time (to live), its configuration must freely change in time such that it provides easier and easier access to its currents (fluid, energy, species, etc.).*

It is important to establish that, to apply the method, some parameters must be adopted. Physical constraints, degrees of freedom, and performance indicators are highlighted here. In most cases, these constraints are areas or volumes, whose values do not change throughout the application; degrees of freedom are properties that can be independently varied; and one (or more) performance indicators must be defined, which must be maximized or minimized (Dos Santos *et al.*, 2017).

The Constructal Design method is based on the Construtal Law, which aims to achieve the same objectives of flow configuration evolution. This way, since flow lines in a flow can be mapped and analyzed in order to obtain an optimization of the arrangement in the system, this method has been widely used in several scientific areas.

- Optimization of the evacuation of individuals in a building (Lui *et al.*, 2015);
- geometric optimization of a solar turbine duct, device for converting solar energy into electrical energy (Vieira *et al.*, 2017);
- forced convection of fluids in a finned channel (Feijó *et al.*, 2018);
- design of a gear that integrates cooling channels (Kamps *et al.*, 2018);
- geometric analysis of a device that converts wave energy into electrical energy of the overtopping type (Martins *et al.*, 2018);
- geometric optimization of a fin inserted in cavities (Razera *et al.*, 2018 and Bueno *et al.*, 2019);
- geometric evaluation of square bluff bodies arrays under forced convection (Teixeira *et al.*, 2018 and Pedroti *et al.*, 2020);

- cavity thermal problems (Vianna *et al.*, 2018 and Estrada *et al.*, 2020);
- performance analysis of flow channels in radiant cooling panels (Mosa, Labat, and Lorente, 2019a,b);
- analysis of entropy production (Ribeiro and Queiros-Condé, 2019);
- performance of boiler parts (Feng *et al.*, 2019 and Xie *et al.*, 2019);
- studies of a thermochemical energy storage reactor (Malley-Ernewein and Lorente, 2019);
- study of ocean thermal energy conversion systems (Wu *et al.*, 2019a,b);
- analysis of geometric parameters in an arterial bypass graft (Dutra *et al.*, 2020);
- buckling analysis of structural elements (Lima *et al.*, 2020);

### 2.5.1 Constructal Design Method Applied to OWC Devices

In addition to its wide application in several areas of engineering and even biology, the Constructal Design method has also been widely used in the study of devices which convert sea wave energy into electrical energy of the Oscillating Water Column (OWC) type. Gomes *et al.* (2013a,b) perform a geometric optimization of an OWC device, in real scale, using the Constructal Design method. In the first study, however, only one offshore device was considered, while in the second a comparison was made between onshore and offshore OWC devices. For this, in both studies, the ratios between height and length of the hydropneumatic chamber and the device turbine duct, and the submergence depth of the chamber, were used as degrees of freedom. As constraints to the method, the area of the hydropneumatic chamber and the total area were adopted. The results obtained by the authors in the first study led to a theoretical recommendation on the geometry of the chamber that maximizes the performance of the device, indicating that the greatest efficiency (around 40%) is obtained when the ratio between height and length of the chamber is 0.13 and chamber submersion is 9.50 m, showing the applicability and relevance of the Constructal Design method in designing OWC devices.

Lorenzini *et al.* (2015) used this methodology to analyze the geometry and submergence of an OWC device. This study aimed to achieve maximum electrical energy conversion, varying and analyzing the influence of three degrees of freedom: ratio between height and length of the OWC chamber, ratio between height and length of the turbine duct, and submergence of the device. A redistribution of the geometry and a variation in the value of its submersion depth improved the hydropneumatic power from 10.7 W to 190.8 W for degrees of freedom equal to 0.135, 6.0 and 9.5 m, respectively. These results led the authors to a theoretical recommendation on the geometry of an OWC device and its submersion depth, which maximized the performance of the device.

Gomes *et al.* (2017) make considerations about the choice of geometric constraints in a study that aimed to maximize energy conversion, using the same degrees

of freedom as in the previously mentioned studies of this device, but keeping them all constant. In this study, the authors sought to analyze the influence of the choice of geometric constraint values on the performance of an OWC device. For this, the volume of the hydropneumatic chamber and the total volume of the device were considered as geometric constraints; in addition, a parameter, named constraint variation, which reflects the relationship between the volume of the hydropneumatic chamber and the wavelength, was considered. The results presented show that when the constraint variation is equal to 1.75, the available hydropneumatic power is maximum.

Lima *et al.* (2017) presented a two-dimensional numerical study that sought to maximize the hydropneumatic power of two OWC devices, considering different combinations of height and length for the hydropneumatic chamber. Four constraints were adopted for the problem: input volumes of each device and total volumes of each device; as well as five degrees of freedom: ratio between height and length of the hydropneumatic chamber of each device, ratio between height and length of the turbine duct of each device and submersion depth of the devices. The results presented by the authors showed that, in the best case, the maximum total hydropneumatic power of 12729.98 W was obtained, and the case with the lowest performance presented a total hydropneumatic power of 1047.37 W.

Plamer *et al.* (2017) analyzed the influence of water mass flow and pressure gradient on the hydropneumatic power of an OWC device. For this, they used the Constructal Design method to evaluate the ratio between the inlet volume and the total volume of the hydropneumatic chamber, as well as the ratio between height and length of the hydropneumatic chamber. With the results, the authors verified how significant was the difference between the optimal geometry and the worst geometry, with the maximum hydropneumatic power being 18.48 times greater in relation to the lowest power. They could still notice that the device performance is better if, when using a regular wave, the chamber length is equal to the wavelength divided by 2.25 and the chamber height is equal to the wave height multiplied by 2.25.

Gomes *et al.* (2018) performed a geometric evaluation using the Constructal Design method to maximize the mean square hydrodynamic power of an OWC device subjected to multiple real-scale waves with different periods. For that, they used the volume of the hydropneumatic chamber and the total volume as constraints, and as degrees of freedom: ratio between height and length of the hydropneumatic chamber and submergence depth. The results obtained by these authors led to important theoretical recommendations on the design of OWC devices, such as the ratio of height to length of the hydropneumatic chamber, which led to the highest power achieved, was four times higher than the ratio of height to length of the incident wave.

Gomes *et al.* (2019) used the presented methodology to evaluate the geometry of a device subjected to the Pierson-Moskowitz wave spectrum. As in previous studies, the volume of the hydropneumatic chamber and the total volume of the device were considered as geometric constraints, and the ratio between height and length of the hydropneumatic chamber as degree of freedom. For the analyzed geometries, the

highest average power obtained was almost 18,000 W, while the lowest was less than 1,000 W.

Lima *et al.* (2019) present a two-dimensional numerical study with two coupled OWC devices. In this study, six constraints were adopted for the problem: inlet volumes of each device, total volumes of each device, and thickness of the side walls of each device; as well as four degrees of freedom: ratio between height and length of the hydropneumatic chamber of each device, height and thickness of the wall that divides the devices. Through the analysis of the results obtained, the authors identified that, with the horizontal variation of the wall that divides the devices, there was a considerable increase in hydropneumatic power, in which in the case of greater power, this thickness was equal to 2.22 m.

Letzow *et al.* (2020) performed a geometric evaluation of an onshore OWC device, aiming to maximize its available power. For this, the Constructal Design method was applied, in order to determine optimal dimensions of the ratio between height and length of the device chamber, ratio between height and length of the ramp and submersion of the frontal wall of the chamber. The authors found that the global optimal geometry led to a twice maximized available power 37.3% higher than the best case without the seabed ramp below the chamber and seven times better than the worst case. They also found that the chamber geometry over the available power was strongly affected by the ramp ratio.

Gomes *et al.* (2021) performed numerical simulations and geometrical analysis of an WEC device which has the OWC device as operating principle. They aimed to evaluate the geometric shape influence of the OWC chamber in the available hydropneumatic power. Therefore, the OWC device was subject to a JONSWAP wave spectrum and authors analyzed four geometric shapes: rectangle, trapezium, inverted trapezium, and double trapezium. To do so, Constructal Design was employed varying the degree of freedom $H_1/L$, problem constraints were the entrance area and the total area of the OWC chamber, which were kept constant. The authors have found results which indicated that when the rectangle geometrical shape was employed an improvement of nearly 99% was achieved.

Lima *et al.* (2021) presents a numerical study of a WEC device based on the OWC operating principle, with a variation on the number of coupled chambers. The authors aimed to evaluate the influence of the geometry and the number of coupled chambers to maximize the available hydropneumatic power. They have found that, among the cases examined, the device with five coupled chambers converted more energy than others, with a hydropneumatic power of 30.8 kW.

# 3 Materials and Methods

This chapter presents a description of the methodology used to obtain wave velocity data along a water column in the sea in Rio Grande, Brazil, of the hydrodynamic model used for the numerical simulation of the wave energy converter device of the Oscillating Water Column (OWC) type, of the steps necessary for the creation and optimization of the mesh used, and the geometric analysis performed on the device using the Constructal Design method.

## 3.1 WaveMIMO Methodology

Machado *et al.* (2021) proposed a methodology that converts sea state spectrum into series of surface elevation, applying this data as boundary conditions in a hydrodynamic model. To obtain a realistic sea state, which would allow an accurate analysis of wave parameters on the coast of the state of Rio Grande do Sul, Brazil, the Tomawac spectral model (Telemac-based Operational Model Addressing Wave Action Computation), belonging to the Open Telemac-Mascaret modelling suite, was used (Hervouet, 2007).

Tomawac is a scientific software which models the changes, both in the time and in the spatial domain, of the power spectrum of wind-driven waves and wave agitation for applications in the oceanic domain, in the intracontinental seas as well as in coastal zones (Awk, 2017). This is a third generation model, which implies that it does not require any parameterization in the directional or spectral distribution of energy. Tomawac models sea states by solving the balance equation of the wave action density directional spectrum, given by:

$$\frac{\partial N(f,\theta)}{\partial t} + \frac{\partial \dot{x} N}{\partial x} + \frac{\partial \dot{y} N}{\partial y} + \frac{\partial \dot{k}_x N}{\partial k_x} + \frac{\partial \dot{k}_y N}{\partial k_y} = Q(k_x, k_y, x, y, t) \tag{3.1}$$

where $N(f, \theta)$ represents the wave action density directional spectrum, $x$ and $y$ represent the axes of the Cartesian coordinate system, $k_x$ and $k_y$ are components of the wavenumber vector on the $x$ and $y$ axes, respectively, $Q$ represents the totality of source and sink terms, and $t$ is time. To solve this equation, the model uses the finite element method, in which, for each mesh node, the differential equation (equation (3.1)) is converted to a system of algebric equations and solved.

To obtain the sea state data used in this study, it was employed the WaveMIMO methodology, which corresponds to a series of steps performed to obtain velocity profile data corresponding to realistic irregular waves, which are then used in numerical simulations. A flowchart of all steps performed in this methodology is shown in figure 3.1.

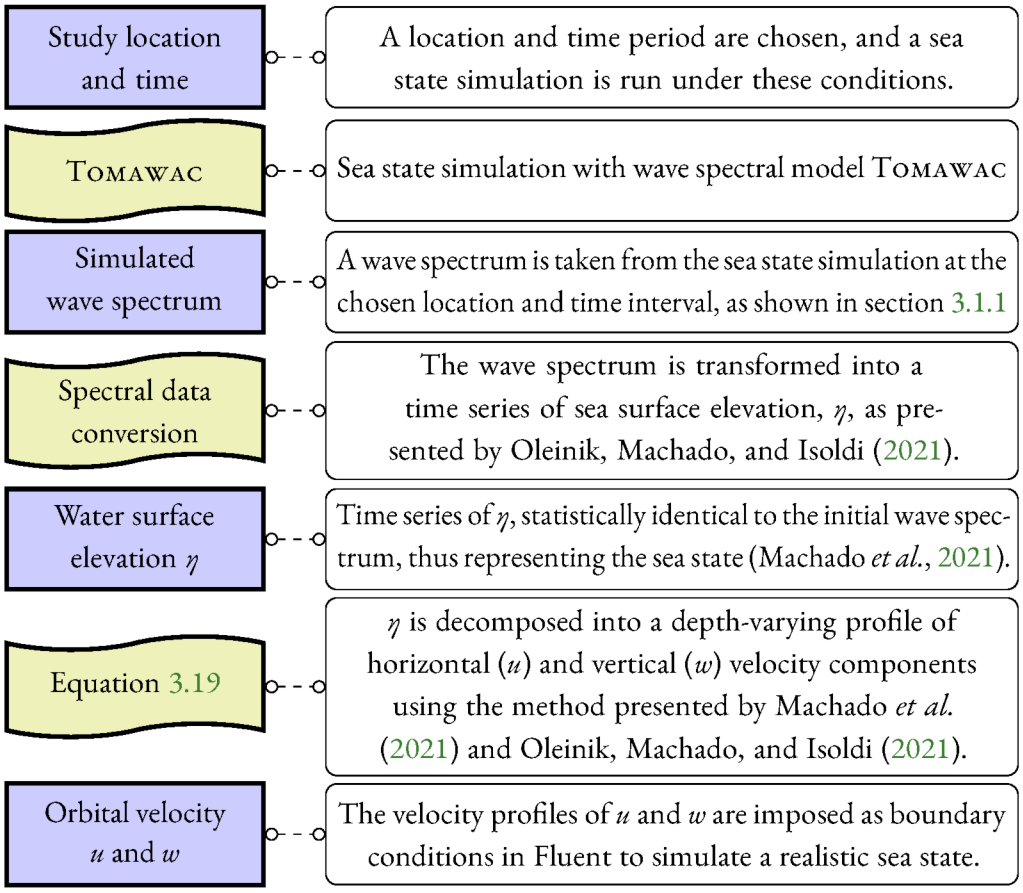


**Figure 3.1:** Summary flowchart of the WaveMIMO methodology. Shapes in lilac represent a step of the methodology and in yellow represent the action performed.

The first step in applying the methodology requires a sea state simulation, which was performed with Tomawac by Oleinik, Marques, and Kirinus (2017). The computational domain of the simulation was the continental shelf ranging from the south of Rio Grande do Sul, in the border between Brazil and Uruguay, to the north of the state of Santa Catarina, totaling approximately 735 km of coastline. The domain also extends 300 km towards the ocean (Oleinik, 2020).

In this simulation, three types of boundary conditions were used: surface, bottom, and oceanic. For the surface wind boundary condition, data from the Reanalysis 1[1] project, from the National Oceanic and Atmospheric Administration (NOAA), which have a temporal resolution of 6 h, a spatial resolution of 1.875° (T62 Gaussian Grid), and were bilinearly interpolated for all mesh nodes (Oleinik *et al.*, 2019).

For the bottom boundary condition, two types of bathymetric data were used, for the seabed on the continental shelf and for the deep ocean. The bathymetry of the continental shelf was obtained from nautical charts published by the Directorate of Hydrography and Navigation of the Brazilian Navy[2], and digitized by Cardoso

[1] www.psl.noaa.gov/data/gridded/data.ncep.reanalysis.html

[2] www.marinha.mil.br/chm/chm/dados-do-segnav-cartas-nauticas/cartas-nauticas

*et al.* (2014); and deep ocean bathymetry was obtained using the General Bathymetric Chart of the Oceans[3] (GEBCO) (Oleinik, 2020).

Ocean boundary condition was obtained from historical data from the Wave Watch III wave model, also from NOAA. The wave parameters obtained from these data were significant height ($H_s$), peak period ($T_p$), and main direction at peak period ($D_p$), with a temporal resolution of 3 h and a spatial resolution of 0.5° (Oleinik *et al.*, 2019).

Lastly, the simulation with Tomawac was performed for the period from January 1$^{st}$, to December 31$^{st}$, 2014. Calibration and validation of Tomawac for this region was performed by Oleinik, Marques, and Kirinus (2017) and Oleinik *et al.* (2019).

For this work, the point corresponding to node 1545 of the mesh of triangular elements was chosen for analysis (shown in figure 3.2), because it is a point located on Cassino beach, Rio Grande, in the state of Rio Grande do Sul, Brazil. This point is located at coordinates 52° 17′ 47.25″ W, 32° 22′ 30.95″ S, at a distance of 2 km from the coast and with a depth of 9.52 m.

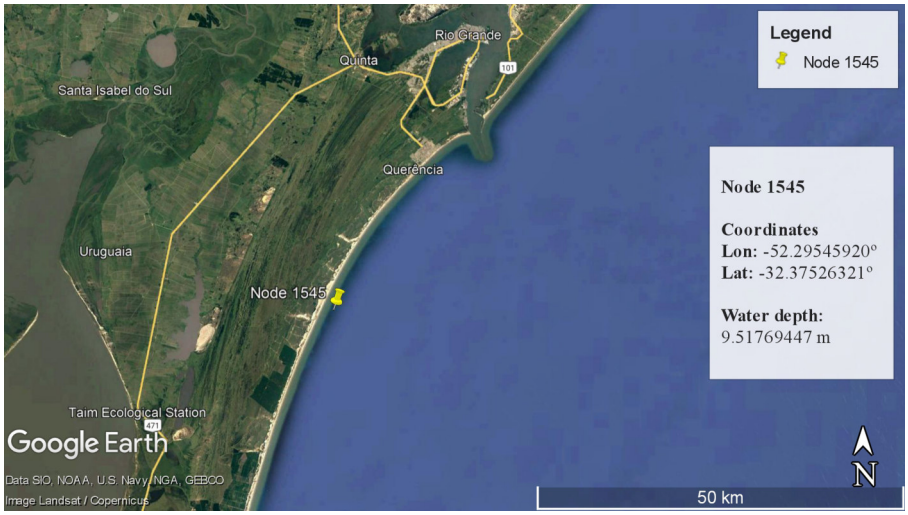


**Figure 3.2:** Location of the point in the Cassino beach chosen for analysis, which will provide realistic sea state data for the simulations.

### 3.1.1 Spectral Data Conversion and Temporal Location of the Study Area

Since the software Fluent, used for the numerical simulation of the OWC device, does not use spectral data as input, a transformation of these data is necessary. For this, wave spectra is transformed into a time series of free surface elevations, which is appropriately treated using the procedure presented by Machado *et al.* (2021) and Oleinik, Machado, and Isoldi (2021), and transformed into orbital velocity components of water particles. The time series of significant wave height and mean wave period for the year 2014 is shown in figure 3.3.

[3] www.gebco.net/

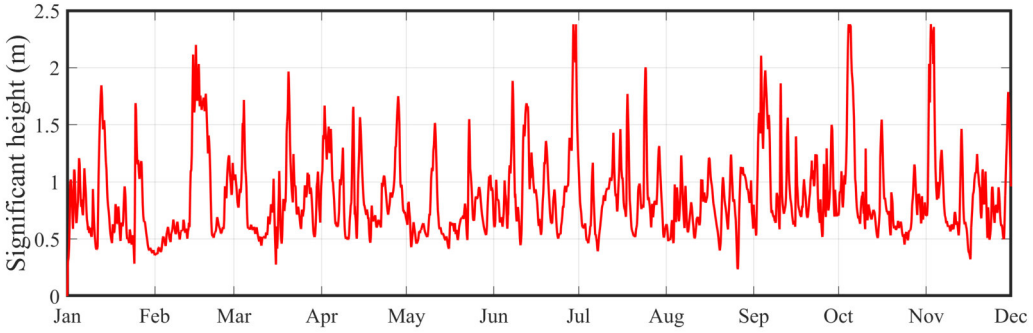


**(a)** Significant wave height ($H_s$).

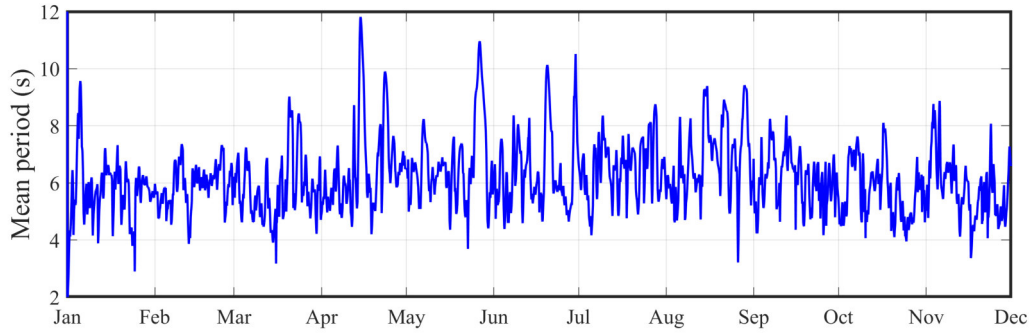


**(b)** Mean wave period ($T_m$).

**Figure 3.3:** Time series of significant wave height ($H_s$) and mean wave period ($T_m$) at the coast of Rio Grande, for the year 2014.

With the spectral data obtained from Tomawac, it was possible to obtain the wave parameters at the Cassino beach, for the year 2014. However, numerical simulations of an OWC device require a great computational effort, which implies the simulation of a short period of time, not compatible with the amount of data available for one year. Thus, it was necessary to carry out a statistical analysis to determine the wave parameters and interval of time representative of the year studied.

In this context, a bivariate histogram of the time series of significant wave height ($H_s$) and mean wave period ($T_m$) for the year 2014 was prepared, so that it was possible to define the highest frequency of values of these variables and thus guarantee a realistic representation of the sea state.

The histogram in figure 3.4 shows, for every pair of variables ($H_s$, $T_m$), the number of occurrences of that sea state in the year 2014, where it was possible to identify the recurrence of sea state characteristics throughout the analyzed period. It is possible to notice that the significant wave height that most manifested itself was 0.66 m and the wave period was 6.30 s, with an occurrence of over 2000 times, which represents 6% of the total for the year 2014.

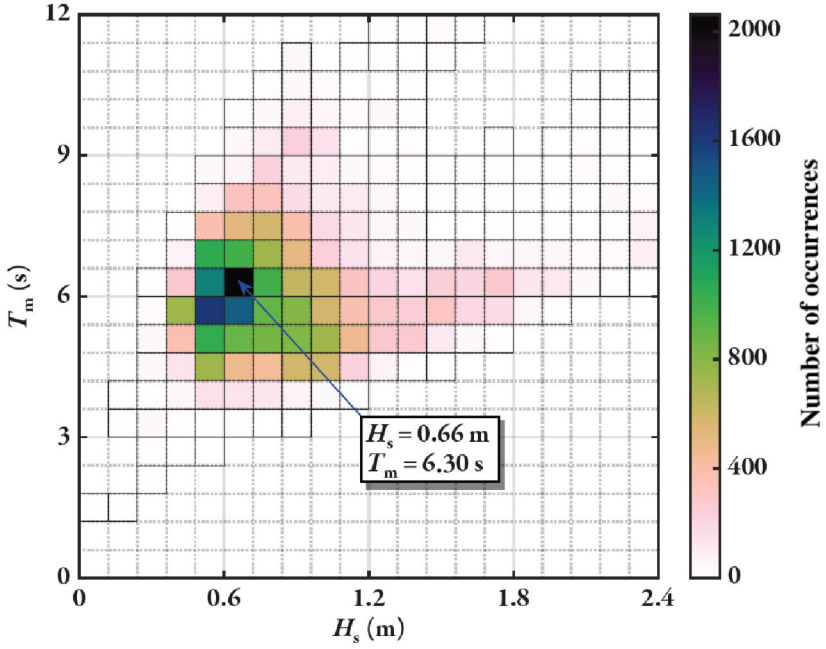


**Figure 3.4:** Bivariate histogram of the time series of significant wave height and mean wave period for the year 2014 (Oleinik, 2020).

Although the values for $H_s$ and $T_m$ which represent the wave climate for the coastal region of Rio Grande, in the state of Rio Grande do Sul, Brazil, were calculated, it was not yet known when they occurred in the year 2014.

It is important to highlight that each spectrum from Tomawac contains 15 min of data. Therefore, several variance spectra present in the year 2014 were analyzed by Oleinik (2020), in order to define which, if any, interval of time represented the wave climate for the year 2014. Then, the spectrum which came closest to $H_s \approx 0.66$ m and $T_m \approx 6.30$ s was chosen. This spectrum happened to be at the date August 23$^{rd}$, at 00:00 (figure 3.5).

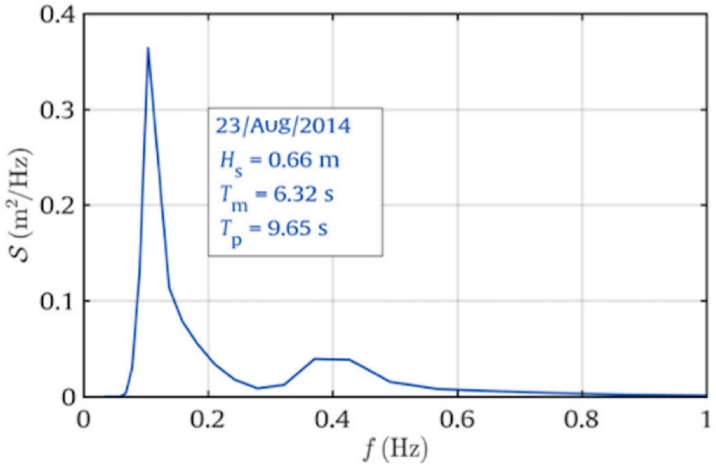


**Figure 3.5:** Variance spectrum of the sea state on August 23$^{rd}$, 2014, at 00:00 (Tavares *et al.*, 2020).

Therefore, this is the interval of time representative of the sea state at the city of Rio Grande, which was adopted to be used in the numerical simulations of the OWC device. As mentioned before, this time series of free surface elevation was appropriately treated using the procedure presented by Machado *et al.* (2021) and Oleinik, Machado, and Isoldi (2021), and transformed into orbital velocity components of water particles, which was, in turn, used as boundary conditions in the hydrodynamic model, thus completing specific objective I.

## 3.2 Multiphase Hydrodynamic Model

Then, we have the horizontal and vertical profiles of velocity data and the representative characteristics of the waves referring to the year 2014. Now, it is necessary to know how the OWC device behaves in this scenario. For this, it is necessary to simulate the sea states found, together with the device. To perform this simulation, Ansys Fluent software was used, which is a computational fluid dynamics (CFD) commercial code based on the finite volume method (FVM).

This software is marketed by Ansys, Inc. and provides comprehensive modeling capabilities for incompressible and compressible, laminar and turbulent fluid flow problems. Steady-state or transient flow analysis can be performed. In Ansys Fluent, a wide range of mathematical models for transport phenomena (such as heat transfer and chemical reactions) are combined with the ability to model complex geometries. Examples of fluid applications include laminar non-Newtonian fluids in process equipment; conjugate heat transfer in turbomachinery and automotive engine components; pulverized coal combustion in utility boilers; external aerodynamics; flow through compressors, pumps, and fans; and multiphase flows in bubble columns and fluidized beds (ANSYS Inc., 2013).

In this study, to tackle with water-air interaction, a nonlinear multiphase model was employed. The motion of fluid flow throughout the mixture is described by the continuity equation and the momentum conservation equations, given by (Versteeg and Malalasekera, 2007 and Srinivasan, Salazar, and Saito, 2011):

$$\frac{\partial \rho}{\partial t} + \nabla \cdot \rho \vec{v} = 0 \tag{3.2}$$

$$\frac{\partial (\rho \vec{v})}{\partial t} + (\nabla \cdot \rho \vec{v}) \vec{v} = -\nabla p + \mu \nabla^2 \cdot (\vec{v}) + S \tag{3.3}$$

where $\nabla \cdot \rho \vec{v}$ represents the divergence of the vector field $\rho \vec{v}$, $p$ is static pressure, $\nabla p$ represents the divergence of the vector field $p$, $\mu$ is the absolute viscosity coefficient, and $S$ is the source.

For a two-dimensional domain, the continuity equation and the momentum conservation equations are as follows (Schlichting and Gersten, 2000 and Meier and

Sreenivasan, 2004):

$$\frac{\partial u}{\partial x} + \frac{\partial w}{\partial z} = 0 \tag{3.4}$$

$$\rho\frac{\partial u}{\partial t} + \rho\left(u\frac{\partial u}{\partial x} + w\frac{\partial u}{\partial z}\right) = -\frac{\partial p}{\partial x} + \mu\left(\frac{\partial^2 u}{\partial x^2} + \frac{\partial^2 u}{\partial z^2}\right) + S \tag{3.5}$$

$$\rho\frac{\partial w}{\partial t} + \rho\left(u\frac{\partial w}{\partial x} + w\frac{\partial w}{\partial z}\right) = -\frac{\partial p}{\partial z} + \mu\left(\frac{\partial^2 w}{\partial x^2} + \frac{\partial^2 w}{\partial z^2}\right) + \rho g + S \tag{3.6}$$

where $u$ and $w$ are the velocity components in $x$ and $z$ direction (m/s), respectively, $\rho$ is density (kg/m$^3$), $t$ is time (s), $p$ is static pressure (N/m$^2$), $\mu$ is the absolute viscosity coefficient (kg/m.s), and $\rho g$ is the gravitational body force (N/m$^3$).

The nonlinear multiphase model adopted uses the surface-tracking volume of fluid (VOF) technique (Hirt and Nichols, 1981), which can model two or more immiscible fluids and track the volume fraction ($\alpha$) of these fluids inside each element throughout the domain. Thus, according to volume fraction values for a domain composed of water and air, three situations are possible: if $\alpha$ is equal to 0, that means the cell is empty of water, filled exclusively by air; if $\alpha$ is equal to 1, that means the cell is full of water; and if $\alpha$ is equal to any other value between 0 and 1, that means the cell contains the interface between the two phases. The volume fraction for the two phases throughout the two-dimensional domain follows a transport equation as shown (Gopala and van Wachem, 2008 and Srinivasan, Salazar, and Saito, 2011):

$$\frac{\partial \alpha}{\partial t} + \frac{\partial \alpha u}{\partial x} + \frac{\partial \alpha w}{\partial z} = 0 \tag{3.7}$$

The values for density and absolute viscosity coefficient, fluid properties present in the momentum conservation equations (equations (3.5) and (3.6)), are then determined as follows (Srinivasan, Salazar, and Saito, 2011):

$$\rho = \alpha\rho_{water} + (1-\alpha)\rho_{air} \tag{3.8}$$

$$\mu = \alpha\mu_{water} + (1-\alpha)\mu_{air} \tag{3.9}$$

As wave reflection may interfere with surface elevation along the channel, a numerical beach was inserted at the end of the domain. In this case, a damping sink term ($S$) is added to the momentum equation for the cell zone in the vicinity of the pressure outlet boundary (ANSYS Inc., 2013):

$$S = -\left[C_1\rho V + \frac{1}{2}C_2\rho|V|V\right]\left(1 - \frac{z - z_{fs}}{z_b - z_{fs}}\right)\left(\frac{x - x_s}{x_e - x_s}\right)^2 \tag{3.10}$$

where $C_1$ and $C_2$ are linear (1/s) and quadratic (1/m) damping coefficients, respectively, $V$ is the velocity along vertical direction (m/s), $z$ is the distance from free surface level (m), $z_{fs}$ and $z_b$ are the free surface and bottom coordinates along vertical direction (m),

respectively, $x$ is the horizontal coordinate (m), $x_s$ and $x_e$ are the start and end points of the numerical beach in the horizontal direction (m).

As previously mentioned, the methodology used in this study consists of generating numerical waves through the imposition of discrete transient data of orbital wave velocity in vertical and horizontal directions. To perform the verification and validation of the hydrodynamic model, regular waves were generated as to simulate those performed in the experiment in which the validation was based. To obtain the values used in the imposition of prescribed velocity boundary conditions, and to perform an analytical comparison with the results, the $2^{nd}$ order Stokes wave equation was employed. Therefore, the horizontal and vertical wave velocity components, and the water surface displacement ($\eta$) are, respectively, as presented by Dean and Dalrymple (1991):

$$u = \frac{H}{2}\frac{gk}{\omega}\frac{cosh\ k(h+z)}{cosh(kh)}cos(kx-\omega t) + \frac{3H^2\omega k}{16}\frac{cosh\,[2k(h+z)]}{sin^4(kh)}\ cos\ 2(kx-\omega t) \tag{3.11}$$

$$w = \frac{H}{2}\frac{gk}{\omega}\frac{sinh\ k(h+z)}{cosh(kh)}sin(kx-\omega t) + \frac{3H^2\omega k}{16}\frac{sinh\,[2k(h+z)]}{sin^4(kh)}\ sin\ 2(kx-\omega t) \tag{3.12}$$

$$\eta = \frac{H}{2}cos(kx-\omega t) + \frac{H^2k}{16}\frac{cosh\,(kh)}{sinh^3(kh)}\,[2+cosh\,(2kh)]\ cos\ 2(kx-\omega t) \tag{3.13}$$

where $H$ represents the wave height (m), $k$ is the wave number ($m^{-1}$), $h$ is the channel water depth (m), and $\omega$ is the wave angular frequency (rad/s).

Lastly, when analyzing different geometries for the OWC device, the hydropneumatic power ($P_{hyd}$) was calculated, which was done using the equation (Dizadji and Sajadian, 2011):

$$P_{hyd} = \left(p_{air} + \frac{\rho_{air}v_{air}^2}{2}\right)\frac{\dot{m}}{\rho_{air}} \tag{3.14}$$

where $p_{air}$ is the air static pressure at the chamber duct ($N/m^2$), $\dot{m}$ is the air mass flow rate inside the turbine duct (kg/s), and $v_{air}$ is the outflow air velocity (m/s), which, in turn, is obtained as:

$$v_{air} = \frac{\dot{m}}{A_{duct}\,\rho_{air}} \tag{3.15}$$

where $A_{duct}$ is the two-dimensional area of the turbine duct ($m^2$).

### 3.2.1 Statistical Measures

As previously mentioned, the instantaneous available hydropneumatic power for each OWC geometry configuration will be calculated. Then, to calculate mean available power values, the Root Mean Square (RMS), indicated for transient flow problems, will be employed. As shown by Marjani *et al.* (2006) and Holthuijsen (2010),

for any flow characteristic designed by $x_i(t)$ varying with time, the corresponding RMS value $X$ over a the number of observations $n$ is calculated by the following relation:

$$X_{RMS} = \sqrt{\frac{1}{n}\sum_{i=1}^{n} x_i^2} \tag{3.16}$$

To assist in comparing simulation results, both the Root Mean Squared Error (RMSE) and the Normalized Root Mean Squared Error (NRMSE) were employed. According to Neill and Hashemi (2018) and Misra and He (2020), RMSE and NRMSE are given, respectively, by:

$$RMSE = \sqrt{\frac{1}{n}\sum_{i=1}^{n}(S_i - O_i)^2} \tag{3.17}$$

$$NRMSE = \frac{\sqrt{\frac{1}{n}\sum_{i=1}^{n}(S_i - O_i)^2}}{O_{max} - O_{min}} \tag{3.18}$$

where $S_i$ represents the values obtained from simulations, $O_i$ represents the observation, i.e. the analytical solution or experimental results, $n$ is the number of observations available for analysis, and $O_{max}$ and $O_{min}$ indicate the maximum and minimum observation values, respectively.

It should be mentioned here that NRMSE has been widely used for dealing with regular waves, since minimum and maximum free surface elevation values are similar to troughs and crests throughout simulations. Similar works dealing with regular waves made use of this statistical indicator (Simonetti *et al.*, 2018; Shalby *et al.*, 2019; Xu and Huang, 2019 and López *et al.*, 2020). Since the validation procedure make use of regular waves, NRMSE was adopted to account for the error in the validation simulations. However, it is not suited for analyzing irregular waves, once minimum and maximum may vary greatly from values which actually represent a fluid flow. Therefore, as it was similarly done by Çelik and Altunkaynak (2020), Singh, Abdussamie, and Hore (2020), and Ezhilsabareesh *et al.* (2021), RMSE was adopted for the study case simulations.

## 3.3 Verification and Validation of the Hydrodynamic Model

Before simulating the OWC device subjected to a realistic sea state, the hydrodynamic model must be validated. For this, a laboratory experiment performed by Zabihi, Mazaheri, and Namin (2019) was numerically simulated using Ansys Fluent. This procedure was performed by Maciel *et al.* (2021), where two sets of simulations were carried out. The first one aimed to conduct a verification of regular waves generation and propagation, simulating $2^{nd}$ order Stokes waves and then comparing the results with its analytical solution (equation 3.13). In the second set, the hydrodynamic

model was validated; an OWC device was inserted in the wave channel to reproduce a laboratory experiment performed by Zabihi, Mazaheri, and Namin (2019). The wave parameters adopted were the same for both simulations, where the height of the simulated wave is 0.15 m and its period is 2.2 s, following the values used in the experiment.

In both sets of simulations, a two-dimensional numerical wave channel (NWC) is part of the computational domain, with a length of 65 m, which corresponds to approximately 9 times the wavelength ($L$ = 7.54 m), height of 6 m, and water depth ($h$) of 4 m. As adopted by Lisboa, Teixeira, and Didier (2017), two wavelengths on the extremity of the NWC have been dedicated to be a numerical beach, thus responsible for wave damping and to avoid wave reflection.

In the verification step, where only the numerical wave channel was simulated, the following boundary conditions have been assigned to the computational domain, as shown in figure 3.6: on the left, in blue, the prescribed velocity boundary condition was assigned; at the bottom, in purple, the no-slip wall boundary condition was imposed; on the left and at the top, in red, the pressure outlet boundary condition was used with an atmospheric pressure value of 101325 Pa; lastly, on the right, a special pressure outlet boundary condition was assigned, using a hydrostatic pressure profile, as adopted by Lisboa, Teixeira, and Didier (2017). Additionally, the surface water line (SWL) is represented by a dashed gray line.

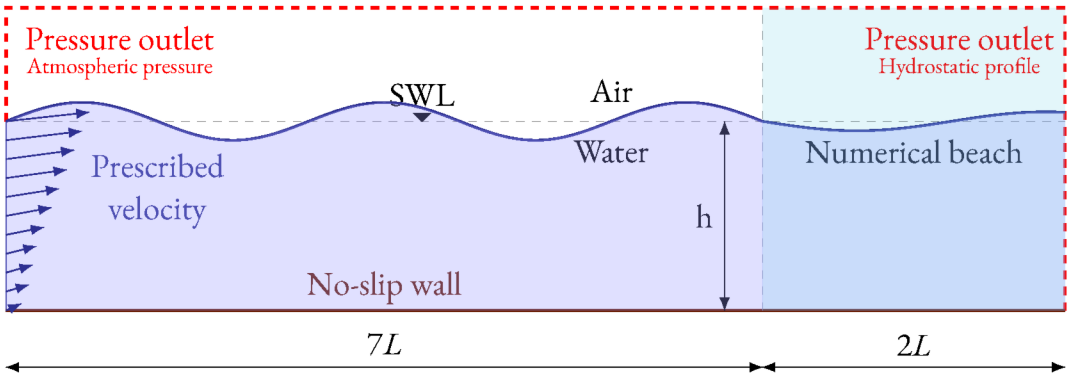


**Figure 3.6:** Computational domain used in this study for the hydrodynamic model verification.

As shown in figure 3.6, the prescribed velocity boundary condition is assigned to the entrance of the channel, on the left boundary. In this region, a vertical profile of wave orbital velocity $\vec{v} = (u,\ w)$ is used, which, depending on velocity values, can reproduce both regular waves and realistic sea states into the wave channel. These velocity profiles, variables in time and along depth, may present values obtained from equations (2.23) and (2.24), which generates regular waves; or they may present values derived from the free surface elevation obtained from the sea state spectrum (from Tomawac), which is transformed into orbital velocity components using the

methodology presented by Machado *et al.* (2021) and Oleinik, Machado, and Isoldi (2021), thus generating realistic waves.

However, the methodology used to impose wave velocity data as boundary conditions presents a geometric particularity, which is, it requires that this region of geometry be divided into subregions (green and red lines), as shown in figure 3.7 (Machado *et al.*, 2017).

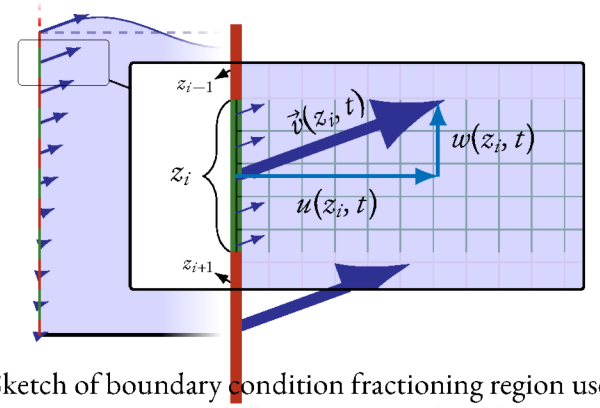


**Figure 3.7:** Sketch of boundary condition fractioning region used in the wave generation with the adopted methodology.

These velocity profiles are vertically discretized into segments with depth $z_i$, and each line segment uses a velocity value calculated, usually, at the center of that segment, as illustrated in figure 3.7. The velocity profiles are also transient, with temporal discretization equal to the simulation time step. Fluent then applies horizontal and vertical wave velocity components $u(z_i, t)$ and $w(z_i, t)$, respectively, obtained for that segment, as indicated by the vectors in the detail of figure 3.7, thus simulating the irregular sea state obtained from the spectrum (Oleinik, 2020).

However, the optimal discretization, i.e. the number of line segments, that provides a proper wave generation must be analyzed. Therefore, the number of segments were evaluated over 2 min of simulation, comparing free surface elevation when using 5, 8, 10, and 16 line segments at the velocity inlet region.

Since the mean water level in the wave channel is 4 m, the length of each segment changes according to the total amount of segments. For example, when using 5 line segments at the entrance, each segment has a length of 0.80 m; when using 8 segments at the entrance, each one has a length of 0.50 m, and so on. The computational domain geometry and mesh were generated using GMSH software, developed by Geuzaine and Remacle (2009).

As presented in section 3.2, the numerical beach equation has a linear ($C_1$) and a quadratic ($C_2$) damping coefficient, which allows for the calibration of the numerical beach. Similar calibrations were previously carried out, where good results were achieved with $C_2 = 0$ (Perić and Abdel-Maksoud, 2016 and Lisboa, Teixeira, and Didier, 2017). Therefore, simultaneously to the velocity inlet boundary condition testing, 5 values of $C_1$ were tested, as shown in figure 3.8, over simulations of 2 min to analyze the efficiency of these parameters.

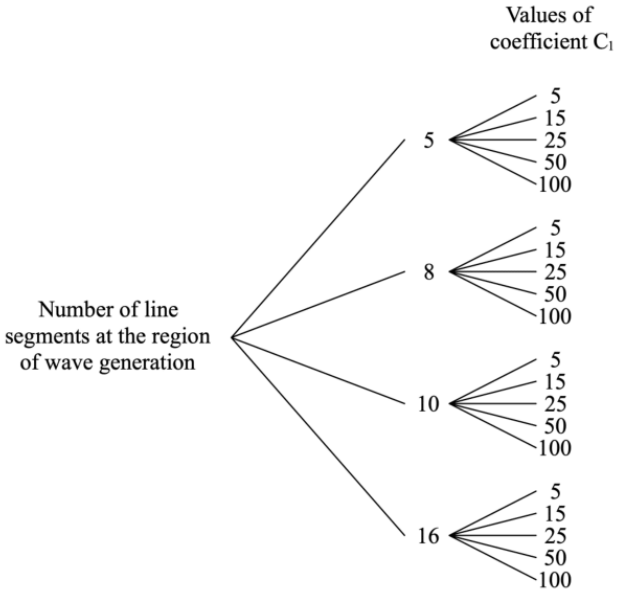


**Figure 3.8:** Number of line segments at the region of wave generation and values of coefficient $C_1$ used in the verification study.

Once the numerical beach was calibrated, mesh discretization was studied. For that, four different mesh sets were analyzed. In each set, different mesh volume sizes were tested, assuming the values shown in table 3.1, where $L$ is the wavelength and $H$ is the wave height. In addition, a refinement zone, with a height twice the value of the incoming wave height, was applied to the area nearing the free surface, through the entire length of the channel, based on the stretched mesh technique (Mavriplis, 1995). Outside the refinement zone, along the channel, elements had a square shape with equal length and height, as it can be seen in figure 3.9.

**Table 3.1:** Mesh element sizes used in the mesh independence study.

| | **Length and height of mesh volumes along the channel** | **Height of mesh volumes inside refinement zone** |
|---|---|---|
| **Mesh 1** | $L/10$ | $H/10$ |
| **Mesh 2** | $L/20$ | $H/15$ |
| **Mesh 3** | $L/30$ | $H/20$ |
| **Mesh 4** | $L/40$ | $H/25$ |

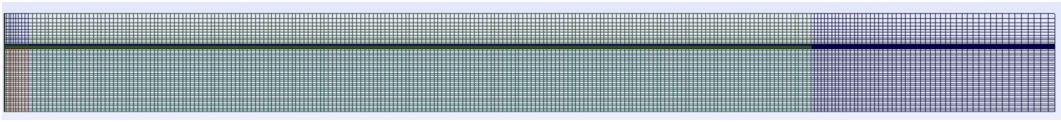

**Figure 3.9:** Two-dimensional mesh used for wave generation verification.

To ensure a proper wave generation, temporal discretization was also studied and time step ($\Delta t$) tests were performed. Liu, Hyun, and Hong (2011) indicates that numerical accuracy is ensured when $\Delta t$ is less than $T/50$, where $T$ is the wave period. Therefore, $\Delta t$ values of $T/50$, $T/100$, $T/200$, $T/400$, and $T/800$ were tested. It is worth highlighting that, before this test was performed, the time step adopted for the simulations was $T/400$, as used in Zabihi, Mazaheri, and Namin (2019).

With all parameters tested, regular $2^{nd}$ order Stokes waves were simulated in the channel and its results were compared with the analytical solution, given by equation (3.13). After all tests which ensure a proper wave generation, an OWC WEC device with the dimensions as those used in Zabihi, Mazaheri, and Namin (2019) was inserted in the channel.

In the mentioned experiment, a fixed OWC model of 1:15 scale was used, with a length of 0.80 m, width of 0.92 m, and 1.11 m of height (figure 3.10). The experiments were performed in a wave tank of 400 m length, 6 m width, and 4 m height. Regular waves with a wave height of 0.15 m and three wave periods of 1.8, 2.0, and 2.2 s were used. It is worth mentioning that Zabihi, Mazaheri, and Namin (2019) observed that short period waves entering the device could reflect from the chamber rear wall, interacting with incoming waves and resulting in higher nonlinearity; thus, the 2.2 s wave period was adopted for the validation numerical simulations.

It should be noted that, for the validation computational domain, a simplification regarding the experiments was made. In the laboratory, the distance between the OWC model and each side wall of the tank was 2.54 m; since this value is more than twice the width of the OWC model, wave reflection was considered negligible. Therefore, a two-dimensional computational domain was adopted here for the validation. Figure 3.10 shows the dimensions of the physical model, as well as its cross-section, used in the two-dimensional computational domain, and figure 3.11 shows the computational domain used in the validation procedure.

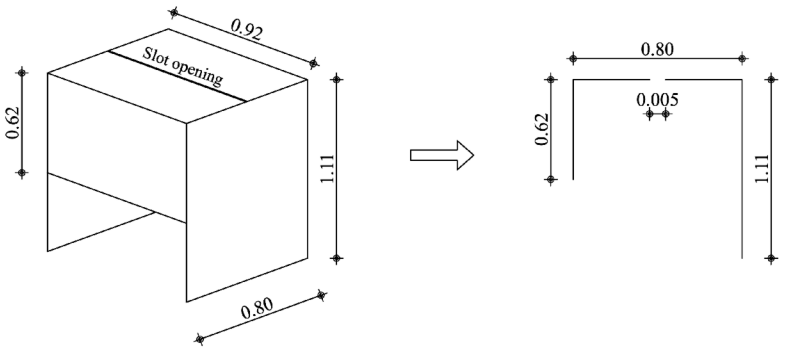


**Figure 3.10:** Dimensions of the physical model used in the experiments of Zabihi, Mazaheri, and Namin (2019) and of its cross-section (in m).

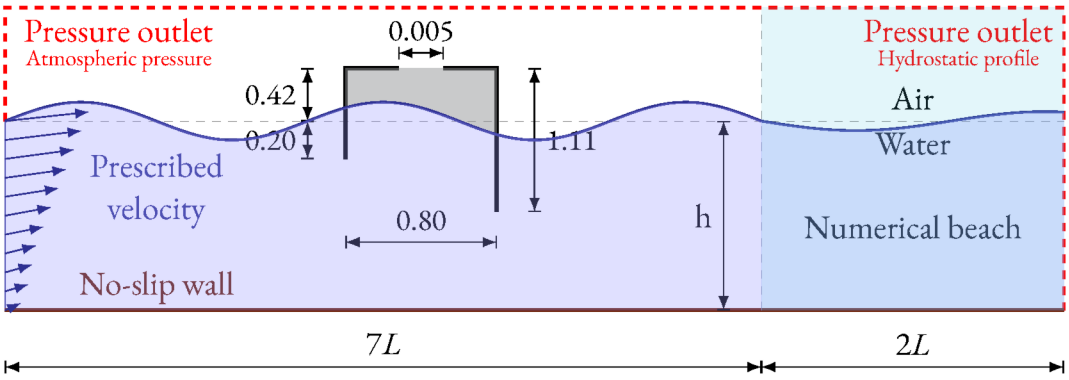


**Figure 3.11:** Computational domain used for validation of hydrodynamic model.

Besides the spatial discretization tested for the wave channel, a refinement zone of two wavelengths, one wavelength to each side of the OWC, was applied to the area around the device. Inside the refinement zone, mesh elements had a horizontal and vertical size of 0.01 m, except for the slot opening region, where the horizontal size of elements were 0.0025 m, following the recommendation from Zabihi, Mazaheri, and Namin (2019). The mesh used for the validation simulation can be seen in figure 3.12.

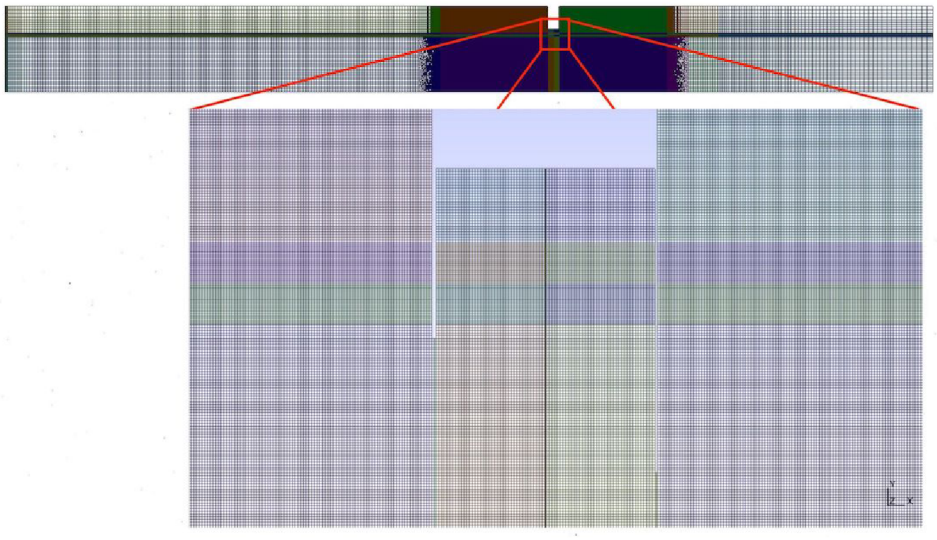

**Figure 3.12:** Discretization of the computational domain employed in the methodology validation.

To measure water free surface elevation and air pressure, 4 numerical wave gauges (WG) and a pressure sensor (PS) were used, as reported by Zabihi, Mazaheri, and Namin (2019). From these, 2 wave gauges were positioned previously to the front wall of the device and the others were positioned inside the device chamber. The front wall of the OWC device was positioned 38 m from the beginning of the wave tank, as it was done in the laboratory experiment. Figure 3.13 indicates the location of the sensor and gauges positioned in the chamber and along the wave tank.

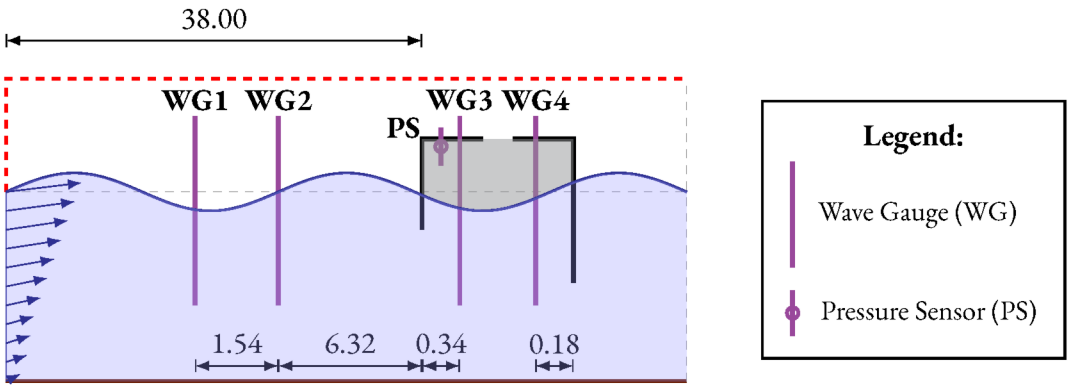


**Figure 3.13:** Location of wave gauges and pressure sensors based on the experiments of Zabihi, Mazaheri, and Namin (2019) (in m).

In addition to spatial and temporal discretization, other numerical parameters were also defined and adopted for the verification and validation. A pressure-based solver was used for the numerical simulation. To solve the problem of linear dependence of velocity on pressure, the velocity-pressure coupling scheme pressure-implicit with splitting of operators (PISO) was adopted. A first order upwind scheme was applied for the discretization of spatial derivatives in the momentum equations, and a first order implicit formulation was adopted for time discretization. For the volume fraction, the geo-reconstruct method was applied; and for pressure interpolation at volume faces, the pressure staggering option (PRESTO!) scheme was used. In the verification simulations, only laminar flow was considered, and for the validation case two turbulence models were also considered: $k$-$\varepsilon$ and $k$-$\omega$ shear stress transport (SST), as to reproduce the same numerical results as Zabihi, Mazaheri, and Namin (2019).

## 3.4 Numerical Simulation with Realistic Sea Data

Once the hydrodynamic model is validated, it can be used to numerically simulate an OWC device subjected to realistic sea waves. Again, two sets of simulations were performed. The first one aimed to perform another verification of the wave generation and propagation, since the waves generated in this stage are different from those in the validation procedure. In this case, velocity profile data were imposed as boundary conditions and then the results were compared with the realistic irregular waves obtained from Tomawac. In the second set of simulations, the OWC device was inserted and simulated as study case, with different geometries, according to the Constructal Design method.

In all simulations, a wave channel is part of the computational domain. To determine the length of the wave channel, the characteristic wavelength of the 15 min of realistic sea data used in the numerical simulations was calculated. Machado *et al.* (2021) used the zero-up crossing method to count and measure waves (Dean and Dalrymple, 1991), obtaining their periods and, subsequently, their wavelengths,

by solving for $k$ in the dispersion relation, given by (Holthuijsen, 2010):

$$\omega^2 = g\,k\,tanh(k\,h) \tag{3.19}$$

Thus, the computational domain consisted of a wave channel with a length five times the characteristic wavelength of the 15 min of realistic sea data ($L$ = 51.6 m), as adopted by Gomes *et al.* (2018), totaling 258 m; a height of 12 m; and a water depth ($h$) of 9.52 m, which is the water depth of the point located on Cassino beach (see figure 3.2) corresponding to node 1545 of the mesh used in the spectral model simulation (Oleinik, Marques, and Kirinus, 2017; Oleinik *et al.*, 2019 and Machado *et al.*, 2021).

As for the numerical beach, Machado *et al.* (2021) applied the WaveMIMO methodology and compared two lengths for the this region of the domain: two wavelengths and two and a half wavelengths. They obtained better results the latter length, therefore two and a half wavelengths on the extremity of the wave channel have been dedicated to act as a numerical beach, thus responsible for wave damping and to avoid wave reflection. As for the calibration of the numerical beach, the same values for the linear ($C_1$) and quadratic ($C_2$) damping coefficient adopted in the validation procedure were used here. Again, in the verification step, only the numerical wave channel was simulated and the same boundary conditions adopted in the validation procedure (see section 3.3) have been assigned to the computational domain, as shown in figure 3.14.

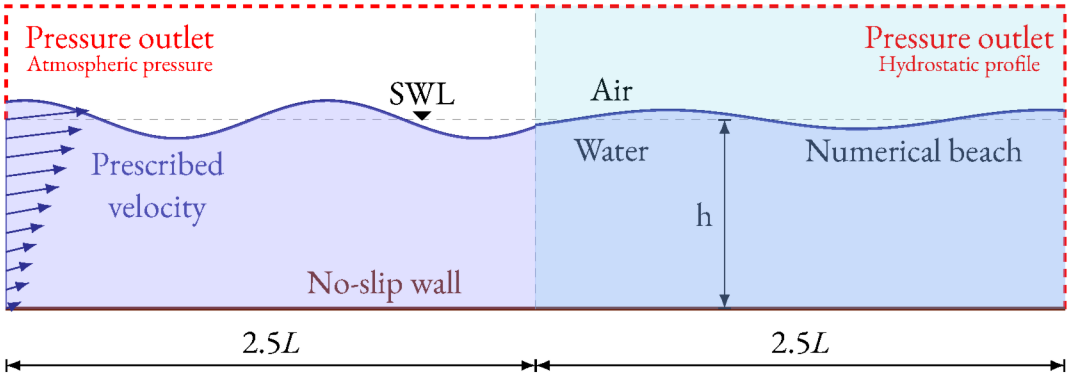


**Figure 3.14:** Computational domain used in this study for the numerical simulations with realistic sea data.

### 3.4.1 Simulation Discretization and Parameters

As mentioned before, in the WaveMIMO methodology, the prescribed velocity boundary condition is assigned to the line segments at the entrance of the channel, which requires a discretization of the number of line segments that provide a proper wave generation. Therefore, to evaluate the numerical behavior regarding the number of line segments (or velocity profile divisions), simulations of 5 min were performed,

comparing free surface elevation when using four different number of line segments. For the validation simulations, the optimal number was 8 line segments, however, Machado *et al.* (2021) achieved better results with 14 line segments. Therefore, in addition to these two values, 10 and 12 line segments were also compared.

Another important factor to be analyzed is that, during the spectral data conversion, the orbital wave velocity is measured at the center of each line segment (see figure 3.7) and then converted to wave velocity components $u$ and $w$. However, it is not known if this location, at the center of each line segment, provides a proper wave generation, or if another location (top or bottom of each line segment) yields better results. Therefore, in addition to the number of line segments, the location from where, alongside each line segment, the wave velocity components are calculated is tested, also with simulations of 5 min. It is important to highlight that, up to this point, wave velocity data has been calculated at the middle of each line segment. It should also be mentioned that, as of this day, this test has not yet been performed for studies which employ this methodology of assigning transient velocity data to line segments at the entrance of a wave channel as boundary conditions.

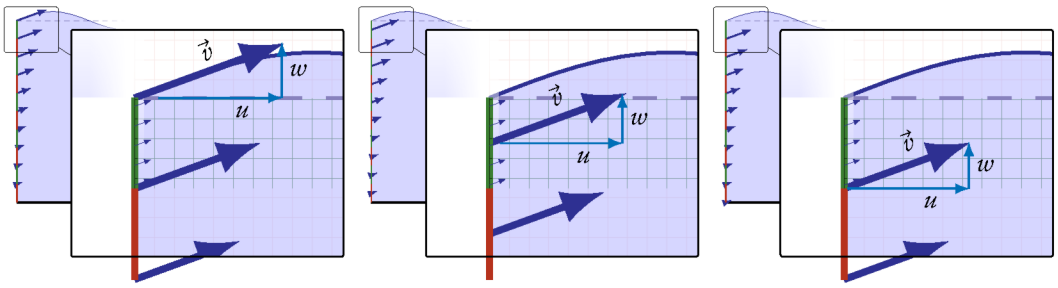


**(a)** Velocity at the top of the line segment.

**(b)** Velocity at the middle of the line segment.

**(c)** Velocity at the bottom of the line segment.

**Figure 3.15:** Location alongside each line segment from where horizontal and vertical components of orbital wave velocity are calculated.

Regarding the spatial discretization of the domain, mesh volume sizes similar to those adopted by Machado *et al.* (2021) were adopted here, i.e., the domain was vertically discretized into 60 volumes in the region with only water, 20 volumes per wave height in the free surface region and 30 volumes in the region with only air, and horizontally, the discretization was 50 volumes per wavelength. In this case, for the wave height value in the free surface region, the greatest free surface elevation during the 15 min of realistic sea data was considered, $H = 0.67$ m; and, as previously mentioned, the typical wavelength for those 15 min is $L = 51.6$ m. As for the temporal discretization, it was adopted the same as the one applied by Machado *et al.* (2021), a time step $\Delta t = 0.05$ s.

As it was done in the previous simulations, other numerical parameters were also defined and adopted here, such as the PISO velocity-pressure coupling scheme, first order upwind scheme for the discretization of spatial derivatives in the momentum

equations, first order implicit formulation for the time discretization, and PRESTO! scheme. However, in all simulations, laminar flow was considered.

### 3.4.2 Inserting the OWC device in the wave channel

With all parameters tested, irregular waves, representative of the sea state, were simulated in the channel and its results were compared with the time series obtained from Tomawac. After all tests which ensure a proper wave generation, the OWC WEC device was inserted in the channel.

The OWC device used in this study was based on the device installed on the island of Pico, in the Azores archipelago, Portugal (see figure 2.13b). The report of the Non Nuclear Energy Programme Joule III (1998) presents a cross-section technical drawing of the OWC device at Pico island. The device was built in-situ on rocky bottom, spanning a small natural harbour (Falcão, 2000). The inner sectional area of the hydropneumatic chamber is 12 m × 12 m at the bottom of the chamber, the turbine axis is located 10 m from the mean water level, the turbine duct has a diameter of 2.8 m and a length of 11.3 m, and the draught of the front wall is 3.4 m from the mean water level, as shown in figure 3.16.

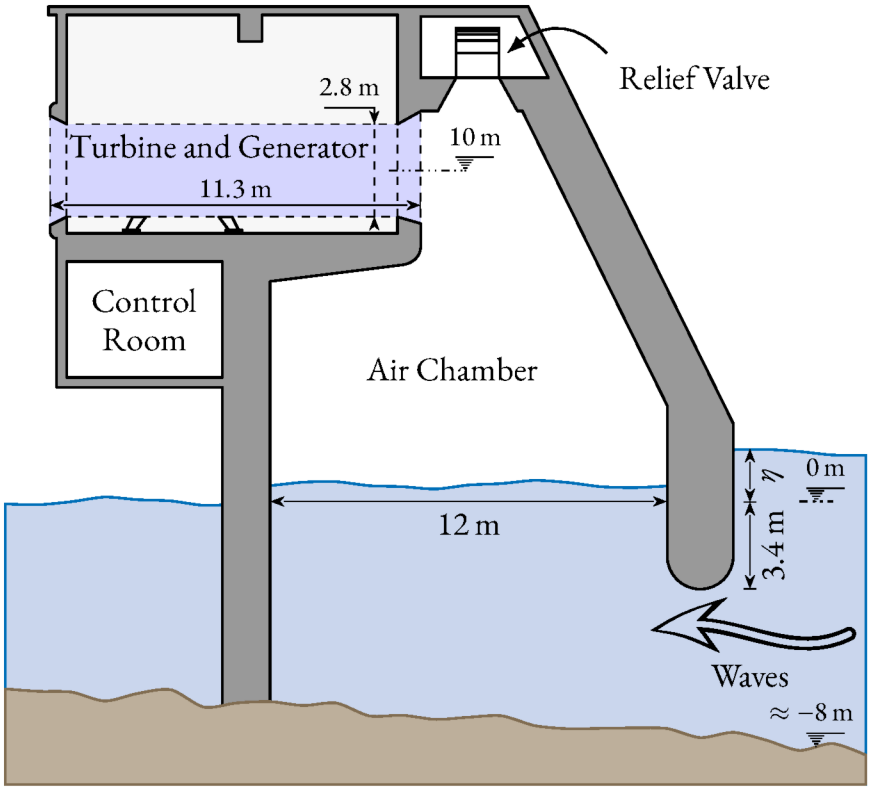


**Figure 3.16:** Representation of the cross-section of the OWC device located in Pico island. Adapted from Joule III (1998).

In order to insert the OWC device into the numerical wave channel shown in figure 3.14, the geometry of the device was simplified, as a means to make mesh

generation easier, as it was done by Oleinik (2020). In the simplified geometry, the hydropneumatic chamber has a rectangular shape, the turbine duct was placed vertically, and the walls were made with minimal thickness. In the turbine duct, the dimensions 11.3 m × 2.8 m were kept, but it was positioned vertically, above the hydropneumatic chamber. The width of the chamber was kept at 12 m, although in the real device there is a narrowing towards the top, and the distance from the mean water level to the entrance of the turbine duct was kept at 10 m. Figure 3.17 shows the OWC device inserted into computational domain, and figure 3.18 shows the computational domain, indicating the location of the device alongside the domain.

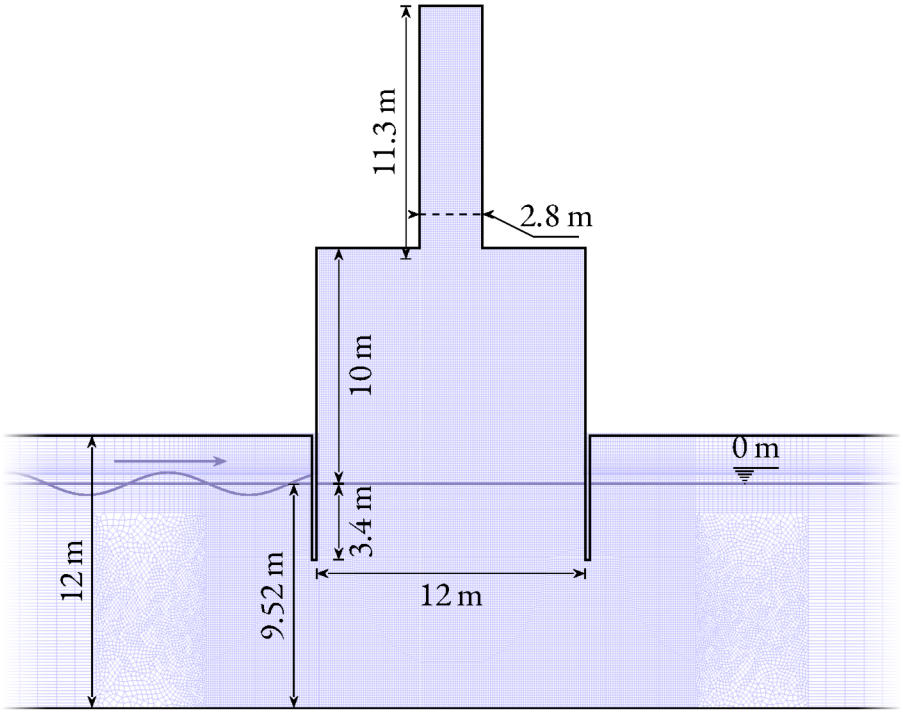


**Figure 3.17:** Dimensions of the OWC device used in this study.

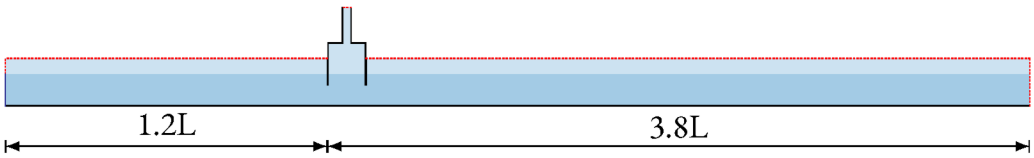


**Figure 3.18:** Computational domain with the OWC device inserted.

Oleinik (2020) draws attention to the fact that this simplification presents two main differences. The first is that the Pico island device is an onshore device, where the rear wall of the hydropneumatic chamber is a solid barrier that completely blocks the passage of waves, and the one adopted for this study is an offshore device. The reason behind this adaptation is to avoid wave reflection from the device and, thus, to allow comparison with the input data.

The second difference concerns the fact that the device in this study has a two-dimensional geometry, which then changes the ratio of area of the turbine duct and the hydropneumatic chamber. This is an important aspect regarding the power take-off. In the Pico island device, the ratio of area of the turbine duct and chamber area is obtained by (Oleinik, 2020):

$$r_{Pico} = \frac{\pi D^2/4}{a \times b} = \frac{\pi 2.8^2/4}{12 \times 12} \approx 0.0428 \tag{3.20}$$

and for the ratio for this study is:

$$r_{OWC_{Study}} = \frac{D}{a} = \frac{2.8}{12} \approx 0.233 \tag{3.21}$$

where $a$ and $b$ are the chamber dimensions, and $D$ is the turbine duct diameter. This comparison shows that the areas proportion is 5.46 times greater in the two-dimensional case. This means, that, if it is assumed for this purpose that the air is incompressible, the air flow in the turbine duct and all related variables are underestimated by 5.46 times due to the fact that a two-dimensional representation of the device is used (Oleinik, 2020).

Regarding the mesh spatial discretization inside the device, it was adopted a refined discretization, which is the same as the one used for the free surface region, i.e., 20 volumes per wave height. It is also important to mention that there is a region of transition from the wave channel before the device, with rectangular volumes, to the OWC region with square volumes, which was made using a hybrid mesh of triangular and quadrangular volumes. As it can be seen in figure 3.18, the OWC device was positioned at a distance of 1.2 wavelengths from the entrance of the wave channel, which corresponds to one wavelength, plus the transition zone to the refined region, of length $L/5$, and a refined region before the device, with length $L/5$.

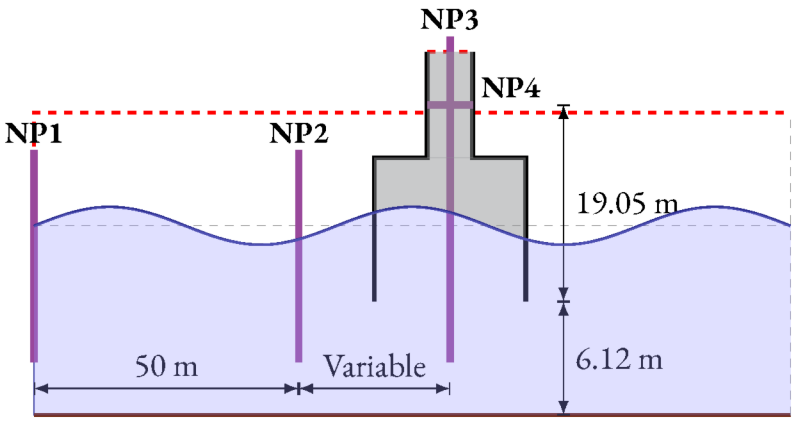


**Figure 3.19:** Numerical probes in the computational domain.

In order to measure physical quantities from the flow, numerical probes have been inserted in the numerical wave channel. Numerical probes (NP) and their respec-

tive positions in the computational domain are defined and presented in figure 3.19. Probes NP1, NP2, and NP3 measure free surface elevation, NP1 is located at $x = 0$ m, NP2 is located at $x = 50$ m, and NP3 is located at the center of the OWC device, which in this case is $x = 67.57$ m, but its position will change according to the different device geometries presented in section 3.5. NP4 is located at the middle of the turbine duct and measures static pressure and mass flow rate, variables needed to calculate the hydropneumatic power, as shown in equation 3.14. These measurements were obtained using the integral option in Fluent, which is calculated as follows (ANSYS Inc., 2013):

$$\int \phi \, dA = \sum_{i=1}^{n} \phi_i \, |A_i| \tag{3.22}$$

where $\phi_i$ is a variable field, in this case the amount of water in each volume, and $A_i$ is the area of each volume, but, since the numerical probe is a line, it represents the length of each volume.

Once the device geometry has been defined, it is now possible to apply the Constructal Design method to analyze other possible geometries for this device and to estimate the power available in the study area.

## 3.5 Application of Constructal Design Method

One of the objectives of this study is to analyze the effects of varying the geometry of an OWC device subjected to a realistic sea state. As shown in section 2.5, many works apply the Constructal Design method to geometrically analyze OWC devices, however employing realistic waves together with this methodology is the differential aspect of this study in relation to other works that involve the application of Constructal Design in sea wave energy.

As mentioned before, some parameters must be adopted in order to apply the method, namely geometric constraints, degrees of freedom, and performance indicators. In most cases, these constraints are areas or volumes, whose values do not change throughout the application, degrees of freedom are geometrical parameters that can be varied, respecting the constraints, and the performance indicator here is the available hydropneumatic power. The steps necessary to apply this method are presented in figure 3.20, as in Dutra *et al.* (2020).

In this case, the degree of freedom $H_1/L$ (ratio between height and length of the hydropneumatic chamber) will be varied, the degrees of freedom $H_2/l$ (ratio between height and length of the turbine duct) and $H_3$ (submergence depth of hydropneumatic chamber) were kept constant. These dimensions can be observed in figure 3.21.

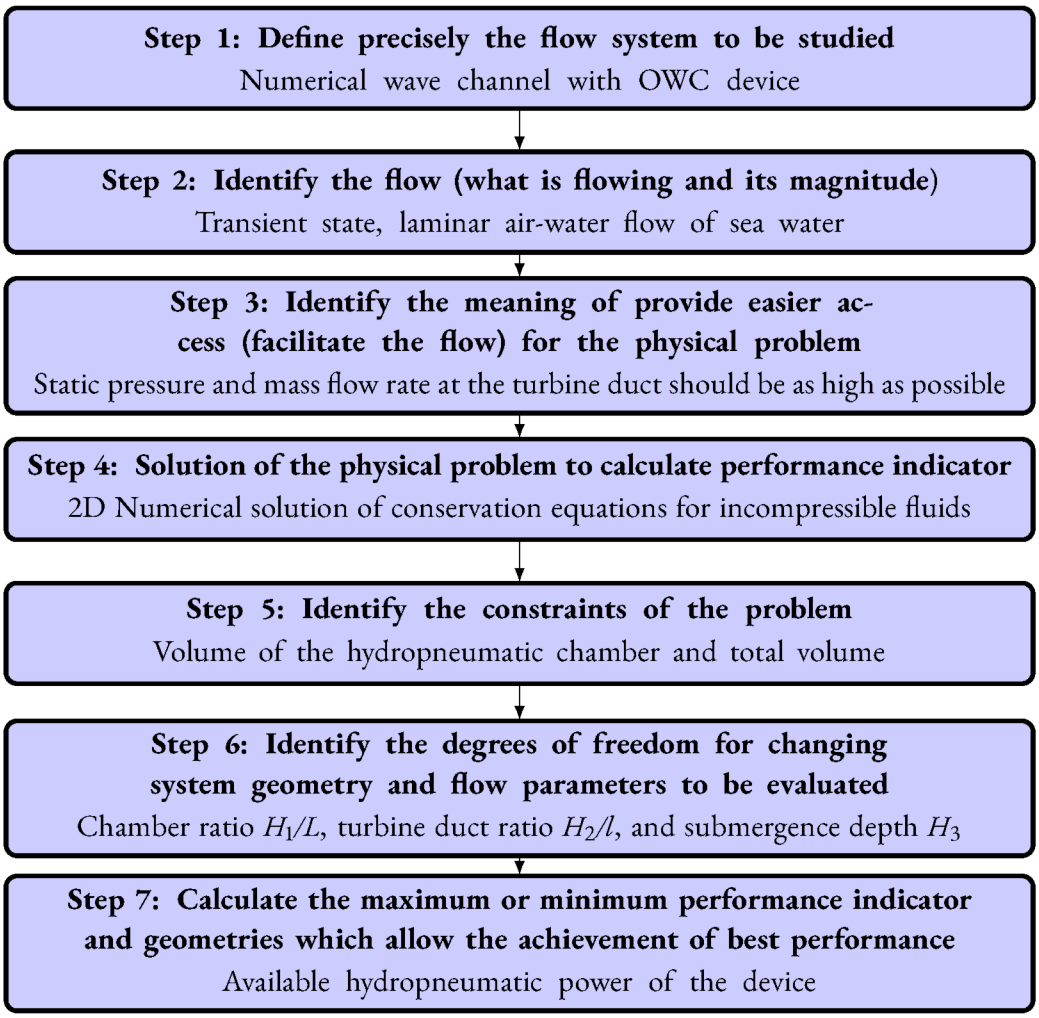


**Figure 3.20:** Summary flowchart of the Constructal Design method.

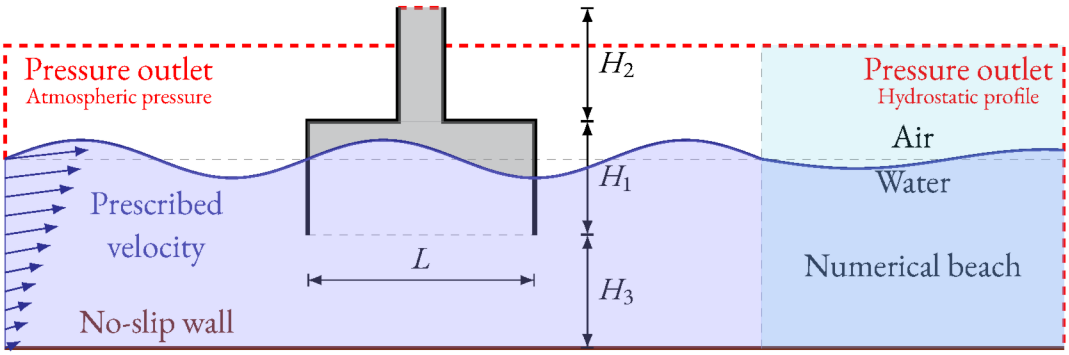


**Figure 3.21:** Representation of the computational domain and the physical dimensions used in the geometrical analysis.

The hydropneumatic chamber volume ($V_{HC}$) and the total volume of the OWC device ($V_T$) are the geometric constraints of the problem and were kept constant.

Volumes $V_{HC}$ and $V_T$, respectively, are described by:

$$V_{HC} = H_1 \, L \, L_1 \tag{3.23}$$

$$V_T = V_{HC} + H_2 \, l \, L_1 \tag{3.24}$$

where the third dimension $L_1$ is kept constant and has a value equal to one, so the problem is considered two-dimensional. From equation 3.23, it is possible to obtain the equations for the length and height of the hydropneumatic chamber, which will change accordingly to the degree of freedom $H_1/L$:

$$L = \left[ \frac{V_{HC}}{\left( \frac{H_1}{L} \right) L_1} \right]^{1/2} \tag{3.25}$$

$$H_1 = L \left( \frac{H_1}{L} \right) \tag{3.26}$$

Similarly, from equation 3.24, it is possible to obtain the equations for the length and height of the turbine duct:

$$l = \left[ \frac{V_T - V_{HC}}{\left( \frac{H_2}{l} \right) L_1} \right]^{1/2} \tag{3.27}$$

$$H_2 = l \left( \frac{H_2}{l} \right) \tag{3.28}$$

However, the ratio $H_2/l$ was kept constant for all simulations, with $H_2$ being equal to 11.3 m and $l$ equal to 2.8 m, as shown in section 3.4.

Next, the values for ratio $H_1/L$ were defined, which allowed to define the values for the lengths and heights of the hydropneumatic chambers to be simulated. Thus, as a criterion for defining the volume restriction of the device chamber, the dimensions similar to those of the OWC device at Pico island, Azores, Portugal, were adopted, where the length of the hydropneumatic chamber is 12 m and its height is 13.4 m, as shown in figure 3.16, which represents an $H_1/L$ value of 1.1167. For the minimum value of $H_1/L$ adopted, the adopted height of the hydropneumatic chamber was half of the height of the turbine duct, which led to $L$ equal to 28.46 m, $H_1$ equal to 5.65 m, and $H_1/L$ equal to 0.1985. For the maximum value of $H_1/L$ considered, the adopted length of the hydropneumatic chamber was three times the length of the turbine duct, which led to $L$ equal to 8.40 m, $H_1$ equal to 19.14 m, and $H_1/L$ equal to 2.2789. All values of $H_1/L$ considered in this study are presented in table 3.2.

The performance indicator to be considered throughout this study was the RMS mean of available hydropneumatic power of the OWC device, which must be maximized.

**Table 3.2:** Configurations of geometry adopted for the simulations in this study.

| **Case** | $H_1/L$ | $L$ (m) | $H_1$ (m) | $l$ (m) | $H_2$ (m) | $H_3$ (m) |
|---|---|---|---|---|---|---|
| **1** | 0.1985 | 28.46 | 5.65 | 2.80 | 11.30 | 6.12 |
| **2** | 0.4297 | 19.34 | 8.31 | 2.80 | 11.30 | 6.12 |
| **3** | 0.6608 | 15.60 | 10.31 | 2.80 | 11.30 | 6.12 |
| **4** | 0.8920 | 13.43 | 11.98 | 2.80 | 11.30 | 6.12 |
| **5** | 1.1167 | 12.00 | 13.40 | 2.80 | 11.30 | 6.12 |
| **6** | 1.3543 | 10.90 | 14.76 | 2.80 | 11.30 | 6.12 |
| **7** | 1.5854 | 10.07 | 15.97 | 2.80 | 11.30 | 6.12 |
| **8** | 1.8166 | 9.41 | 17.09 | 2.80 | 11.30 | 6.12 |
| **9** | 2.0478 | 8.86 | 18.15 | 2.80 | 11.30 | 6.12 |
| **10** | 2.2789 | 8.40 | 19.14 | 2.80 | 11.30 | 6.12 |

# 4 Results

This chapter presents the results obtained for the verification and validation of the hydrodynamic model (which include wave generation tests, numerical beach examination, mesh quality study, time step analysis, and study of the wave channel), for the numerical simulations performed with OWC device, and for the geometrical analysis performed with the Constructal Design methodology. The numerical simulations were performed in the CFD software Ansys Fluent, version 18.1, on a computer with processor Intel® Core™ i7-8700 CPU 3.20GHz and RAM memory of 16 GB.

## 4.1 Verification and Validation

As previously mentioned, the proposed methodology relies on the imposition of discrete wave velocity components, used as boundary conditions. Therefore, the spatial discretization at the region of velocity imposition is of prime importance. As shown in figure 3.8, four discretization arrangements were tested.

Figure 4.1 shows the free surface elevation at $x = 10$ m for each velocity imposition discretization, as well as the analytical solution for a regular $2^{nd}$ order Stokes wave. Since it is regular waves that are being analyzed, the dimensionless parameter $t/T$ was used to present the ratio between simulated time ($t$) and wave period ($T$).

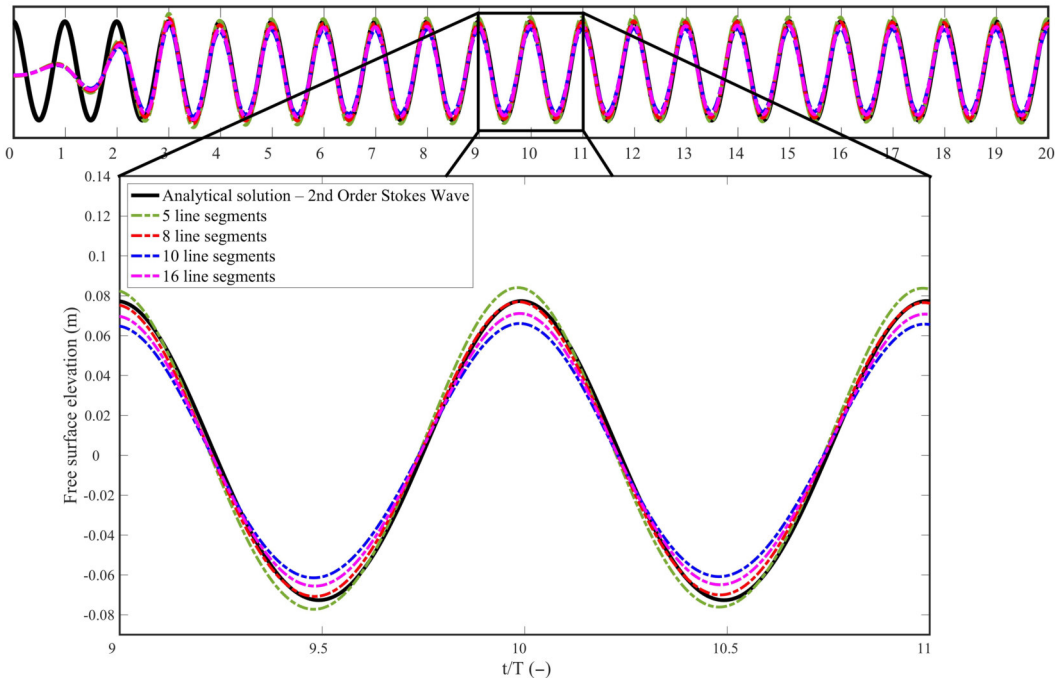


**Figure 4.1:** Comparison of the discretization at the wave generation region for the validation procedure.

To assist choosing the optimal discretization of the wave generation region for the validation procedure, NRMSE was calculated using equation (3.18), with relation to the analytical solution. The NRMSE value for each of the simulations presented in figure 4.1 is presented in table 4.1.

**Table 4.1:** NRMSE values for velocity inlet discretization at the wave generation region.

| Discretization | NRMSE (%) |
|---|---|
| 5 line segments | 3.99 |
| 8 line segments | 2.79 |
| 10 line segments | 6.20 |
| 16 line segments | 4.21 |

As shown in table 4.1, the velocity inlet discretization which presented the smallest percentage of error was the one with 8 velocity profiles, with a NRMSE value of 2.79 %. This result is in accordance with that achieved by Machado *et al.* (2017), therefore, this number was adopted for the validation simulations.

As mentioned in section 3.3, a numerical beach was implemented to prevent wave reflection at the end of the wave channel, which would interfere with wave propagation along the channel. For a proper wave damping, five linear damping coefficient ($C_1$) values were tested, as presented in table 3.1. Figure 4.2 shows the free surface elevation at the end of the channel for each value of $C_1$ adopted.

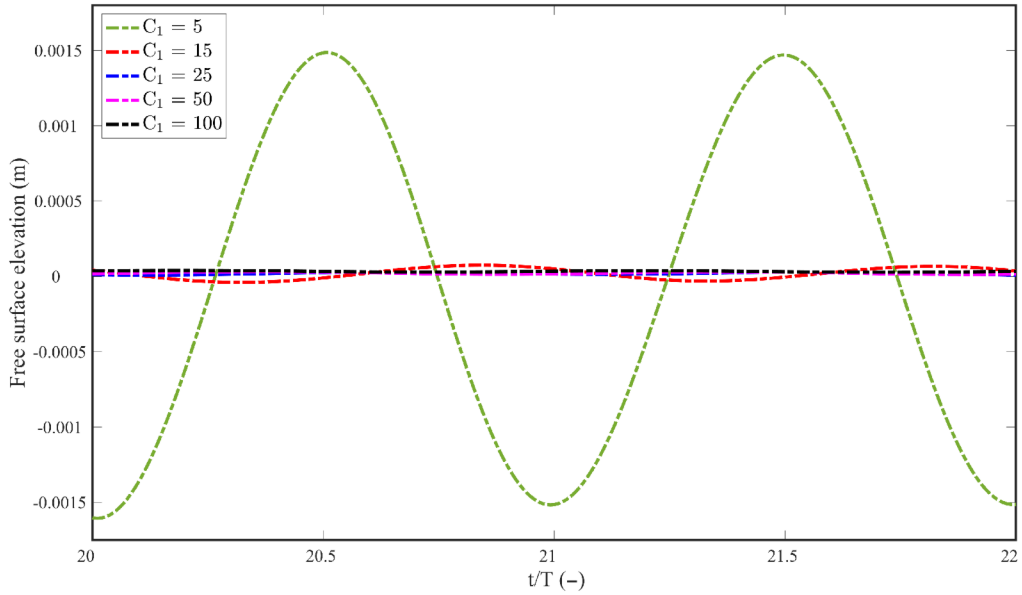


**Figure 4.2:** Comparison of free surface elevation at the end of the channel, according to the values adopted for numerical beach coefficient $C_1$.

To measure wave damping efficiency, a ratio between the wave height obtained

at the end of the channel ($x$ = 65.00 m) for each linear damping coefficient and the wave height at the beginning of the numerical beach ($x$ = 49.92 m) was calculated. The ratio value for each verification simulation is presented in table 4.2.

**Table 4.2:** Wave height ratio for each value of linear damping coefficient analyzed.

| Values of $C_1$ | Wave height ratio (%) |
|---|---|
| 5 | 2.15 |
| 15 | 0.13 |
| 25 | 0.07 |
| 50 | 0.06 |
| 100 | 0.06 |

One can observe in table 4.2 that the smallest ratio values were the ones obtained with $C_1$ values of 50 and 100. However, the difference between them and the ratio value for $C_1$ equals 25 was negligible. As this result is rather similar to that obtained by Lisboa, Teixeira, and Didier (2017), a linear damping coefficient of 25 was adopted.

Next, mesh spatial discretization was analyzed. For that, 4 simulations were performed, with 8 line segments at the region of wave generation and a $C_1$ coefficient value of 25 at the numerical beach. In each simulation, a different mesh was employed, using the dimensions presented in table 3.1.

The analysis was performed by means of equation (3.18), and compared both numerical and analytical free surface elevation at position $x$ = 10.00 m. It should be mentioned that, at the beginning of every simulation, the wave channel is at rest and, due to the flow inertia, the first waves generated are more dampened, as it can be seen in figure 4.1, leading to considerable deviations in the comparison with the analytical results. Therefore, this interval of time in which wave generation is not stable, which corresponded to an interval of 11.09 s, was disregarded. The comparison between the free surface elevation of each mesh tested and the analytical solution is presented in figure 4.3, and the corresponding NRMSE values are presented in Tab. 4.3.

**Table 4.3:** NRMSE values for mesh discretization in the validation procedure.

| Mesh number | NRMSE (%) |
|---|---|
| 1 | 7.95 |
| 2 | 4.27 |
| 3 | 5.04 |
| 4 | 1.15 |

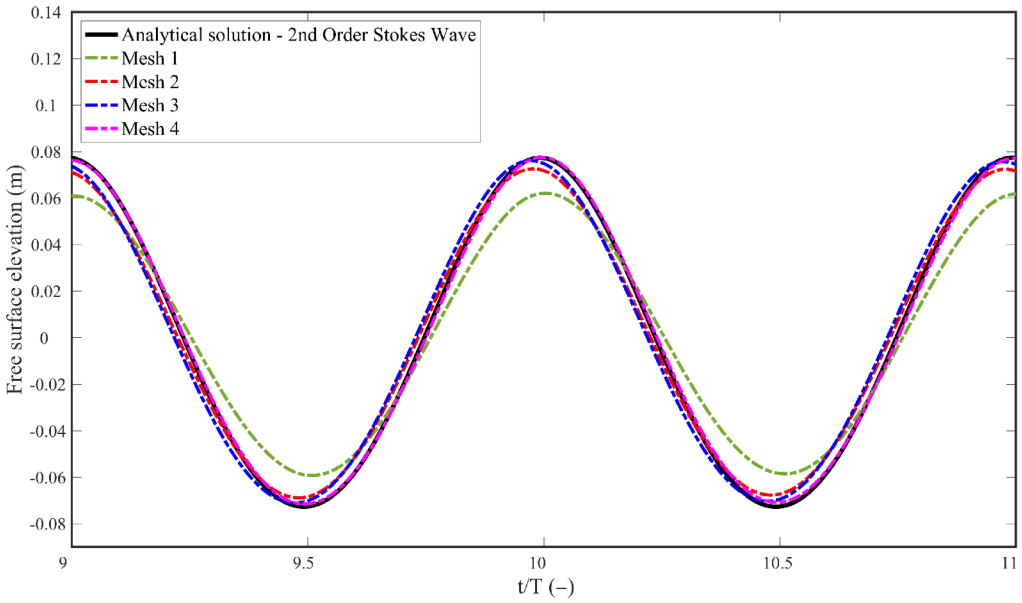


**Figure 4.3:** Comparison of mesh discretizations tested for the validation procedure.

As expected, mesh number 1, which contained a coarser grid, showed the greatest discrepancy, with a NRMSE value of 7.95%. On the other hand, mesh number 4, which possessed the finest grid, presented the smallest NRMSE value (1.15%), and, therefore, it was adopted for the validation simulations.

Since this is a transient problem, the time step influence was evaluated. For this analysis, mesh number 4 was employed, with 8 line segments at the region of wave generation, and a $C_1$ coefficient value of 25 at the numerical beach. Five simulations were performed, varying the time step, using the values pointed in section 3.3. The comparison between he numerical solution obtained with each time step tested and the analytical solution given by equation (3.13) is presented in figure 4.4, and the corresponding NRMSE values are presented in table 4.4.

**Table 4.4:** NRMSE value for each time step analyzed.

| Time step | NRMSE (%) |
|---|---|
| $T/50$ | 3.45 |
| $T/100$ | 2.15 |
| $T/200$ | 1.46 |
| $T/400$ | 1.15 |
| $T/800$ | 1.16 |

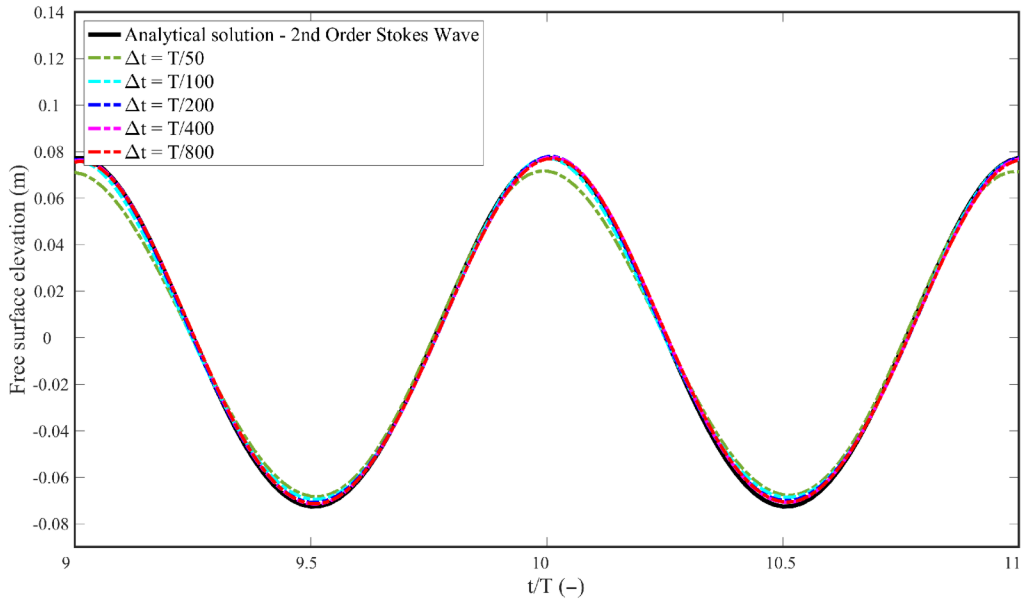


**Figure 4.4:** Comparison of time step values tested in this study.

As it can be seen in figure 4.4 and table 4.4, free surface elevation was more dissonant when using $\Delta t$ equals $T/50$. It should be highlighted that the NRMSE value found using this temporal discretization can be considered fairly small. However, the smallest NRMSE was obtained with a time step equal to $T/400$. It is also worth mentioning that an approximate value was encountered by Gomes *et al.* (2018), who reached good results with a time step of $T/500$. Thus, the time step value of $T/400$ was adopted for the simulation of the validation procedure.

It is important to highlight that the verification tests performed ensured a proper wave generation and propagation, including analysis of the discretization at the region of velocity imposition, linear damping coefficient $C_1$ at the numerical beach, mesh spatial discretization, and temporal discretization. So far, great results were obtained with 8 line segments at the region of wave generation, $C_1$ equal to 25, mesh elements throughout the channel with dimensions of $L/40$, mesh elements inside free surface refinement zone with dimensions of $H/25$, and a time step value of $T/400$.

Then, the OWC device was inserted into the numerical wave channel and three simulations were performed, using either laminar flow or turbulent flow, with turbulence models $k$-$\epsilon$ and $k$-$\omega$ SST. With the results obtained from these simulations, the free surface elevation obtained by the numerical gauges located outside and inside the hydropneumatic chamber was compared with wave gauges WG1, WG2, WG3, and WG4 (see figure 3.13 for more details). The pressure obtained by the numerical probe located inside the hydropneumatic chamber was also compared with the pressure sensor used in the experiment in which the validation simulation was based on.

The free surface elevation for wave gauges WG1, WG2, WG3, and WG4 can be seen in figures 4.5 and 4.6. All results are presented for five wavelengths, the NRMSE for each simulation was calculated, in comparison to the experimental results, and it

is shown in table 4.5.

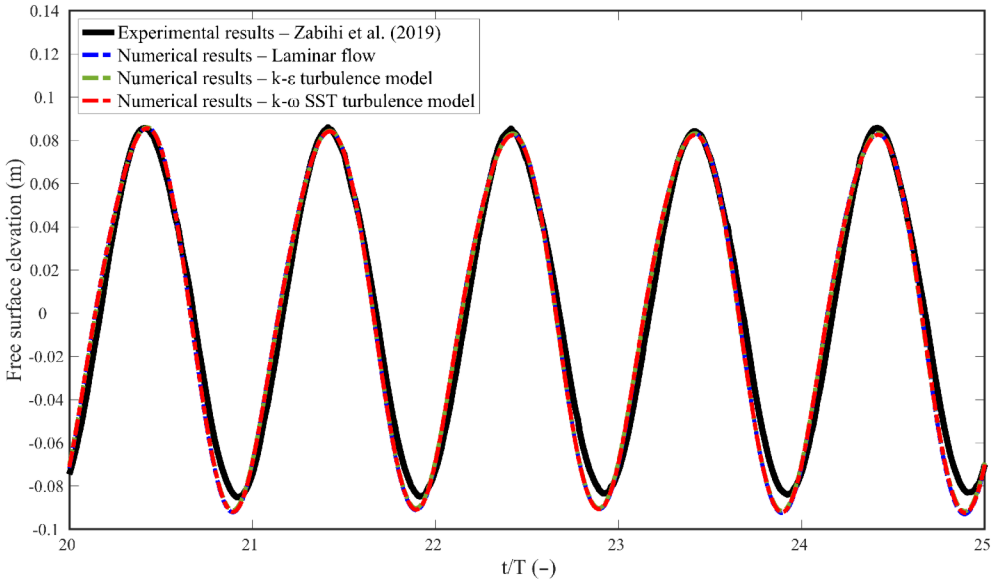


**(a)** Free surface elevation at wave gauge WG1, experimental versus numerical results.

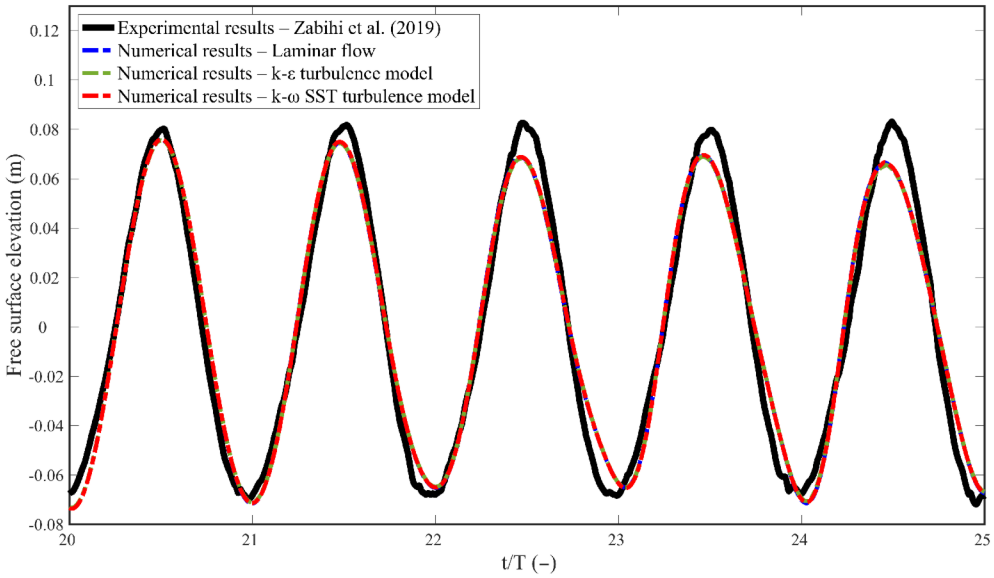


**(b)** Free surface elevation at wave gauge WG2, experimental versus numerical results.

**Figure 4.5:** Free surface elevation of wave gauges located outside the hydropneumatic chamber.

As indicated in figure 3.13, wave gauges WG1 and WG2 are located previously to the OWC device, which has less effect of nonlinearity. This aspect can be observed in both numerical and experimental results of figure 4.5, where it is possible to observe that the free surface elevation follows a more regular pattern.

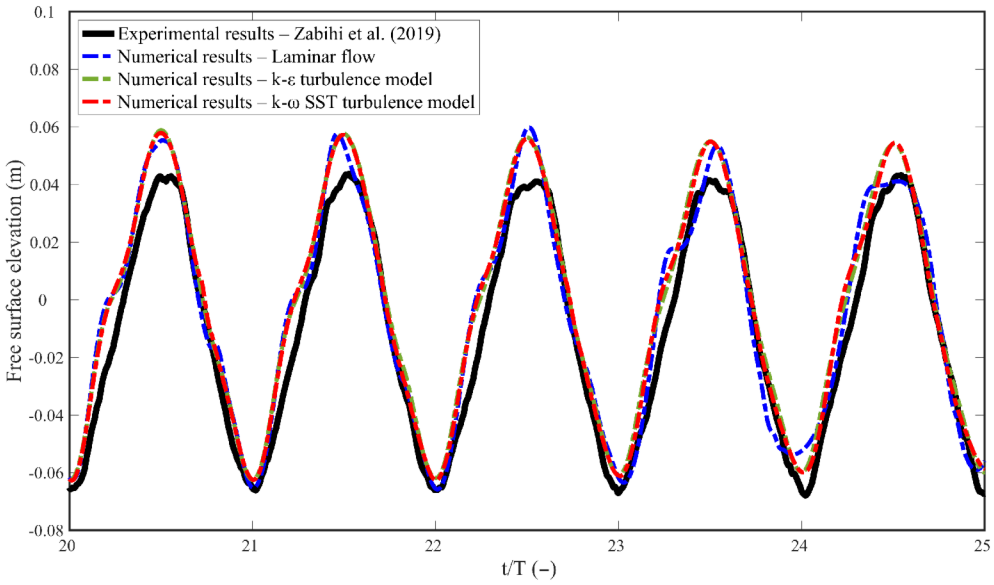


**(a)** Free surface elevation at wave gauge WG3, experimental versus numerical results.

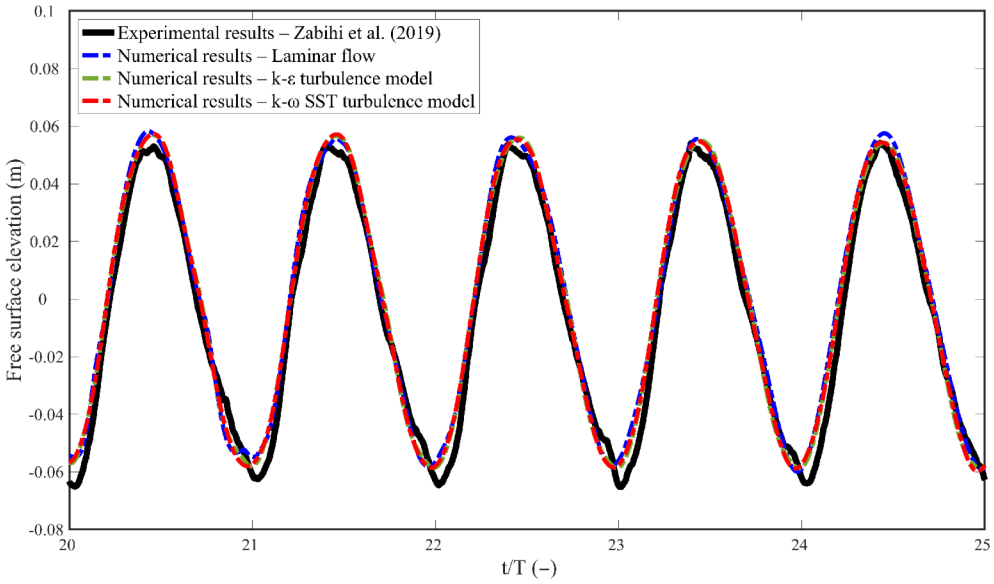


**(b)** Free surface elevation at wave gauge WG4, experimental versus numerical results.

**Figure 4.6:** Free surface elevation of wave gauges located inside the hydropneumatic chamber.

As Zabihi, Mazaheri, and Namin (2019) affirmed, nonlinear interactions are more noticeable inside the hydropneumatic chamber; this explains greater NRMSE values for wave gauges WG3 and WG4, which are located inside the chamber. As it can be observed in figure 4.6a, there are some disparities among wave crests of numerical and experimental results for WG3, however, that is less evident in WG4 (figure 4.6b).

In addition, water free surface flow for nine instants along a wave period is presented in figure 4.7. One can observe how wave crests and troughs are more accentuated previously to the hydropneumatic chamber than afterwards, due to the wave damping when interacting with the walls of the device.

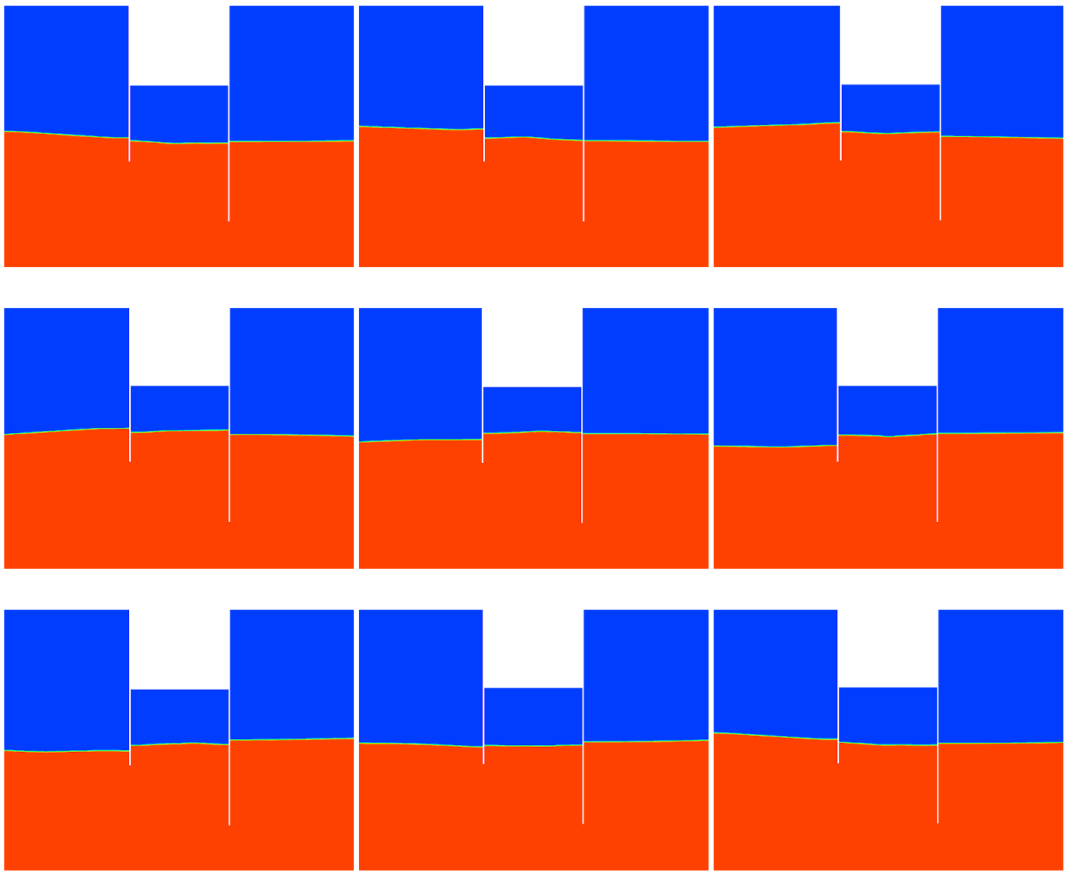

**Figure 4.7:** Instantaneous free surface flow along a wave period, from 35.75 s to 37.95 s (Maciel *et al.*, 2021).

The air pressure inside the hydropneumatic chamber was also analyzed, for it is significant when reproducing the hydrodynamics of the OWC device, and it can be seen in figure 4.8. It should be highlighted that the numerical results presented excellent accordance with the experimental results, being able to capture the general fluid-dynamic behavior present in the device.

**Table 4.5:** NRMSE value for numerical wave gauges and pressure sensor in the validation simulation.

| **Flow regime** | **NRMSE (%)** | | | | |
|---|---|---|---|---|---|
| | **WG1** | **WG2** | **WG3** | **WG4** | **PS** |
| Laminar flow | 3.37 | 5.07 | 9.35 | 5.27 | 4.22 |
| Turbulent – k-$\epsilon$ | 3.27 | 5.03 | 8.23 | 4.93 | 4.40 |
| Turbulent – k-$\omega$ SST | 3.32 | 5.16 | 9.03 | 5.11 | 4.63 |

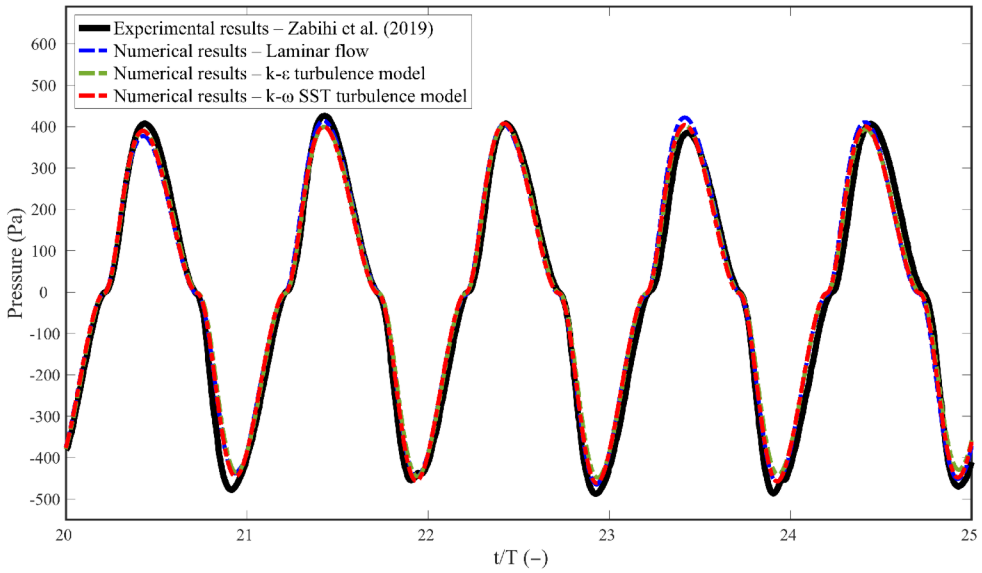


**Figure 4.8:** Air pressure inside the hydropneumatic chamber, experimental versus numerical results.

As one can note, overall, numerical results presented a good agreement with results from the experiments, although nonlinear interaction was more present in WG3. From the NRMSE values, it is possible to notice that the $k$-$\epsilon$ turbulence model provided a behavior more similar to those found in the experiments. However, the other turbulence model, as well as the laminar approach, also conduct to accurate results, as it can be viewed in figure 4.8. Therefore, considering that there was not a significant difference in results, a laminar regime was adopted for the irregular waves simulations. From the results shown, one can say that the hydrodynamic numerical model adopted for this study was successfully verified and validated, which fulfills specific objective II.

## 4.2 OWC subjected to realistic sea state

With the hydrodynamic model successfully validated, it was used to numerically simulate an OWC device subjected to realistic sea waves. Since the waves used in the upcoming simulations are different from those in the validation procedure, a verification of irregular waves generation was performed.

As it was done in the validation procedure, subregion fractioning at the entrance of the wave channel was studied. This is an important test within this methodology, since it is at this region that transient discrete velocity data is imposed to the velocity profile as boundary condition. Therefore, four discretization arrangements were tested, with 8, 10, 12, and 14 line segments as velocity inlet boundary condition.

Figure 4.9 shows the free surface elevation at $x = 0$ m during 5 min of simulation for each velocity imposition discretization, as well as the free surface elevation obtained by converting spectral data from Tomawac (section 3.1). Figure 4.10 shows the same

results, however with a smaller time interval (160 s $\leq t \leq$ 220 s), where the differences between free surface elevations are more noticeable.

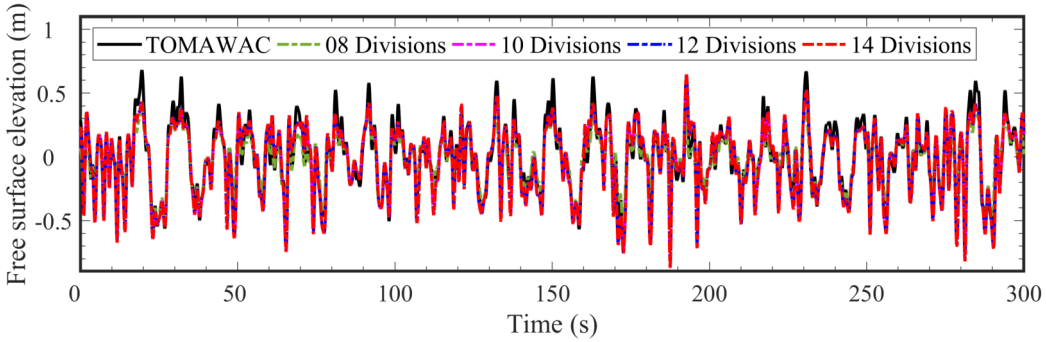


**Figure 4.9:** Free surface elevation at $x = 0$ m for different velocity inlet discretizations at the wave generation region.

As it can be seen in figure 4.9, free surface elevation at crests and troughs vary considerably, in this case, statistical measure NRMSE is not fitted to analyze the error in these simulations. Therefore, RMSE (equation (3.17)) was calculated for each velocity inlet discretization at the wave generation region with relation to the free surface elevation obtained by converting spectral data from Tomawac. RMSE values for each simulation can be observed both in figure 4.10 and table 4.6.

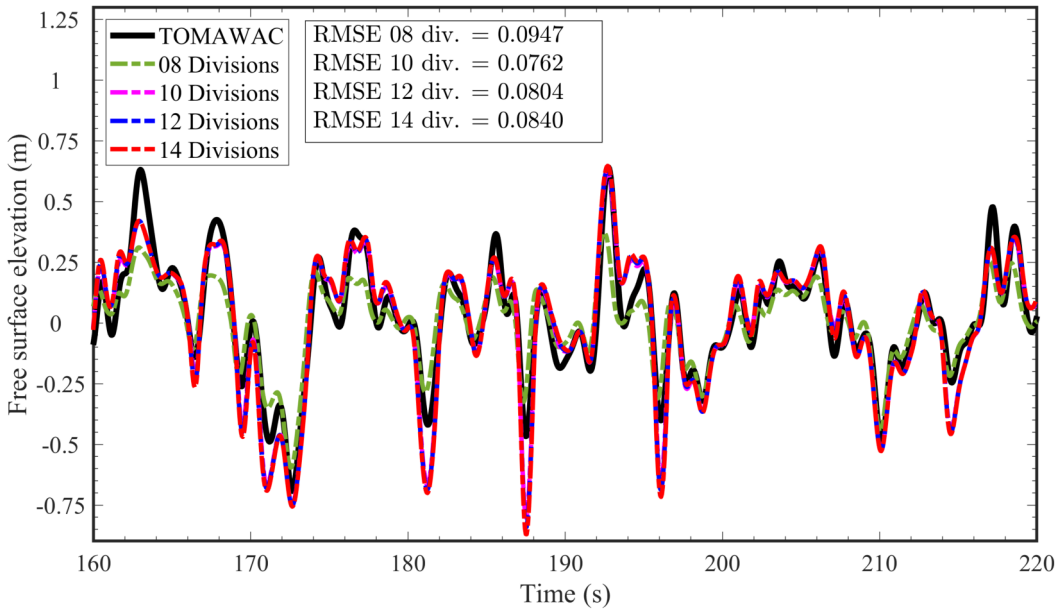


**Figure 4.10:** Free surface elevation at $x = 0$ m for different velocity inlet discretizations at the wave generation region.

As shown in figure 4.10 and table 4.6, the velocity inlet discretization which presented the smallest error was the one with 10 line segments, with a RMSE value of 0.0762 m. In contrast, the discretization which presented the greatest error was the one with 8 line segments, with a RMSE value of 0.0947 m. This is a different result

from the one obtained in the validation procedure and by Machado *et al.* (2017) and Maciel *et al.* (2021), where the discretization which presented the smallest error was the one with 8 line segments; and from Machado *et al.* (2021), where the discretization employed had 14 line segments. Therefore, based on the results obtained in this investigation, the discretization with 10 velocity profiles at the entrance of the wave channel was adopted for the forthcoming simulations.

**Table 4.6:** RMSE values for velocity inlet discretization at the wave generation region.

| Discretization | RMSE (m) |
|---|---|
| 8 line segments | 0.0947 |
| 10 line segments | 0.0762 |
| 12 line segments | 0.0804 |
| 14 line segments | 0.0840 |

It is important to keep in mind that the generation of waves using this methodology is linked to the fractioning of the region where wave velocity data is imposed as boundary condition. Therefore, it is important to analyze wave generation behavior according to the region fractioning, for the number of line segments might not be enough to reproduce successfully irregular waves, or, if it is too much, it might introduce non-linearity into the simulation, which is a possible explanation for the results shown in figure 4.10 and table 4.6.

Another important factor analyzed was that during the spectral data conversion, the orbital wave velocity can be measured at different locations in each line segment (see figure 3.15) before being converted to wave velocity components $u$ and $w$. Therefore, the location from where, alongside each line segment, the wave velocity components are calculated were tested. For this, wave velocity components $u$ and $w$ were calculated at three different locations for each velocity profile: bottom, middle, and top of each line segment. It is important to mention that, up until now, wave velocity data has been calculated at the middle of each line segment. As mentioned before, this test has not yet been performed for studies which employ the WaveMIMO methodology.

Figure 4.11 shows the free surface elevation at $x = 0$ m during 5 min of simulation according to the location from where the wave velocity components are calculated, as well as the free surface elevation obtained by converting spectral data from Tomawac. Figure 4.12 shows the same results, however with a smaller time interval (160 s $\leq t \leq$ 220 s), where the differences between free surface elevations are more noticeable.

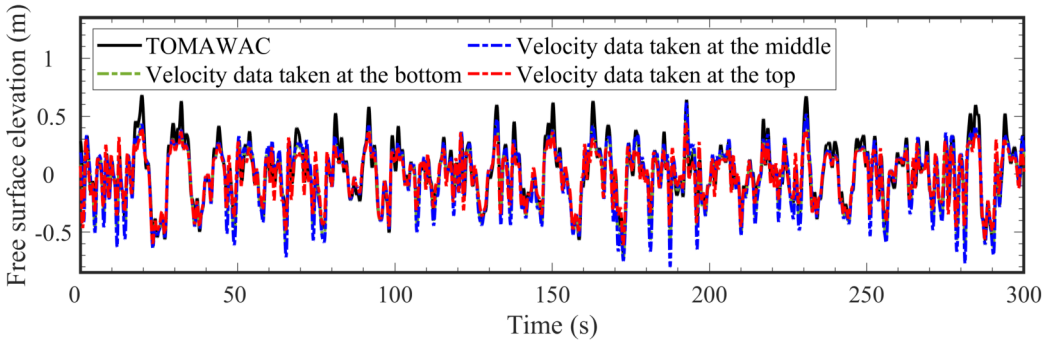


**Figure 4.11:** Free surface elevation at $x = 0$ m for different locations from where, alongside each line segment, wave velocity data is calculated.

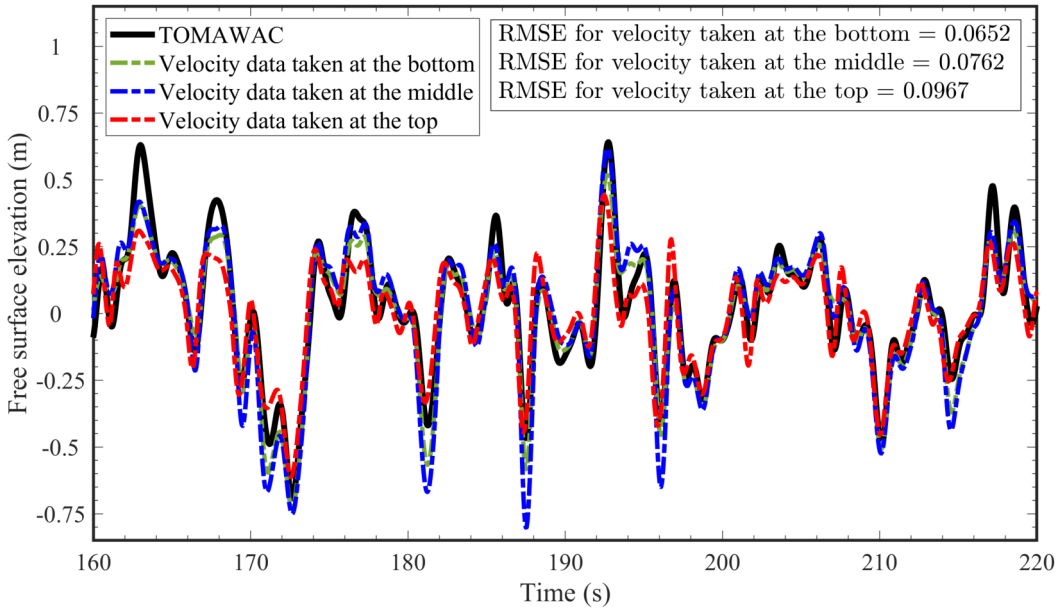


**Figure 4.12:** Free surface elevation at $x = 0$ m for different locations from where, alongside each line segment, wave velocity data is calculated.

One can observe from figure 4.12 and table 4.7 that the location from where wave velocity data is calculated which presented the smallest error was when wave velocity was calculated at the bottom of each line segment, with a RMSE value of 0.0652 m. This is a rather intriguing result, because, since the top location is closer to the free surface, it would be expected that it presented results more similar to the free surface elevation obtained by converting spectral data from Tomawac. On the contrary, however, the proximity to the free surface leads to higher error values. A possible explanation for this phenomena is that the free surface is a region of greater sensibility to the velocity field, and imposing higher velocity values to the portion of water column closer to the free surface might lead to a higher error.

**Table 4.7:** RMSE values for velocity inlet discretization at the wave generation region.

| Location of velocity data acquisition | RMSE (m) |
|---|---|
| Velocity data calculated at the bottom of each line segment | 0.0652 |
| Velocity data calculated at the middle of each line segment | 0.0762 |
| Velocity data calculated at the top of each line segment | 0.0967 |

Therefore, for the numerical simulations with the OWC device, wave velocity data was calculated at the bottom of each line segment. And, since the OWC device was numerically subjected to the action of irregular waves, it is possible to state that specific objective III was fulfilled.

The verification tests performed ensured a proper wave generation and propagation, including analysis of the discretization at the region of velocity imposition and location from where, alongside each line segment, wave velocity data is calculated. So far, great results were obtained with 10 line segments at the region of wave generation, and when wave velocity was calculated at the bottom of each line segment. Concerning the spatial discretization of the domain, as mentioned in section 3.4.1, it was adopted the same as Machado *et al.* (2021), where the domain was vertically discretized into 60 volumes in the region with only water, 20 volumes per wave height ($H$ = 0.67 m) in the free surface region and 30 volumes in the region with only air, and horizontally, the discretization was 50 volumes per wavelength ($L$ = 51.6 m). As for the temporal discretization, it was also adopted the same as the one applied by Machado *et al.* (2021), a time step $\Delta t$ = 0.05 s.

## 4.3 Application of the Constructal Design Method

Next, the OWC device was inserted into the numerical wave channel and it was numerically simulated, subjected to irregular realistic waves. Different geometries for the device were considered, applying the Constructal Design method to define such geometries. The objective here is to optimize the two-dimensional geometry of the OWC device, in order to maximize the power generation by the device in the realistic wave climate. To do so, the obtained results were compared among each other, characterizing a geometrical optimization through exhaustive search technique.

The goal is to analyze the degree of freedom $H_1/L$, which is the ratio between the height and length of the oscillating water column chamber. The degrees of freedom $H_2/l$, which is the ratio between the height and the length of the turbine, and $H_3$, submergence depth of hydropneumatic chamber, were kept constant. Volume of the hydropneumatic chamber ($V_{HC}$), shown in equation (3.23), and total volume of the device ($V_T$), shown in equation (3.24), were also kept constant and are the geometric constraints of the problem. The variable physical dimensions of the computational

domain can be seen in figure 3.21.

Using the formulation presented in section 3.5, the values $H_2/l$ = 4.0357, $H_3$ = 6.12 m, $V_{HC}$ = 160.80 m$^2$, and $V_T$ = 192.44 m$^2$ were adopted for the methodology application. Therefore, it was possible to vary the degree of freedom $H_1/L$ and to use equations (3.25) and (3.26) to calculate the geometries for the OWC devices. Table 3.2 shows the values adopted for the degrees of freedom $H_1/L$.

Next, the free surface elevation obtained by the numerical probes located at the beginning of the wave channel were compared with the free surface elevation obtained by converting spectral data from Tomawac using the WaveMIMO methodology. Figure 4.13 shows the free surface elevation at $x$ = 0 m during 15 min of simulation for each geometry corresponding to values of $H_1/L$, as well as the free surface elevation obtained by the WaveMIMO methodology (section 3.1).

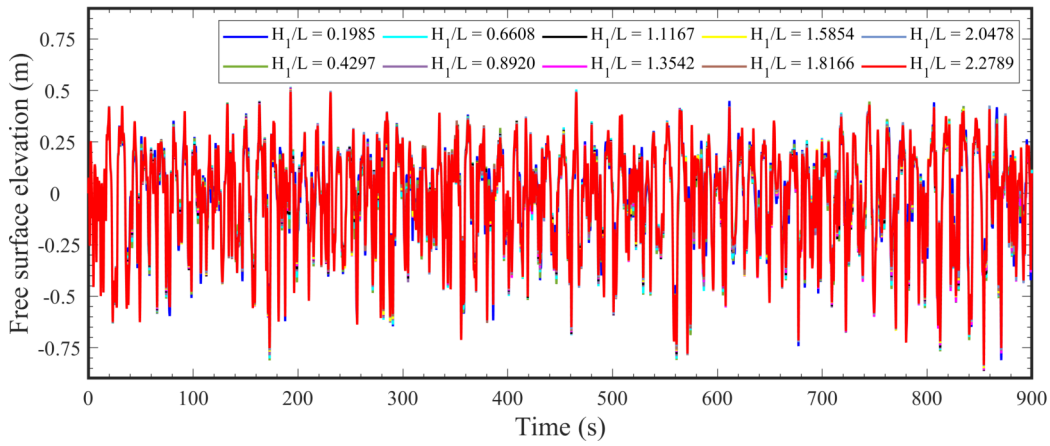


**Figure 4.13:** Free surface elevation at $x$ = 0 m for different values of $H_1/L$.

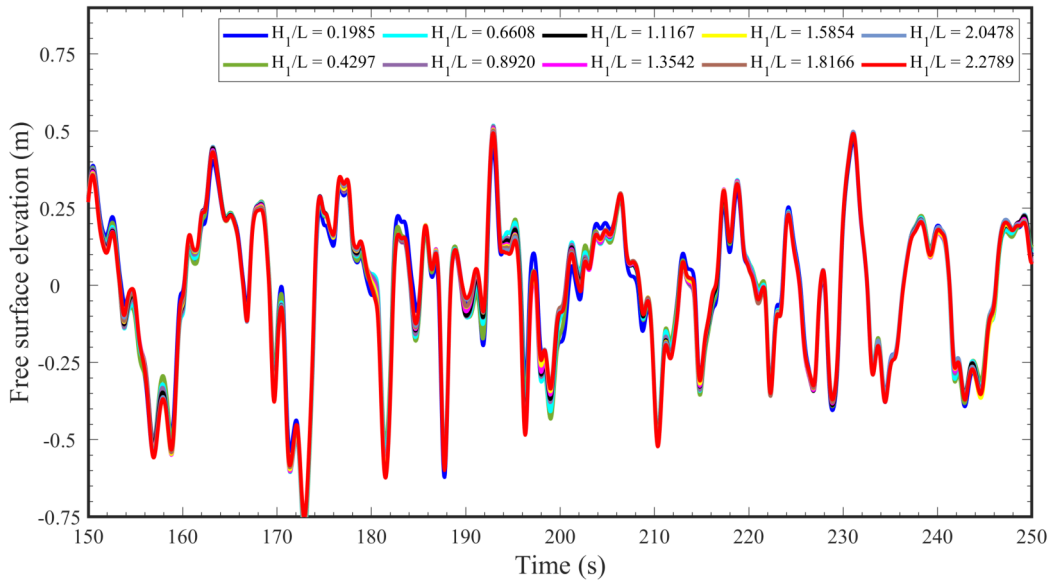


**Figure 4.14:** Free surface elevation at $x$ = 0 m for different values of $H_1/L$ (detail).

Figure 4.14 shows the same results, however with a smaller time interval (150 s $\leq t \leq$ 250 s), where the differences between free surface elevations are more noticeable. It is possible to observe a small difference between crests and troughs, even though all simulations used the same data as velocity inlet boundary conditions. This is possibly due to the wave reflection caused by the walls of the OWC device, and, since each device simulated has a different geometry, the reflected waves behave differently from each simulation. The corresponding RMSE at $x$ = 0 m, calculated with relation to the free surface elevation obtained by converting spectral data from Tomawac, for each $H_1/L$ value analyzed is presented in table 4.8.

**Table 4.8:** RMSE values for different values of degree of freedom $H_1/L$.

| $H_1/L$ (–) | RMSE (m) |
|---|---|
| 0.1985 | 0.0721 |
| 0.4297 | 0.0725 |
| 0.6608 | 0.0731 |
| 0.8920 | 0.0740 |
| 1.1167 | 0.0739 |
| 1.3543 | 0.0748 |
| 1.5854 | 0.0742 |
| 1.8166 | 0.0752 |
| 2.0478 | 0.0762 |
| 2.2789 | 0.0764 |

It is important to highlight that a direct comparison of the elevation time series for different locations in the wave channel does not show good results, because the wave propagation velocity varies with their length, and, since the series is composed by the sum of several sinusoidal components of different lengths, each one propagates with a different velocity and this causes the shape of the time series to evolve over time (Oleinik, 2020). Figure 4.15 shows the time series of free surface measured at the entrance of the wave channel, superimposed with the elevation at the center of the OWC device (with configuration $H_1/L$ = 1.1167), which are visibly displaced with respect to each other due to the propagation of waves along the channel. Direct comparison, in the case of irregular waves, is only possible when comparing two time series at the same point in space.

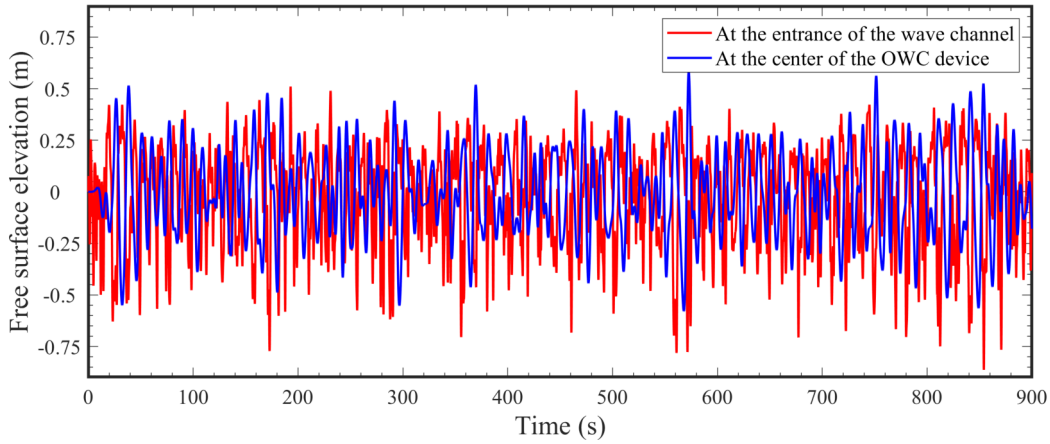


**Figure 4.15:** Free surface elevation at $x$ = 0 m and $x$ = 67.57 m (center of the OWC device) for $H_1/L$ = 1.1167.

Thus, to verify the hydrodynamic model ability to reproduce the sea state, the spectral density of free surface elevation was calculated. This was done using the same procedure as that of Oleinik, Machado, and Isoldi (2021). Spectral density was calculated for three different locations, at $x$ = 0 m, $x$ = 50 m, and $x$ = 67.57 m (center of the OWC device) for $H_1/L$ = 1.1167, as shown in figure 4.16.

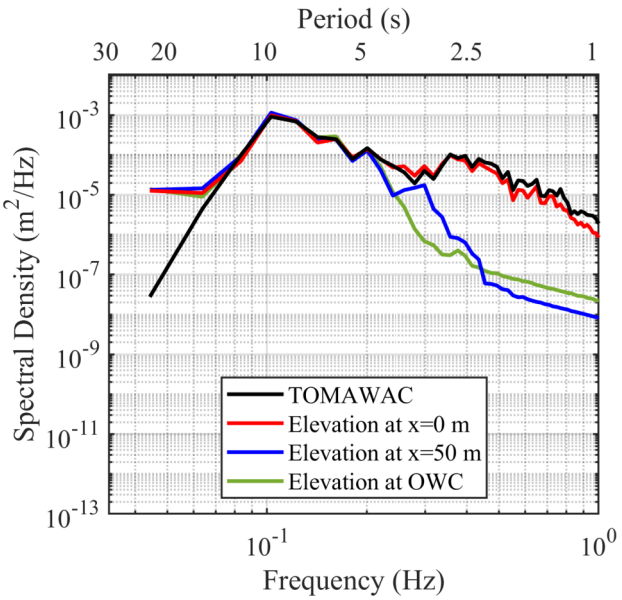


**Figure 4.16:** Spectra of free surface elevation at $x$ = 0 m, $x$ = 50 m, and $x$ = 67.57 m (center of the OWC device) for $H_1/L$ = 1.1167.

It is possible to notice from the results shown in figure 4.16 that for waves with periods between approximately 15 s and 5 s, there is a good agreement between the results. However, for wave periods greater than 15 s and less than 5 s, there is divergence. This behavior is very similar to that encountered by Machado *et al.* (2021).

In addition to the free surface elevation, static pressure and mass flow rate were also measured using numerical probes present in the numerical wave channel, whose locations are indicated in figure 3.19. Figure 4.17 shows the static pressure at the turbine duct, during 15 min of simulation for each geometry corresponding to values of $H_1/L$; while figure 4.18 presents the same results but in an interval between 150 s and 250 s, highlighting the existing differences. As mentioned in section 3.4.2, coordinates of the center of the OWC device change according to the device geometry.

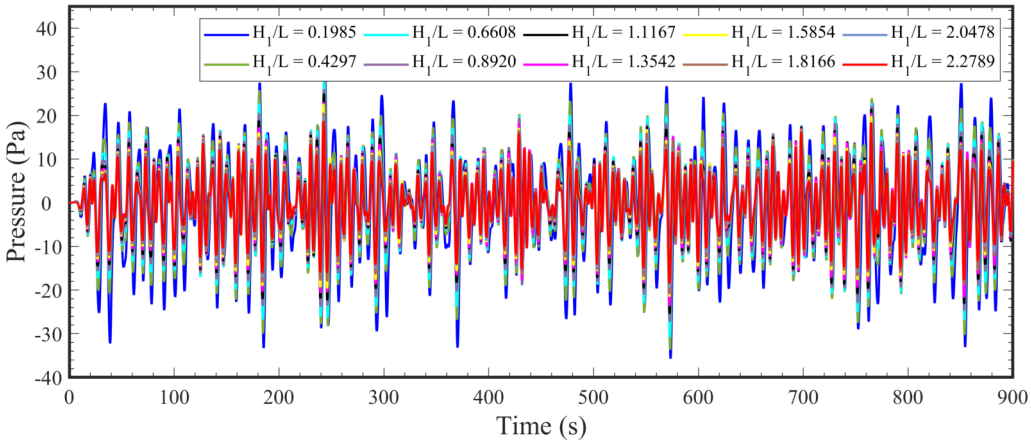


**Figure 4.17:** Static pressure at the turbine duct for different values of $H_1/L$.

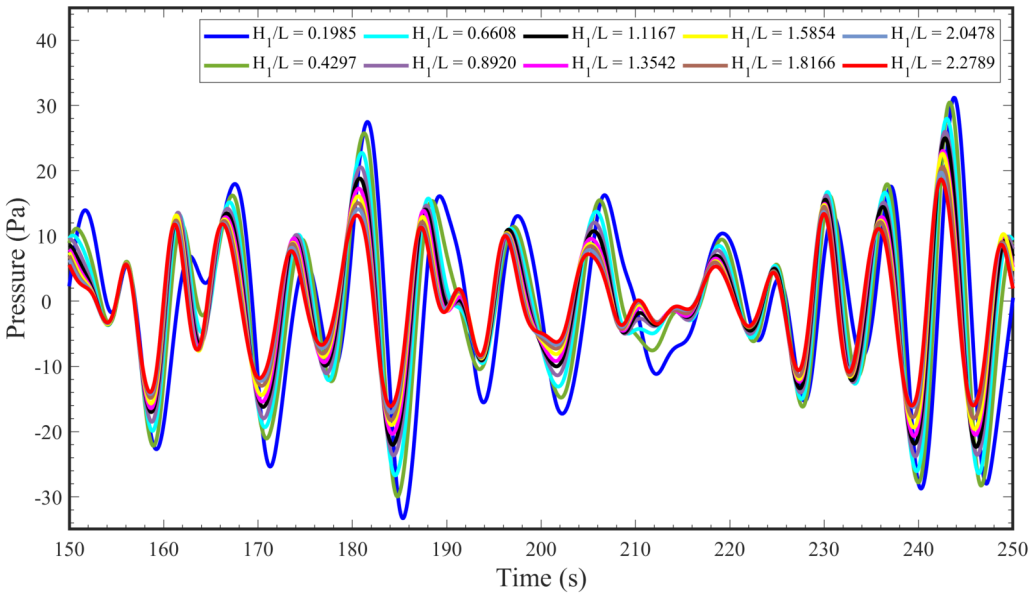


**Figure 4.18:** Static pressure at the turbine duct for different values of $H_1/L$ (detail).

Figure 4.19 shows the mass flow rate at the turbine duct, during 15 min of simulation for each geometry corresponding to values of $H_1/L$. Figure 4.20 shows the same results, however with a smaller time interval (150 s $\leq t \leq$ 250 s), where the

differences between mass flow rate values are more noticeable. It is possible to notice from figures 4.18 and 4.20 that there is a difference in phase between the geometries simulated. This is possibly caused by the distance between the front wall and the center of the device, which is shortened as $H_1/L$ values increase, thus causing the waves to reach the center of the device faster in low $H_1/L$ value geometries.

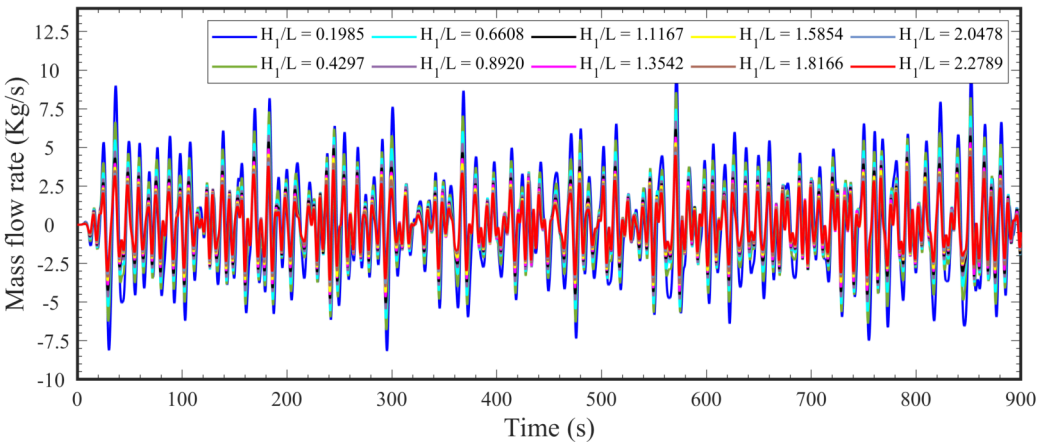


**Figure 4.19:** Mass flow rate at the turbine duct for different values of $H_1/L$.

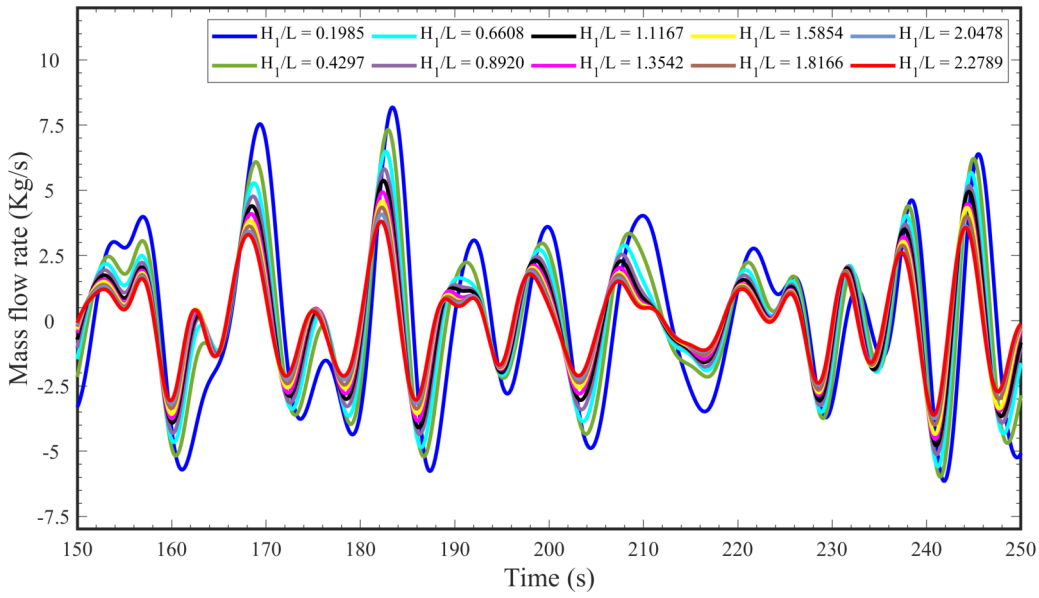


**Figure 4.20:** Mass flow rate at the turbine duct for different values of $H_1/L$ (detail).

Figure 4.21 shows the instantaneous hydropneumatic available power for each value of $H_1/L$, calculated using equation (3.14). Then, as a means to obtain mean available power values, the RMS (equation (3.16)) was calculated for each geometry corresponding to values of $H_1/L$, as shown in figure 4.22 and table 4.9.

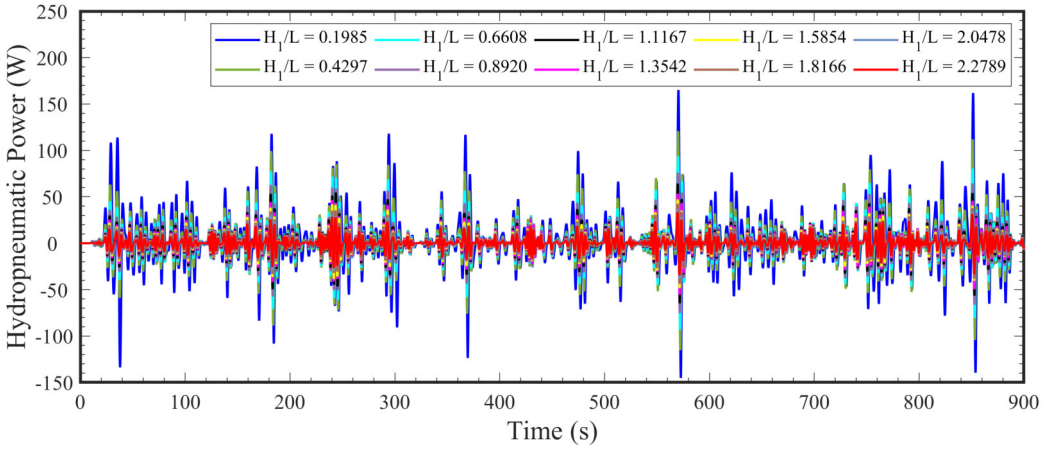


**Figure 4.21:** Instantaneous hydropneumatic power of the OWC device for different values of $H_1/L$.

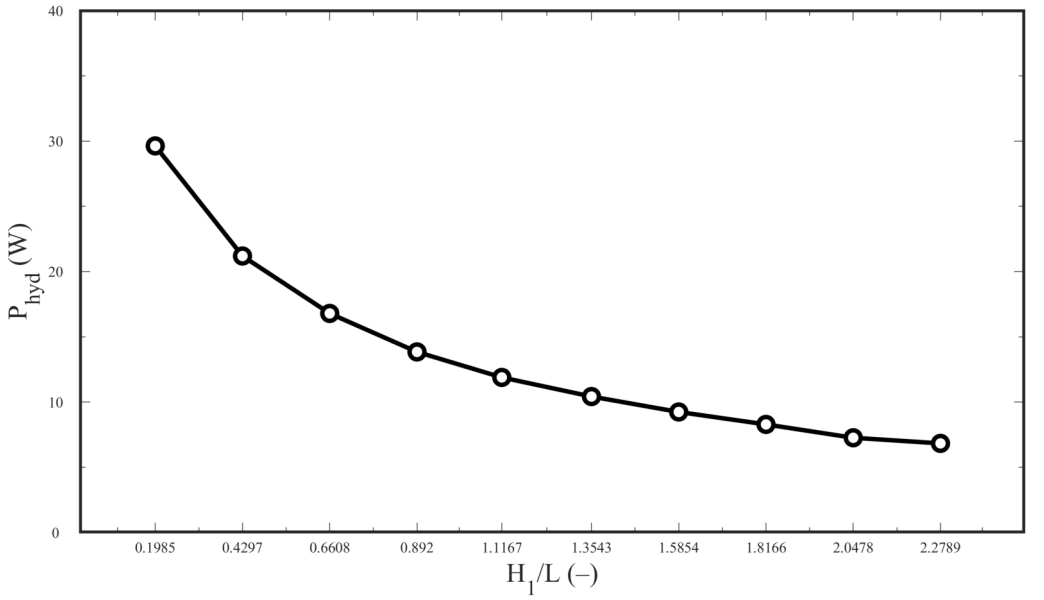


**Figure 4.22:** RMS averaged hydropneumatic power of the OWC device for different values of $H_1/L$.

From figure 4.22 and table 4.9, one can observe that the best geometry performance, which happened with geometry of $H_1/L$ value of 0.1985, presented a hydropneumatic available power $P_{hyd}$ of 29.63 W. That is 4.34 times higher than the power obtained with the worst performance geometry, which was 6.83 W, obtained with the geometry of degree of freedom $H_1/L$ value of 2.2789; and 2.49 times higher than the power obtained by the device with the same dimensions as those from the one in Pico island (see section 3.4.2), which was 11.89 W.

**Table 4.9:** Available hydropneumatic power according to each OWC device geometry simulated.

| Case | $H_1/L$ | L (m) | $H_1$ (m) | l (m) | $H_2$ (m) | $H_3$ (m) | $P_{hyd}$ (W) |
|---|---|---|---|---|---|---|---|
| **1** | 0.1985 | 28.46 | 5.65 | 2.80 | 11.30 | 6.12 | 29.63 |
| **2** | 0.4297 | 19.34 | 8.31 | 2.80 | 11.30 | 6.12 | 21.19 |
| **3** | 0.6608 | 15.60 | 10.31 | 2.80 | 11.30 | 6.12 | 16.79 |
| **4** | 0.8920 | 13.43 | 11.98 | 2.80 | 11.30 | 6.12 | 13.84 |
| **5** | 1.1167 | 12.00 | 13.40 | 2.80 | 11.30 | 6.12 | 11.89 |
| **6** | 1.3543 | 10.90 | 14.76 | 2.80 | 11.30 | 6.12 | 10.42 |
| **7** | 1.5854 | 10.07 | 15.97 | 2.80 | 11.30 | 6.12 | 9.24 |
| **8** | 1.8166 | 9.41 | 17.09 | 2.80 | 11.30 | 6.12 | 8.28 |
| **9** | 2.0478 | 8.86 | 18.15 | 2.80 | 11.30 | 6.12 | 7.26 |
| **10** | 2.2789 | 8.40 | 19.14 | 2.80 | 11.30 | 6.12 | 6.83 |

One of the cases from the Constructal Design evaluation performed by Gomes *et al.* (2018) used wave parameters similar to the ones adopted in this study, simulating a wave channel under the action of regular waves with wave period $T$ = 6 s, water depth $h$ = 10 m, wave height $H$ = 1 m, and wavelength $L$ = 48.5 m. However, device geometries were somewhat different, with submergence depth $H_3$ values ranging from 9 m to 10.25 m, while in this study $H_3$ was kept constant at 6.12 m. In the mentioned evaluation, $P_{hyd}$ ranged from 15 W to ≈ 140 W. Perhaps, the hydropneumatic power obtained by the device in this study could be improved by analyzing different $H_3$ values.

Gomes *et al.* (2019) also performed a similar application of the Constructal Design methodology, varying $H_1/L$, employing it to perform a geometric evaluation of an OWC subjected to a Pierson-Moskowitz wave spectrum. In one of the cases simulated, the length of the device chamber was 19.36 m and its height was 9.06 m, which resulted in $H_1/L$ = 0.2615; and the length of the turbine duct was 3.74 m, with its height being 11.23 m, dimensions similar to case 2 in table 4.9. Wave parameters employed for the wave spectrum were significant period $T_S$ = 7.5 s, significant wave height $H_S$ = 1.5 m, wavelength $L$ = 65.35 m, water depth $h$ = 10 m. Authors have found, for this configuration, a hydropneumatic power $P_{hyd}$ ≈ 5 kW. Figures 4.23 and 4.24 show the computational domain solution for the air-water mixture and the velocity field, respectively.

Lastly, since the Constructal Design methodology was successfully applied to evaluate the effect over the hydropneumatic power of an OWC device when varying degrees of freedom, it is possible to state that specific objective IV was achieved.

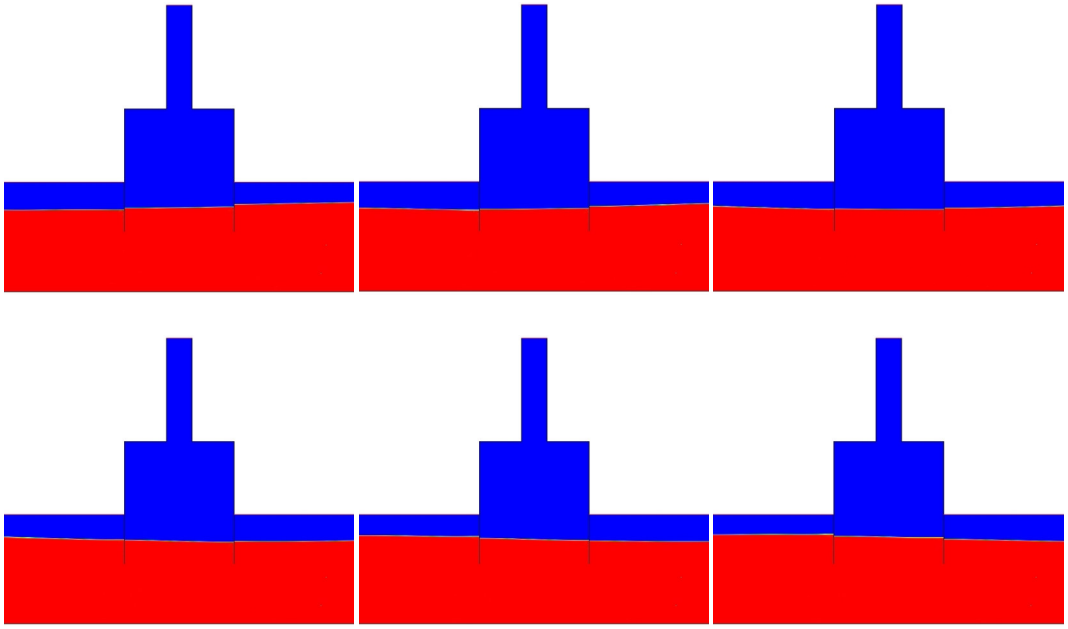

**Figure 4.23:** Instantaneous wave flow during 5 s of simulation, from 295 s to 300 s, for geometry with $H_1/L$ = 1.1167.

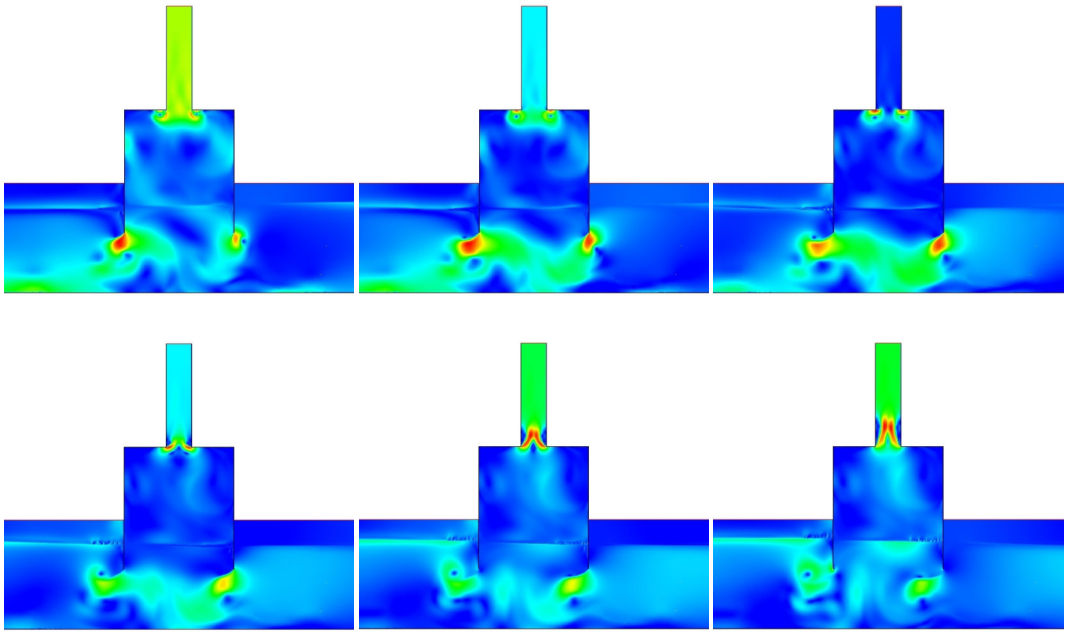

**Figure 4.24:** Instantaneous wave velocity field during 5 s of simulation, from 295 s to 300 s, for geometry with $H_1/L$ = 1.1167.

# 5 Conclusions

The OWC converter device is one of the most extensively studied in the literature. It has been analyzed through various approaches: analytical, experimental, and numerical. Due to their capacity of simulating devices and their physical phenomena, taking into account wave characteristics with accuracy, numerical procedures have been increasingly applied.

In this study, a two-dimensional approach for an OWC device was numerically subjected to irregular realistic waves in a wave channel. For this, the WaveMIMO methodology was employed, which converts sea data from a spectral model into time series of free surface elevation, which is, in turn, appropriately treated and transformed into orbital velocity components of water particles. The spectral model was Tomawac and it obtained sea state data for the year 2014, for the continental shelf ranging from the south of Rio Grande do Sul, in the border between Brazil and Uruguay, to the north of the state of Espírito Santo, as well as extending 650 km towards the ocean.

In the numerical simulations, the WaveMIMO methodology was also employed to generate regular waves with the same wave parameters as those used in a laboratory experiment. These waves were imposed as prescribed velocity boundary condition and compared with the analytical solution. Then, a laboratory-scale OWC device was inserted in the computational domain, aiming to validate the methodology employed, as shown by Maciel *et al.* (2021).

In this first procedure, several tests were performed to ensure proper wave generation, including the discretization at the region of velocity imposition, the linear damping coefficient $C_1$ at the numerical beach, mesh spatial discretization, and temporal discretization. Optimal results were obtained with 8 line segments at the region of wave generation, $C_1$ equal to 25, mesh elements throughout the channel with dimensions of $L/40$, mesh elements inside free surface refinement zone with dimensions of $H/25$, and a time step value of $T/400$. For the validation case, although there were some disparities, in general, the numerical results showed a good agreement with the laboratory experiment results. It should be highlighted that $k$-$\epsilon$ turbulence model could best represent the flow inside the wave channel.

Once the hydrodynamic model was validated, it was used to numerically simulate a real-scale OWC device subjected to realistic sea waves. For that, a statistical analysis was carried out to determine the wave parameters and interval of time representative of the year 2014, where it was found that significant wave height and mean wave period that most occurred during that year were 0.66 m and 6.30 s, respectively. For the real-scale OWC device, it were adopted dimensions similar to those of the OWC device from Pico island, Azores, Portugal.

Since the numerical waves generated for the real-scale device are different from those in the validation procedure, a second verification of the hydrodynamic model was performed. It is important remember that the generation of waves using this methodology is linked to the fractioning of the region where wave velocity data is imposed as boundary condition. Therefore, in this verification, two tests were performed, the first regarding the fractioning at the region of velocity imposition, where optimal results were obtained with 10 line segments, RMSE = 0.0762. The second one concerned the location from where, alongside each velocity profile, the wave velocity components are calculated were tested. It was found that the location from where wave velocity data is calculated which presented the smallest error was when wave velocity was calculated at the bottom of each line segment, RMSE = 0.0652. This second test, however, has not yet been performed for studies which employ the methodology of assigning transient velocity data to line segments at the entrance of a wave channel as boundary conditions.

Next, the OWC device was inserted and simulated as study case, where the free surface elevation the entrance of the wave channel was monitored and compared to the free surface elevation obtained by converting spectral data from Tomawac.

Then, a geometric evaluation of this device was performed through the Constructal Design method, which led to an analysis of the available hydropneumatic power of this device when subjected to the wave climate of Rio Grande, in the state of Rio Grande do Sul, Brazil. Numerical simulations of 15 min where then performed, with $H_1/L$ ranging from 0.1985 to 2.2789; degrees of freedom $H_2/l$ and $H_3$ were kept constant, as 4.0357 and 6.12 m, respectively. As physical constrains of the methodology, volume of the hydropneumatic chamber $V_{HC}$ and total volume $V_T$ were also kept constant, with values of 160.80 $m^2$ and 192.44 $m^2$, respectively.

The best geometry performance happened with an $H_1/L$ value of 0.1985 and presented an available hydropneumatic power $P_{byd}$ of 29.63 W. That is 4.34 times higher than the power obtained with the worst performance geometry, which was 6.83 W, obtained with the degree of freedom $H_1/L$ value of 2.2789; and 2.49 times higher than the power obtained by the device with the same dimensions as those from the one in Pico island, which was 11.89 W.

The contribution of this study was to validate a recently proposed methodology for the imposition of transient velocity data as boundary condition, in the generation of numerical waves. Since most studies use regular waves, there is a lack of analysis that use ocean waves realistic data. In this context, this methodology is innovative for it allows the use of realistic sea state data in numerical simulations regarding WECs. In this study, a geometric evaluation of an OWC device was also performed, with the Constructal Design method, while employing the WaveMIMO methodology to generate realistic irregular waves from the wave climate of Rio Grande, in the state of Rio Grande do Sul, Brazil, which is unprecedented in the literature.

## 5.1 Suggestion for future studies

This work adopted a few simplifications to avoid numerical problems which might make it difficult to complete the study. Here are listed some aspects of this study which could be improved.

- The WaveMIMO methodology, used to obtain realistic irregular wave data, may be further employed to obtain sea state data from other parts of the state of Rio Grande do Sul, or even the country;
- Other OWC device geometries may be investigated, as well as nearshore and onshore locations;
- Other degrees of freedom regarding the Constructal Design method can be analyzed;
- A three-dimensional approach to the WaveMIMO methodology could also be conducted.

# References


Airy, G. B. (1845). "Tides and Waves". In: *Encyclopædia Metropolitana* 5. Wiliam Clowes & Sons, pp. 241–396.

ANSYS Inc. (2013). *Ansys Fluent Theory Guide*. Cannonsburg, PA: ANSYS, Inc.

Arena, F., A. Romolo, G. Malara, and A. Ascanelli (2013). "On Design and Building of a U-OWC Wave Energy Converter in the Mediterranean Sea: A Case Study". In: *Proceedings of the 32nd International Conference on Ocean, Offshore and Arctic Engineering*. Nantes, France, pp. 1–8.

Awk, T. (2017). *Tomawac User Manual Version 7.2*. EDF R&D. URL: www.opentelemac.org.

Bejan, A. (1996). "Street network theory of organization in nature". In: *Journal of Advanced Transportation* 30.2, pp. 85–107. DOI: 10.1002/atr.5670300207.

Bejan, A. (1997). "Constructal-theory network of conducting paths for cooling a heat generating volume". In: *International Journal of Heat and Mass Transfer* 40.4, pp. 799–811. DOI: 10.1016/0017-9310(96)00175-5.

Bejan, A. (2016). *Advanced Engineering Thermodynamics*. 4th ed. Hoboken, New Jersey: John Wiley & Sons Inc., p. 782.

Bejan, A. and S. Lorente (2008). *Design with Constructal Theory*. Hoboken, New Jersey: John Wiley & Sons Inc., p. 552. DOI: 10.1002/9780470432709.

Ben Elghali, S. E., M. E. Benbouzid, and J. F. Charpentier (2007). "Marine tidal current electric power generation technology: State of the art and current status". In: *IEEE International Electric Machines and Drives Conference*. Antalya, Turkey, pp. 1407–1412. DOI: 10.1109/IEMDC.2007.383635.

Bhattacharyya, R. and M. E. McCormick (2003). "Wave Power Activities in the Asia-Pacific Region". In: *Wave Energy Conversion*. Ed. by R. Bhattacharyya and M. E. McCormick. Vol. 6. Elsevier Ocean Engineering Series. Elsevier, pp. 79–93. DOI: 10.1016/S1571-9952(03)80059-4.

Bueno, J. F., A. R. S. Silva, T. A. Hirt, G. F. C. Bogo, F. S. F. Zinani, and L. A. O. Rocha (2019). "Constructal Design of Fins in Cooled Cavities By Non-Newtonian Fluids". In: *Revista de Engenharia Térmica* 18.1, p. 85. DOI: 10.5380/reterm.v18i1.67055.

Cardoso, S. D., W. C. Marques, E. P. Kirinus, and C. E. Stringari (2014). "Levantamento batimétrico usando cartas náuticas". In: *13a Mostra da Produção Universitária*. Rio Grande: Universidade Federal do Rio Grande.

Carneiro, M. L. (2007). "Desenvolvimento de dispositivo de geração e absorção ativa de ondas para tanque de ensaios de estruturas oceânicas". Dissertação de mestrado. Escola Politécnica da Universidade de São Paulo, p. 98.

Çelik, A. and A. Altunkaynak (2020). "Determination of hydrodynamic parameters of a fixed OWC by performing experimental and numerical free decay tests". In: *Ocean Engineering* 204. DOI: 10.1016/j.oceaneng.2019.106827.

Cong, P., B. Teng, W. Bai, D. Ning, and Y. Liu (2021). "Wave power absorption by an oscillating water column (OWC) device of annular cross-section in a combined wind-wave energy system". In: *Applied Ocean Research* 107. DOI: 10.1016/j.apor.2020.102499.

Count, B. M. and D. V. Evans (1984). "The influence of projecting sidewalls on the hydrodynamic performance of wave-energy devices". In: *Journal of Fluid Mechanics* 145.7, pp. 361–376. DOI: 10.1017/S0022112084002962.

Dai, S., S. Day, Z. Yuan, and H. Wang (2019). "Investigation on the hydrodynamic scaling effect of an OWC type wave energy device using experiment and CFD simulation". In: *Renewable Energy*, pp. 184–194. DOI: 10.1016/j.renene.2019.04.066.

Dean, R. G. and R. A. Dalrymple (1991). *Water Wave Mechanics for Engineers and Scientists*. Vol. 2. World Scientific Publishing Company, p. 368.

Dizadji, N. and S. E. Sajadian (2011). "Modeling and optimization of the chamber of OWC system". In: *Energy* 36.5, pp. 2360–2366. DOI: 10.1016/j.energy.2011.01.010.

Dos Santos, E. D., L. A. Isoldi, M. das N. Gomes, and L. A. O. Rocha (2017). "The Constructal Design Applied to Renewable Energy Systems". In: *Sustainable Energy Technologies*. CRC Press - Taylor & Francis Group, pp. 45–62. DOI: 10.1201/9781315269979-4.

Doyle, S. and G. A. Aggidis (2019). "Development of multi-oscillating water columns as wave energy converters". In: *Renewable and Sustainable Energy Reviews* 107.January, pp. 75–86. DOI: 10.1016/j.rser.2019.02.021.

Dutra, R. F., F. S. F. Zinani, L. A. O. Rocha, and C. Biserni (2020). "Constructal design of an arterial bypass graft". In: *Heat Transfer*, pp. 1–21. DOI: 10.1002/htj.21693.

El Tawil, T., J. F. Charpentier, and M. Benbouzid (2017). "Tidal energy site characterization for marine turbine optimal installation: Case of the Ouessant Island in France". In: *International Journal of Marine Energy* 18, pp. 57–64. DOI: 10.1016/j.ijome.2017.03.004.

Empresa de Pesquisa Energética (2018). *Balanço Energético Nacional 2018: Ano base 2017*. Tech. rep. Rio de Janeiro: Ministério de Minas e Energia, 292, (*in Portuguese*). URL: http://www.epe.gov.br/sites-pt/publicacoes-dados-abertos/publicacoes/PublicacoesArquivos/publicacao-303/topico-419/BEN2018%7B%5C_%7D%7B%5C_%7DInt.pdf.

Espindola, R. L. and A. M. Araújo (2017). "Wave energy resource of Brazil: An analysis from 35 years of ERA-Interim reanalysis data". In: *PLoS ONE* 12.8, pp. 1–28. DOI: 10.1371/journal.pone.0183501.

Estrada, E. S., E. X. Barreto, L. A. Isoldi, E. D. dos Santos, S. Lorente, and L. A. Rocha (2020). "Constructal design of tree shaped cavities inserted into a cylindrical body

with heat generation". In: *International Journal of Thermal Sciences* 152. DOI: 10.1016/j.ijthermalsci.2020.106342.

Ezhilsabareesh, K., R. Suchithra, K. Thandayutham, and A. Samad (2021). "Surrogate based optimization of a Bi-Directional impulse turbine for OWC-WEC: Effect of guide vane lean and stagger angle for pseudo-sinusoidal wave conditions". In: *Ocean Engineering* 226. DOI: 10.1016/j.oceaneng.2021.108843.

Falcão, A. F. O. (2000). "The shoreline OWC wave power plant at the Azores". In: *Proceedings of the 4th European Wave Energy Conference*. Aalborg, Denmark, pp. 42–48.

Falcão, A. F. (2012). "Historical aspects of wave energy conversion". In: *Comprehensive Renewable Energy*. Ed. by A. Sayigh. Vol. 8. Oxford: Elsevier Ltd., pp. 7–9. DOI: 10.1016/B978-0-08-087872-0.00802-7. URL: http://dx.doi.org/10.1016/B978-0-08-087872-0.00802-7.

Falcão, A. F. d. O. (2008). *The Development of Wave Energy Utilisation. IEA-OES Annual Report 2008*. Tech. rep. International Energy Agency Implementing Agreement on Ocean Energy Systems (IEA-OES), pp. 30–37.

Falcão, A. F. d. O. (2014). *Modelling of Wave Energy Conversion*. Instituto Superior Técnico, Universidade Técnica de Lisboa, pp. 1–38. URL: https://fenix.tecnico.ulisboa.pt/downloadFile/3779580606646/Chapter%7B%5C%%7D25201%7B%5C%%7D25282014%7B%5C%%7D2529.pdf.

Falcão, A. F. O. and J. C. C. Henriques (2016). "Oscillating-water-column wave energy converters and air turbines: A review". In: *Renewable Energy* 85.2016, pp. 1391–1424. DOI: 10.1016/j.renene.2015.07.086.

Falcão, A. F. O., A. J. N. A. Sarmento, L. M. C. Gato, and A. Brito-Melo (2020). "The Pico OWC wave power plant: Its life from conception to closure 1986–2018". In: *Applied Ocean Research* (102104), p. 10. DOI: 10.1016/j.apor.2020.102104.

Falnes, J. (2007). "A review of wave-energy extraction". In: *Marine Structures* 20.4, pp. 185–201. DOI: 10.1016/j.marstruc.2007.09.001.

Feijó, B. C., G. Lorenzini, L. A. Isoldi, L. A. Rocha, J. N. Goulart, and E. D. dos Santos (2018). "Constructal design of forced convective flows in channels with two alternated rectangular heated bodies". In: *International Journal of Heat and Mass Transfer* 125, pp. 710–721. DOI: 10.1016/j.ijheatmasstransfer.2018.04.086.

Feng, H., Z. Xie, L. Chen, Z. Wu, and S. Xia (2019). "Constructal design for supercharged boiler superheater". In: *Energy* 191, p. 116484. DOI: 10.1016/j.energy.2019.116484.

Fenton, J. D. (1985). "A Fifth-Order Stokes Theory for Steady Waves". In: *Journal of Waterway, Port, Coastal, and Ocean Engineering* 111.2, pp. 216–234. DOI: 10.1061/(ASCE)0733-950X(1985)111:2(216).

Ferguson, T. M., A. Fleming, I. Penesis, and G. Macfarlane (2015). "Improving OWC performance prediction using polychromatic waves". In: *Energy* 93, pp. 1943–1952. DOI: 10.1016/j.energy.2015.10.086.

Fox, B. N., R. P. Gomes, and L. M. Gato (2021). "Analysis of oscillating-water-column wave energy converter configurations for integration into caisson breakwaters". In: *Applied Energy* 295. DOI: 10.1016/j.apenergy.2021.117023.

Gaspar, L. A., P. R. Teixeira, and E. Didier (2020). "Numerical analysis of the performance of two onshore oscillating water column wave energy converters at different chamber wall slopes". In: *Ocean Engineering* 201, pp. 1–14. DOI: 10.1016/j.oceaneng.2020.107119.

Geuzaine, C. and J.-F. Remacle (2009). "Gmsh: A 3-D finite element mesh generator with built-in pre- and post-processing facilities". In: *International Journal for Numerical Methods in Engineering* 79 (11). DOI: 10.1002/nme.2579.

Gomes, M. N., G. Lorenzini, L. A. Rocha, E. D. dos Santos, and L. A. Isoldi (2018). "Constructal Design Applied to the Geometric Evaluation of an Oscillating Water Column Wave Energy Converter Considering Different Real Scale Wave Periods". In: *Journal of Engineering Thermophysics* 27.2, pp. 173–190. DOI: 10.1134/S1810232818020042.

Gomes, M. d. N., M. J. De Deus, E. D. Dos Santos, L. A. Isoldi, and L. A. O. Rocha (2019). "Analysis of the geometric constraints employed in constructal design for oscillating water column devices submitted to the wave spectrum through a numerical approach". In: *Defect and Diffusion Forum* 390, pp. 193–210. DOI: 10.4028/www.scientific.net/DDF.390.193.

Gomes, M. d. N., M. J. de Deus, E. d. S. Domingues, L. A. Isoldi, and L. A. O. Rocha (2017). "The choice of geometric constraints value applied in the constructal design for Oscillating Water Column device". In: *Proceedings of the XXXVIII Iberian Latin American Congress on Computational Methods in Engineering*. Florianópolis, Brasil, pp. 1–17. DOI: 10.20906/cps/cilamce2017-0547.

Gomes, M. d. N., E. D. Dos Santos, L. A. Isoldi, and L. A. O. Rocha (2013a). "Two-Dimensional Geometric Optimization of an Oscillating Water Column Converter of Real Scale". In: *22nd International Congress of Mechanical Engineering*. Ribeirão Preto, Brasil, pp. 3468–3479.

Gomes, M. d. N., L. A. O. Rocha, K. R. Waess, L. A. Isoldi, and E. D. Dos Santos (2013b). "Modelagem Computacional e Otimização Geométrica 2D com Constructal Design de um Dispositivo do Tipo Coluna de Água Oscilante em Escala Real – Comparação Onshore E Offshore". In: *Proceedings of the XXXIV Iberian Latin-American Congress on Computational Methods in Engineering*. Pirenópolis, Brasil, pp. 1–20.

Gomes, M. d. N., H. Salvador, F. Magno, A. A. Rodrigues, E. D. Santos, L. A. Isoldi, and L. A. O. Rocha (2021). "Constructal Design Applied to Geometric Shapes Analysis of Wave Energy Converters". In: *Defect and Diffusion Forum* 407, pp. 147–160. DOI: 10.4028/www.scientific.net/DDF.407.147.

Gopala, V. R. and B. G. van Wachem (2008). "Volume of fluid methods for immiscible-fluid and free-surface flows". In: *Chemical Engineering Journal* 141.1-3, pp. 204–221. DOI: 10.1016/j.cej.2007.12.035.

Graw, K.-U. (1996). "Wave energy breakwaters - a device comparison". In: *Proceedings of the Conference in Ocean Engineering*. Madras, India.

Halliday, D., R. Resnick, and J. Walker (2018). *Fundamentals of Physics*. 11th. John Wiley & Sons, Ltd, p. 1456.

Heath, T., T. J. T. Whittaker, and C. B. Boake (2000). "The Design, Construction and Operation of the LIMPET Wave Energy Converter (Islay, Scotland)". In: *Proceedings of the 4th European Wave Energy Conference*. Aalborg, Denmark, pp. 49–55.

Hervouet, J.-M. (2007). *Hydrodynamics of Free Surface Flows: Modelling with the finite element method*. John Wiley & Sons, Ltd. DOI: 10.1002/9780470319628.

Hil Baky, M. A., M. M. Rahman, and A. K. Islam (2017). "Development of renewable energy sector in Bangladesh: Current status and future potentials". In: *Renewable and Sustainable Energy Reviews* 73.January, pp. 1184–1197. DOI: 10.1016/j.rser.2017.02.047.

Hirt, C. W. and B. D. Nichols (1981). "Volume of fluid (VOF) method for the dynamics of free boundaries". In: *Journal of Computational Physics* 39.1, pp. 201–225. DOI: 10.1016/0021-9991(81)90145-5.

Holthuijsen, L. H. (2010). *Waves in Oceanic and Coastal Waters*. Cambridge University Press, p. 404.

International Energy Agency (2017). *World Energy Balances 2017*. Tech. rep. Paris, France: International Energy Agency.

Joule III, N. N. E. P. (1998). *European Wave Energy Pilot Plant on the Island of Pico, Azores, Portugal. Phase Two: Equipment*. URL: https://cordis.europa.eu/docs/projects/files/JOR/JOR3950012/47698021-6_en.pdf.

Kamps, T., M. Biedermann, C. Seidel, and G. Reinhart (2018). "Design approach for additive manufacturing employing Constructal Theory for point-to-circle flows". In: *Additive Manufacturing* 20, pp. 111–118. DOI: 10.1016/j.addma.2017.12.005.

Kim, J. S., B. W. Nam, K. H. Kim, S. Park, S. H. Shin, and K. Hong (2020). "A numerical study on hydrodynamic performance of an inclined OWC wave energy converter with nonlinear turbine-chamber interaction based on 3D potential flow". In: *Journal of Marine Science and Engineering* 8.3. DOI: 10.3390/jmse8030176.

Kirinus, E. d. P. (2017). "Estudo Numérico de Conversão da Energia Cinética das Correntes Marinhas em Energia Elétrica na Plataforma Continental Sul-Sudeste Brasileira". PhD thesis. Universidade Federal do Rio Grande.

Kolditz, O. (2002). *Computational Methods in Environmental Fluid Mechanics*. Berlin, Germany: Springer, p. 382. DOI: 10.1007/978-3-662-04761-3.

Lerner, R. G. and G. L. Trigg (2005). *Encyclopedia of Physics*. 3rd ed. Wiley-VCH, p. 3043.

Letzow, M., G. Lorenzini, D. V. E. Barbosa, R. G. Hübner, L. A. O. Rocha, M. das Neves Gomes, L. A. Isoldi, and E. D. dos Santos (2020). "Numerical Analysis of the Influence of Geometry on a Large Scale Onshore Oscillating Water Column Device with Associated Seabed Ramp". In: *International Journal of Design & Nature and Ecodynamics* 15 (6), pp. 873–884. DOI: 10.18280/ijdne.150613.

Lima, J. P. S., M. L. Cunha, E. D. dos Santos, L. A. O. Rocha, M. d. V. Real, and L. A. Isoldi (2020). "Constructal Design for the ultimate buckling stress improvement of stiffened plates submitted to uniaxial compressive load". In: *Engineering Structures* 203. DOI: 10.1016/j.engstruct.2019.109883.

Lima, Y. T., M. N. Gomes, C. F. Cardozo, L. A. Isoldi, E. D. Santos, and L. A. Rocha (2019). "Analysis of geometric variation of three degrees of freedom through the constructal design method for a oscillating water column device with double hidropneumatic chamber". In: *Defect and Diffusion Forum* 396, pp. 22–31. DOI: 10.4028/www.scientific.net/DDF.396.22.

Lima, Y. T. B., L. A. O. Rocha, M. d. N. Gomes, L. A. Isoldi, and E. D. dos Santos (2017). "Numerical Evaluation of Hydropneumatic Power for Two Oscillating Water Column (OWC) Devices Coupled Using Constructal Design". In: *Proceedings of the XXXVIII Iberian Latin American Congress on Computational Methods in Engineering*. Florianópolis, Brasil. DOI: 10.20906/cps/cilamce2017-0231.

Lima, Y. T. B. d., M. D. N. Gomes, L. A. Isoldi, E. D. D. Santos, G. Lorenzini, and L. A. O. Rocha (2021). "Geometric analysis through the constructal design of a sea wave energy converter with several coupled hydropneumatic chambers considering the oscillating water column operating principle". In: *Applied Sciences* 11 (18). DOI: 10.3390/app11188630.

Lisboa, R. C., P. R. F. Teixeira, and E. Didier (2017). "Regular and Irregular Wave Propagation Analysis in a Flume with Numerical Beach Using a Navier-Stokes Based Model". In: *Defect and Diffusion Forum* 372. DOI: 10.4028/www.scientific.net/DDF.372.81.

Lisboa, R. C., P. R. Teixeira, F. R. Torres, and E. Didier (2018). "Numerical evaluation of the power output of an oscillating water column wave energy converter installed in the southern Brazilian coast". In: *Energy* 162, pp. 1115–1124. DOI: 10.1016/j.energy.2018.08.079.

Liu, Z., B. S. Hyun, and K. Hong (2011). "Numerical study of air chamber for oscillating water column wave energy convertor". In: *China Ocean Engineering* 25.1, pp. 169–178. DOI: 10.1007/s13344-011-0015-8.

López, I., R. Carballo, F. Taveira-Pinto, and G. Iglesias (2020). "Sensitivity of OWC performance to air compressibility". In: *Renewable Energy* 145, pp. 1334–1347. DOI: 10.1016/j.renene.2019.06.076.

Lorenzini, G., M. F. E. Lara, L. A. O. Rocha, M. D. N. Gomes, E. D. Dos Santos, and L. A. Isoldi (2015). "Constructal design applied to the study of the geometry and submergence of an Oscillating Water Column". In: *International Journal of Heat and Technology* 33.2, pp. 31–38. DOI: 10.18280/ijht.330205.

Lui, C. H., N. K. Fong, S. Lorente, A. Bejan, and W. K. Chow (2015). "Constructal design of evacuation from a three-dimensional living space". In: *Physica A: Statistical Mechanics and its Applications* 422, pp. 47–57. DOI: 10.1016/j.physa.2014.12.005.

Machado, B. N., E. V. Kisner, M. d. S. Paiva, M. d. N. Gomes, L. A. O. Rocha, W. C. Marques, E. D. dos Santos, and L. A. Isoldi (2017). "Numerical Generation of Regular Waves Using Discrete Analytical Data As Boundary Condition of Prescribed Velocity". In: *Proceedings of the XXXVIII Iberian Latin American Congress on Computational Methods in Engineering*. Florianópolis, Brasil. DOI: 10.20906/cps/cilamce2017-0816.

Machado, B. N., P. H. Oleinik, E. D. P. Kirinus, E. D. D. Santos, L. A. O. Rocha, M. D. N. Gomes, J. M. P. Conde, and L. A. Isoldi (2021). "WaveMIMO Methodology: Numerical Wave Generation of a Realistic Sea State". In: *Journal of Applied and Computational Mechanics* 7 (4), pp. 2129–2148. DOI: 10.22055/jacm.2021.37617.3051.

Maciel, R. P., C. Fragassa, B. N. Machado, L. A. Rocha, E. D. Dos Santos, M. N. Gomes, and L. A. Isoldi (2021). "Verification and validation of a methodology to numerically generate waves using transient discrete data as prescribed velocity boundary condition". In: *Journal of Marine Science and Engineering* 9 (896), pp. 1–19. DOI: 10.3390/jmse9080896.

Maliska, C. R. (2004). *Transferência de Calor e Mecânica dos Fluidos Computacional*. 2nd ed. LTC, 454p.

Malley-Ernewein, A. and S. Lorente (2019). "Constructal design of thermochemical energy storage". In: *International Journal of Heat and Mass Transfer* 130, pp. 1299–1306. DOI: 10.1016/j.ijheatmasstransfer.2018.10.097.

Marjani, A. E., F. Castro, M. Bahaji, and B. Filali (2006). "3D unsteady flow simulation in an OWC wave converter plant". In: *Renewable Energy and Power Quality Journal* 1 (4), pp. 350–355. DOI: 10.24084/repqj04.452.

Martins, J. C., M. M. Goulart, M. d. N. Gomes, J. A. Souza, L. A. Rocha, L. A. Isoldi, and E. D. dos Santos (2018). "Geometric evaluation of the main operational principle of an overtopping wave energy converter by means of Constructal Design". In: *Renewable Energy* 118, pp. 727–741. DOI: 10.1016/j.renene.2017.11.061.

Mavriplis, D. J. (1995). *Unstructured Mesh Generation and Adaptivity*. Program of the von Karman Institute for Fluid Dynamics. URL: https://apps.dtic.mil/dtic/tr/fulltext/u2/a294551.pdf.

Meier, G. E. A. and K. R. Sreenivasan (2004). "(Eds.). IUTAM Symposium on One Hundred Years of Boundary Layer Research". In: *Proceedings of the International Union of Theoretical and Applied Mechanics Symposium*. Göttingen, Germany: Springer, p. 507.

Melikoglu, M. (2018). "Current status and future of ocean energy sources: A global review". In: *Ocean Engineering* 148.November 2017, pp. 563–573. DOI: 10.1016/j.oceaneng.2017.11.045.

Mendonça, A., J. Dias, E. Didier, C. J. Fortes, M. G. Neves, M. T. Reis, J. M. Conde, P. Poseiro, and P. R. Teixeira (2018). "An integrated tool for modelling oscillating water column (OWC) wave energy converters (WEC) in vertical breakwaters". In:

*Journal of Hydro-Environment Research* 19, pp. 198–213. DOI: 10.1016/j.jher.2017.10.007. URL: https://doi.org/10.1016/j.jher.2017.10.007.

Misra, S. and J. He (2020). "Chapter 3 - Shallow neural networks and classification methods for approximating the subsurface in situ fluid-filled pore size distribution". In: *Machine Learning for Subsurface Characterization*. Ed. by S. Misra, H. Li, and J. He. Gulf Professional Publishing, pp. 65–101. DOI: https://doi.org/10.1016/B978-0-12-817736-5.00003-X.

Mosa, M., M. Labat, and S. Lorente (2019a). "Constructal design of flow channels for radiant cooling panels". In: *International Journal of Thermal Sciences* 145. DOI: 10.1016/j.ijthermalsci.2019.106052.

Mosa, M., M. Labat, and S. Lorente (2019b). "Role of flow architectures on the design of radiant cooling panels, a constructal approach". In: *Applied Thermal Engineering* 150.2018, pp. 1345–1352. DOI: 10.1016/j.applthermaleng.2018.12.107.

Neill, S. P. and M. R. Hashemi (2018). "Chapter 8 - Ocean Modelling for Resource Characterization". In: *Fundamentals of Ocean Renewable Energy*. Ed. by S. P. Neill and M. R. Hashemi. E-Business Solutions. Academic Press, pp. 193–235. DOI: https://doi.org/10.1016/B978-0-12-810448-4.00008-2.

Offshore Energy (2018). *Stranded wave device to grow into artificial reef off Australia*. URL: https://www.offshore-energy.biz/stranded-wave-device-to-grow-into-artificial-reef-australia/ (visited on 06/19/2020).

Ohanian, H. C. and J. T. Markert (2007). *Physics for Engineers and Scientists*. 3rd ed. London, UK: Norton & Company, Inc., p. 816.

Oleinik, P. H., B. N. Machado, and L. A. Isoldi (2021). "Transformation of Water Wave Spectra into Time Series of Surface Elevation". In: *Earth* 2 (4), pp. 997–1005. DOI: 10.3390/earth2040059.

Oleinik, P. H. (2020). "Metodologia Numérica para a Simulação Hidrodinâmica de Estados de Mar Utilizando Dados Espectrais e Estudo de Caso de um OWC na Costa de Rio Grande–RS". MA thesis. Rio Grande: Universidade Federal do Rio Grande, p. 112.

Oleinik, P. H., E. d. P. Kirinus, C. Fragassa, W. C. Marques, and J. Costi (2019). "Energetic Potential Assessment of Wind-Driven Waves on the South-Southeastern Brazilian Shelf". In: *Journal of Marine Science and Engineering* 7.2. DOI: 10.3390/jmse7020025.

Oleinik, P. H., W. C. Marques, and E. d. P. Kirinus (2017). "Estimate of the wave climate on the most energetic locations of the south-southeastern Brazilian shelf". In: *Defect and Diffusion Forum* 370, pp. 130–140. DOI: 10.4028/www.scientific.net/DDF.370.130.

Pedroti, V. A., C. C. de Escobar, E. D. dos Santos, and J. A. Souza (2020). "Thermal analysis of tubular arrangements submitted to external flow using constructal theory". In: *International Communications in Heat and Mass Transfer* 111. DOI: 10.1016/j.icheatmasstransfer.2019.104458.

Perić, R. and M. Abdel-Maksoud (2016). "Reliable damping of free-surface waves in numerical simulations". In: *Ship Technology Research* 63.1, pp. 1–13. DOI: 10.1080/09377255.2015.1119921.

Plamer, C. B., Y. T. B. de Lima, L. A. Isoldi, E. D. Dos Santos, L. A. O. Rocha, and M. d. N. Gomes (2017). "Modelagem Computacional e Método Constructal Design Aplicados a um Conversor do Tipo Coluna de Água Oscilante (CAO) Analisando a Influência em seu Desempenho da Variação da Razão Entre o Volume de Entrada e o Volume Total da Câmara Hidropneumática". In: *Revista Brasileira de Energias Renováveis* 6.3, pp. 507–526. DOI: 10.5380/rber.v6i3.52995.

Portillo, J. C., P. F. Reis, J. C. Henriques, L. M. Gato, and A. F. Falcão (2019). "Backward bent-duct buoy or frontward bent-duct buoy? Review, assessment and optimisation". In: *Renewable and Sustainable Energy Reviews* 112.March, pp. 353–368. DOI: 10.1016/j.rser.2019.05.026.

Razera, A. L., R. J. da Fonseca, L. A. Isoldi, E. D. dos Santos, L. A. Rocha, and C. Biserni (2018). "Constructal design of a semi-elliptical fin inserted in a lid-driven square cavity with mixed convection". In: *International Journal of Heat and Mass Transfer* 126, pp. 81–94. DOI: 10.1016/j.ijheatmasstransfer.2018.05.157.

Ressurreição, A., J. Gibbons, T. P. Dentinho, M. Kaiser, R. S. Santos, and G. Edwards-Jones (2011). "Economic valuation of species loss in the open sea". In: *Ecological Economics* 70.4, pp. 729–739. DOI: 10.1016/j.ecolecon.2010.11.009.

Ribeiro, P. and D. Queiros-Condé (2019). "On the entropy production of the elemental construct of the constructal designed plate generating heat". In: *International Journal of Thermal Sciences* 145, pp. 1–11. DOI: 10.1016/j.ijthermalsci.2019.106043.

Rodrigue, J.-P. (2020). *The Geography of Transport Systems*. 5th. Routledge. DOI: 10.4324/9780429346323.

Sabedra, S. d. O., P. H. Oleinik, M. D. N. Gomes, E. D. Dos Santos, J. A. Souza, L. A. O. Rocha, W. C. Marques, and L. A. Isoldi (2017). "Modelagem computacional de um conversor de energia das ondas em energia elétrica do tipo Coluna de Água Oscilante (CAO) considerando dados de estado do mar". In: *Scientia Plena* 13.4, pp. 1–10. DOI: 10.14808/sci.plena.2017.049915.

Santos, A. L. d., C. Fragassa, A. L. G. Santos, R. S. Vieira, L. A. O. Rocha, J. M. P. Conde, L. A. Isoldi, and E. D. dos Santos (2022). "Development of a Computational Model for Investigation of and Oscillating Water Column Device with a Savonius Turbine". In: *Journal of Marine Science and Engineering* 10 (1), p. 79. DOI: 10.3390/jmse10010079.

Schlichting, H. and K. Gersten (2000). *Boundary-Layer Theory*. 8th. Berlin, Germany: Springer, p. 802. DOI: 10.1007/978-3-642-85829-1.

Shalby, M., A. Elhanafi, P. Walker, and D. G. Dorrell (2019). "CFD modelling of a small–scale fixed multi–chamber OWC device". In: *Applied Ocean Research* 88.March, pp. 37–47. DOI: 10.1016/j.apor.2019.04.003.

Simonetti, I., L. Cappietti, H. Elsafti, and H. Oumeraci (2018). "Evaluation of air compressibility effects on the performance of fixed OWC wave energy converters

using CFD modelling". In: *Renewable Energy* 119, pp. 741–753. DOI: 10.1016/j.renene.2017.12.027.

Singh, U., N. Abdussamie, and J. Hore (2020). "Hydrodynamic performance of a floating offshore OWC wave energy converter: An experimental study". In: *Renewable and Sustainable Energy Reviews* 117. DOI: 10.1016/j.rser.2019.109501.

Srinivasan, V., A. J. Salazar, and K. Saito (2011). "Modeling the disintegration of modulated liquid jets using volume-of-fluid (VOF) methodology". In: *Applied Mathematical Modelling* 35.8, pp. 3710–3730. DOI: 10.1016/j.apm.2011.01.040.

Stokes, G. G. (1847). "On the Theory of Oscillatory Waves". In: *Transactions of the Cambridge Philosophical Society* VIII, pp. 441–455.

Sutton, M. (2017). *Court proceedings 'delay action' to remove stranded Oceanlinx wave energy generator*. URL: https://www.abc.net.au/news/2017-05-17/oceanlinx-generator-stranded-as-court-proceedings-continue/8529602.

Tavares, G. P. (2019). "Estudo Numérico Comparativo da Potência Disponível entre Ondas Regulares e Irregulares — Estudo de Caso de um Dispositivo de Conversão de Energia CAO na Costa de Rio Grande – RS". Trabalho de Conclusão de Curso. Rio Grande: Universidade Federal do Rio Grande, p. 83.

Tavares, G. P., R. P. Maciel, E. D. dos Santos, M. d. N. Gomes, L. A. O. Rocha, B. N. Machado, P. H. Oleinik, and L. A. Isoldi (2020). "A Comparative Numerical Analysis of the Available Power Between Regular and Irregular Waves: Case Study of an Oscillating Water Column Converter in Rio Grande Coast, Brazil". In: *Procceedings of the 18th Brazilian Congress of Thermal Sciences and Engineering*, p. 11. DOI: 10.26678/abcm.encit2020.cit20-0304.

Teixeira, F. B., G. Lorenzini, M. R. Errera, L. A. Rocha, L. A. Isoldi, and E. D. dos Santos (2018). "Constructal Design of triangular arrangements of square bluff bodies under forced convective turbulent flows". In: *International Journal of Heat and Mass Transfer* 126, pp. 521–535. DOI: 10.1016/j.ijheatmasstransfer.2018.04.134.

Thorpe, T. W. (1999). *A Brief Review of Wave Energy: A report produced for The UK Department of Trade and Industry*. Tech. rep. Oxfordshire, UK: ETSU-R120. AEA Techonology.

Toffoli, A. and E. M. Bitner-Gregersen (2017). "Types of Ocean Surface Waves, Wave Classification". In: *Encyclopedia of Maritime and Offshore Engineering*. Ed. by J. Carlton, P. Jukes, and Y. S. Choo, pp. 1–8. DOI: 10.1002/9781118476406.emoe077.

Torre-Enciso, Y., I. Ortubia, L. I. López de Aguileta, and J. Marqués (2009). "Mutriku Wave Power Plant: from the thinking out to the reality". In: *Proceedings of the 8th European Wave and Tidal Energy Conference (EWTEC 2009)*. Uppsala, Sweden, pp. 319–328. URL: http://tethys.pnnl.gov/sites/default/files/publications/Torre-Enciso%7B%5C_%7Det%7B%5C_%7Dal%7B%5C_%7D2009.pdf.

Tucker, P. G. (2016). *Advanced Computational Fluid and Aerodynamics*. Cambridge University Press. DOI: 10.1017/CBO9781139872010.

U.S. Army Corps of Engineers (2002). *Coastal Engineering Manual: Engineering Manual 1110-2-1100*. Washington, DC: U.S. Army Corps of Engineers. URL: www.publications.usace.army.mil/USACE-Publications/Engineer-Manuals/.

Uihlein, A. and D. Magagna (2016). "Wave and tidal current energy - A review of the current state of research beyond technology". In: *Renewable and Sustainable Energy Reviews* 58, pp. 1070–1081. DOI: 10.1016/j.rser.2015.12.284.

Versteeg, H. K. and W. Malalasekera (2007). *An Introduction to Computational Fluid Dynamics*. Pearson: Prentice Hall, p. 517.

Vianna, J. C. B., E. d. S. D. Estrada, L. A. Isoldi, E. D. dos Santos, and J. A. Souza (2018). "A new Constructal Theory based algorithm applied to thermal problems". In: *International Journal of Thermal Sciences* 126.2017, pp. 118–124. DOI: 10.1016/j.ijthermalsci.2017.12.023.

Vieira, R. S., A. P. Petry, L. A. Rocha, L. A. Isoldi, and E. D. dos Santos (2017). "Numerical evaluation of a solar chimney geometry for different ground temperatures by means of constructal design". In: *Renewable Energy* 109, pp. 222–234. DOI: 10.1016/j.renene.2017.03.007.

Vural, G. (2020). "Renewable and non-renewable energy-growth nexus: A panel data application for the selected Sub-Saharan African countries". In: *Resources Policy* 65.2020, p. 7. DOI: 10.1016/j.resourpol.2019.101568.

Wang, C., Z. Deng, P. Wang, and Y. Yao (2019). "Wave power extraction from a dual oscillating-water-column system composed of heave-only and onshore units". In: *Energies* 12.9. DOI: 10.3390/en12091742.

Whittaker, T. J., W. Beattie, S. Raghunathan, A. Thompson, T. Stewart, and R. Curran (1997). "The Islay wave power project: An engineering perspective". In: *Proceedings of the Institution of Civil Engineers: Water and Maritime Engineering* 124.3, pp. 189–201. DOI: 10.1680/iwtme.1997.29783.

World Water Assessment Programme (2009). *The United Nations World Water Development Report 3: Water in a Changing World*. Tech. rep. Paris: UNESCO, pp. 17–65. DOI: 10.1142/9781848160682_0002.

Wu, Z., H. Feng, L. Chen, Z. Xie, and C. Cai (2019a). "Pumping power minimization of an evaporator in ocean thermal energy conversion system based on constructal theory". In: *Energy* 181, pp. 974–984. DOI: 10.1016/j.energy.2019.05.216.

Wu, Z., H. Feng, L. Chen, Z. Xie, C. Cai, and S. Xia (2019b). "Optimal design of dual-pressure turbine in OTEC system based on constructal theory". In: *Energy Conversion and Management* 201. DOI: 10.1016/j.enconman.2019.112179.

Xie, Z., H. Feng, L. Chen, and Z. Wu (2019). "Constructal design for supercharged boiler evaporator". In: *International Journal of Heat and Mass Transfer* 138, pp. 571–579. DOI: 10.1016/j.ijheatmasstransfer.2019.04.078.

Xu, C. and Z. Huang (2019). "Three-dimensional CFD simulation of a circular OWC with a nonlinear power-takeoff: Model validation and a discussion on resonant slosh-

ing inside the pneumatic chamber". In: *Ocean Engineering* 176, pp. 184–198. DOI: 10.1016/j.oceaneng.2019.02.010.

Zabihi, M., S. Mazaheri, and M. M. Namin (2019). "Numerical Validation of Experimental Tests Conducted on a Fixed Offshore Oscillating Water Column". In: *International Journal of Coastal and Offshore Engineering* 2, pp. 1–8.

Zeng, S., Y. Liu, C. Liu, and X. Nan (2017). "A review of renewable energy investment in the BRICS countries: History, models, problems and solutions". In: *Renewable and Sustainable Energy Reviews* 74, pp. 860–872. DOI: 10.1016/j.rser.2017.03.016.

Zhang, D., W. Li, and Y. Lin (2009). "Wave energy in China: Current status and perspectives". In: *Renewable Energy* 34.10, pp. 2089–2092. DOI: 10.1016/j.renene.2009.03.014.

Zhou, Z., S. Ke, R. Wang, R. Mayon, and D. Ning (2022). "Hydrodynamic Investigation on a Land-Fixed OWC Wave Energy Device under Irregular Waves". In: *Applied Sciences* 12 (6). DOI: 10.3390/app12062855.